The PHILOSOPHICAL MAGAZINE

FIRST PUBLISHED IN 1798

. 46 SEVENTH SERIES No. 376 May 1955

A Journal of Theoretical Experimental and Applied Physics

PRICE 15s. 0d.
Annual Subscription £8 0s. 0d. payable in advance

AND PUBLISHED BY TAYLOR & FRANCIS LTD., RED LION COURT, FLEET ST., LONDON, E.C.4.

LV. *The Optical and Electrical Properties of Single Crystals of Sodium Niobate*

By L. E. Cross* and B. J. Nicholson†
Department of Physics, University of Leeds‡

[Received January 10, 1955]

Abstract

The optical strains and dielectric constants of small single crystals of sodium niobate have been measured over the temperature range −190°c to +650°c. At room temperature the properties are consistent with an antiferroelectric structure, and for high fields applied perpendicular to the orthorhombic *c* axis, double hysteresis curves have been observed. At low temperature there is evidence of ferroelectric properties for fields applied parallel to the *c* axis. In the most perfect crystals the Curie temperature is below −209°c, but the ferroelectric phase may be induced by a high electric field. There is a long thermal hysteresis on this change and once transformed the crystals remain ferroelectric to −55°c. Above 350°c the symmetry is only pseudo-tetragonal, truly orthorhombic, and two minor structure changes, at 470°c and 518°c are observed, before the structure becomes cubic at 638°c.

§1. Introduction

Sodium niobate $NaNbO_3$ is of particular interest in the study of ferroelectrics, as it appears to exhibit some of the properties of both ferroelectric and antiferroelectric materials.

X-ray structure determinations (Wood 1951, Vousden 1951 a, b) show that the crystal has a multiple unit cell at room temperature and that within the unit, ionic displacements from the ideal positions occur in anti-parallel arrays (see especially Vousden 1951, fig. 4), giving a non-polar structure characteristic of an antiferroelectric material (Kittel 1951).

Electrical measurements on single crystals (Matthias 1949, Matthias and Remeika 1951) however appear to indicate ferroelectric properties at room temperature, with electric hysteresis, measurable piezoelectric response, and a Curie temperature at 480°c. Vousden (1951) also reports twin boundary motion under high electric stress, though Wood (*loc. cit.*) using smaller fields, finds no detectable changes.

To resolve this anomaly we have made a critical re-examination of the optical and electrical properties of small single crystals. A preliminary report has been published (Cross and Nicholson 1954) and the present article is a more detailed account of this work.

* Now with the British Electrical and Allied Industries Research Association, Perivale.

† Now with Marconi's Research and Development Laboratories, Great Baddow, Essex.

‡ Communicated by Professor E. C. Stoner, F.R.S.

§ 2. Preparation and Selection of Crystals

The specimens used in these measurements were grown by the fusion of sodium bicarbonate and niobium pentoxide in excess sodium fluoride. The proportions were initially those given by Wood (*loc. cit.*), sodium bicarbonate being used in place of the carbonate, as it is more readily available in the anhydrous form. The melt was packed into a platinum crucible, heated to 1300°C in an electric muffle, maintained at this temperature for four hours, then cooled at 40°C/hour to 200°C. Under these conditions the addition of 5% excess $NaHCO_3$ appeared to improve the quality of the resulting crystals, and most of the specimens subsequently examined were from these melts. The niobate crystals were extracted by dissolving away the excess sodium fluoride in hot water.

All the crystals extracted contained a high proportion of irregular heavily twinned specimens, which were useless for even qualitative examination and a method of optical sorting was devised. The crystals extracted from the melt were broadcast over cover slips ruled in 5 mm squares and systematically examined under a low power polarizing microscope. The qualities sought were regular shape, flat faces, simple internal structure, good extinction in polarized light and for the electrical work, a ratio of useful linear dimensions to thickness greater than 10 : 1.

It is estimated that in this manner some 250 000 crystals were superficially inspected, approximately 150 selected for further examination and detailed measurements taken on 62 of these samples. The average size of crystal selected was $0{\cdot}7 \times 0{\cdot}7 \times 0{\cdot}05$ mm. The best sample had a region 1 mm $\times$ 1·3 mm free from major twin boundaries and a thickness of 0·033 mm.

§ 3. Optical Properties

The optical properties of these crystals at room temperature are consistent with orthorhombic symmetry and the samples differ in only two respects from the properties previously reported by Wood. (i) The '(100)'* type twin boundaries, which appear as fine lines running parallel to the edge on suitably oriented specimens, are more widely spaced. In several specimens it was possible to find regions up to 0·3 mm square completely free from twinning and the contrast with the very close twinning which is evident in $BaTiO_3$ below 0°C is very striking. (ii) The birefringence at room temperature, viewing down the c axis is $0{\cdot}073 \pm 0{\cdot}002$ for NaD light, considerably smaller than the value 0·13 given by Wood.

Crystals of orthorhombic symmetry are optically biaxial, the indicatrix being a triaxial ellipsoid whose semi-axes $\alpha\beta\gamma$, the principal refractive indices, coincide with the crystallographic axes. In $NaNbO_3$ at room temperature, the orthorhombic axes are inclined at 45° to the original cubic axes in the (001) plane. Thus viewing a crystal with well developed cube faces, along [001], there is symmetric extinction in polarized light

* Following Wood (*loc. cit.*) quotation marks are used to distinguish indices which refer to the original cubic axes.

and the anisotropy $\Delta\mu_1$ is the difference between two principal refractive indices ($\beta-\alpha$). The cube faces parallel to [001] are (110) type faces of the orthorhombic crystal, thus viewing perpendicular to these faces the crystals show parallel extinction and the anisotropy $\Delta\mu_2$ is the difference between the principal index γ and the 45° bisector of the axes of the ellipse in the $\alpha\beta$ plane of the indicatrix.

The variation of $\Delta\mu_1$ and $\Delta\mu_2$ with temperature is shown in fig. 1. The curves are mean values for measurements on 15 crystals, the region below room temperature being dotted as in each case only one sample has been measured over this range.

Fig. 1

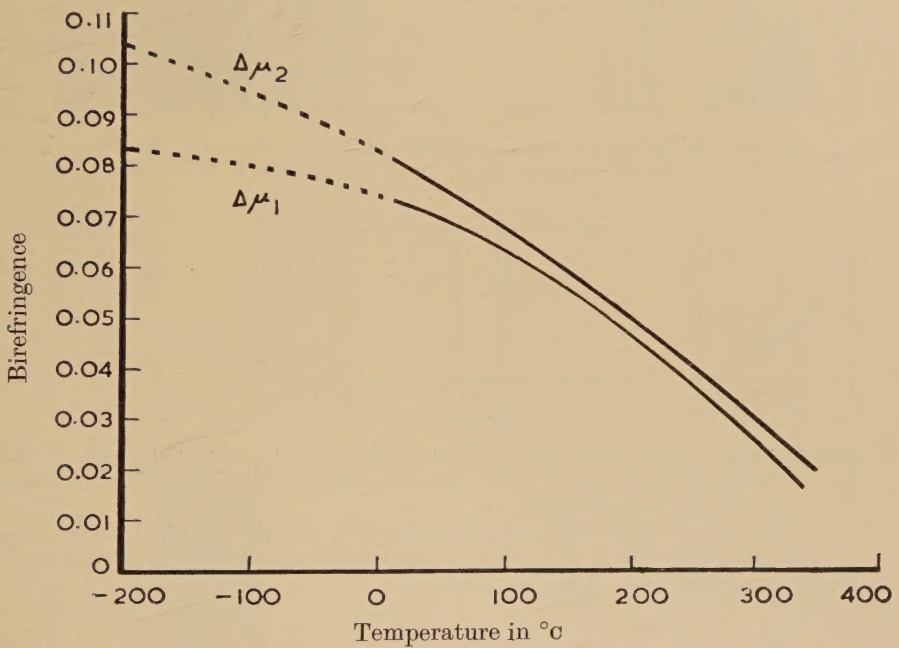

The variation of the optical anisotropies $\Delta\mu_1$, $\Delta\mu_2$ with temperature in orthorhombic $NaNbO_3$ measured in NaD light.

At 360°c±15°c on heating, there is a discontinuous change in the optical properties, most noticeable in that all regions of symmetric extinction are lost. In the new phase above 360°c, all the axial directions show optical anisotropy with parallel extinction, and twinning is observed about (110), (101), and (011) planes. The true symmetry must be orthorhombic, though the anisotropy $\Delta\mu_{\gamma\beta}$ is very small, and the distortion from tetragonal probably too small to detect by x-ray methods.

A typical example of the twin structure in this phase is shown in fig. 2, the probable orientation of the orthorhombic axes in each twin component deduced from the optical data is indicated.

The variation of the ' birefringences ' from 350°c to 638°c is shown in fig. 3. Two minor structure changes are evident before the crystals become cubic at 638°c. At 470°c on heating, there is a discontinuous

change in all the optical strains, the relative magnitudes are not however greatly changed, and it is easy to miss the effect unless actually observing the specimen at the transition temperature. At 518°c the optical change is more pronounced and on very thin specimens where $\Delta\mu_{\gamma\beta}$ produces little optical path difference, appears equivalent to a rotation of the

Fig. 2

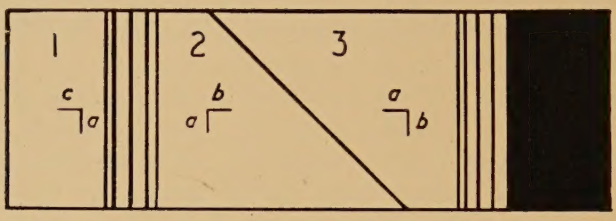

Crystal thickness 0·01 cm, polarized light, Nicols at 45° to the extinction position, temperature 360°c

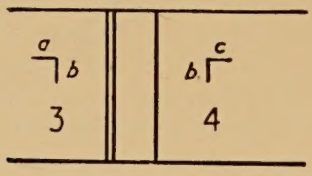

Zero order

A diagrammatic representation of the optical effect in polarized light, of the twinning observed above 350°c in a crystal of $NaNbO_3$ (Nicols crossed at 45° to the crystal edge).

The optical path difference in regions 2, 3 which would be zero in a tetragonal crystal is $\simeq \frac{1}{4}$ order in NaD, and the birefringence of 3 is of different sign to 1, 2 and 4.

Fig. 3

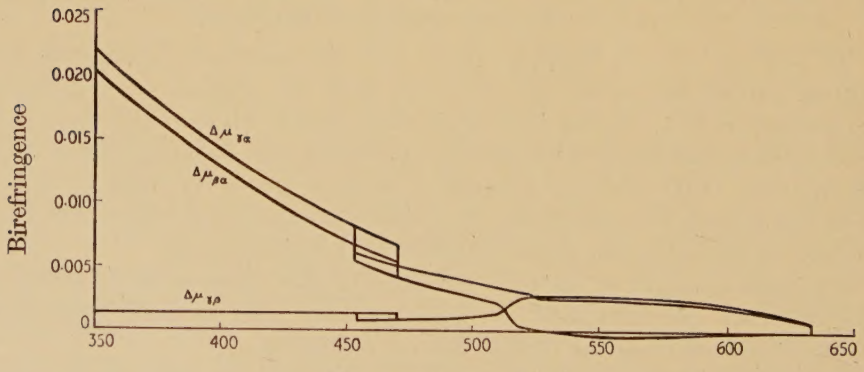

The variation of 'birefringence' with temperature in pseudotetragonal $NaNbO_3$ measured in NaD light.

pseudo-tetrad axis. The optical effects in polarized light of two typical crystals are summarized in fig. 4. To simplify the presentation the same axes are retained above the transition, though in this region the optical data suggests that $b > c > a$ and $b \simeq c$.

Fig. 4

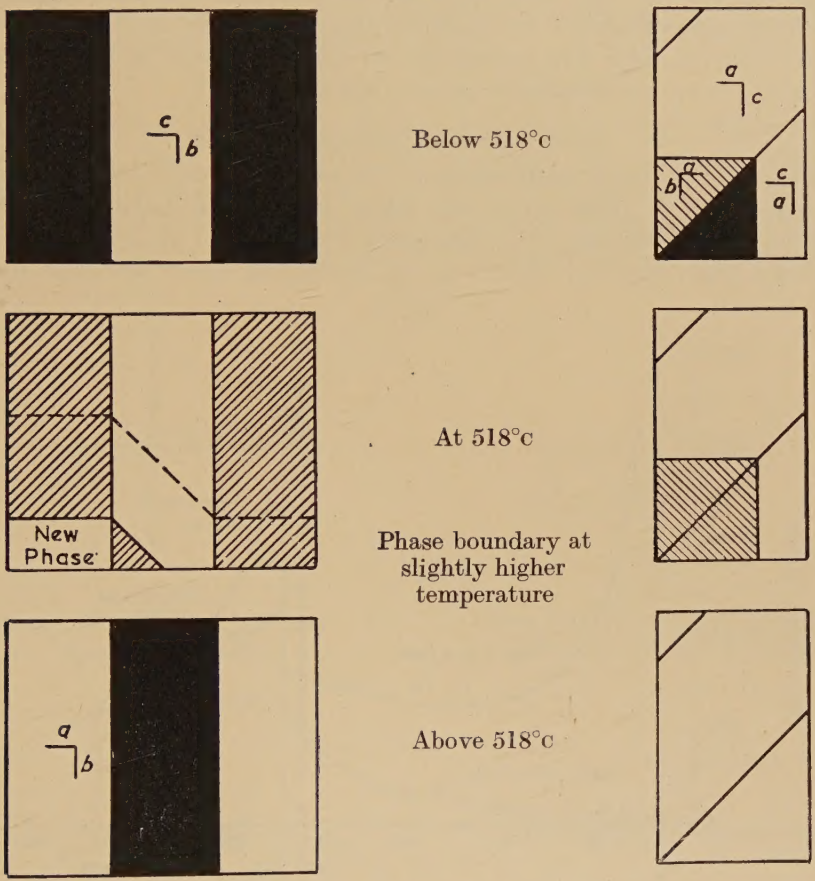

A diagrammatic representation of the optical effects in polarized monochromatic light of the structure change at 518°c in a thin crystal of $NaNbO_3$. The smallest birefringence $\Delta\mu_{\gamma\beta}$ below 518°c and $\Delta\mu_{\beta\alpha}$ above 518°c produce no appreciable path difference, so that the transition is equivalent to a rotation of the pseudotetrad axis, with a change in sign of the crystal.

No measurable thermal hysteresis was detected at 638°c or 518°c, though this may be due to the finite range (about 1·5°c), over which the two phases co-exist, which makes it difficult to assign exact transition temperatures. The change at 470°c occurs on cooling at 450°c.

The major twin boundaries are usually retained at 470°c and 518°c, heating above 638°c however usually produced a new twin structure on re-cooling.

§ 4. Electrical Measurements

For electrical work below 500°C, gold electrodes were evaporated onto the crystal faces. Above 500°C gold films were found to deteriorate rapidly and semi-transparent palladium electrodes were used. It was not possible to select specimens which were completely free from internal twinning, and for this work electrodes of restricted size were applied to optically selected areas. To minimize edge corrections, circular electrodes were used on very thin specimens, so that the ratio of the electrode diameter to crystal thickness was not less than 7 : 1.

Measurements at Low Fieldstrength

The variation with temperature of the weak field dielectric constant is shown in fig. 5. The curve was taken on a single specimen, without altering the electrodes, the orientation changing on successive heating through 638°C and was chosen as the numerical values are close to the

Fig. 5

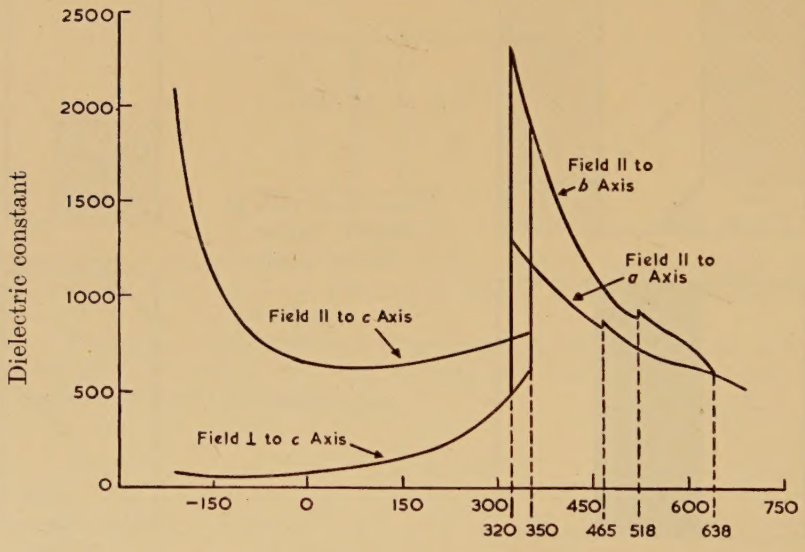

The variation of dielectric constant with temperature in a single crystal of $NaNbO_3$.

mean for all specimens. It is not possible to produce a useful mean curve because of the differences in the transition temperatures between different specimens. The general form of fig. 5 is however well reproduced and at points remote from the major transitions the following mean values were obtained :

$E \parallel$ to 'c' at room temperature 670 ± 13 measured on 9 crystals,
$E \perp$ to 'c' at room temperature 76 ± 2 measured on 3 crystals,
$E \parallel$ to 'b' at 530°C 926 ± 63 measured on 15 crystals.

The following features of the dielectric constant variation appear to be of particular interest.

(i) There is no evidence of any major discontinuity in ϵ above 350°C, only minor changes appear at 470°C and 520°C.

(ii) The anisotropy detected optically above 350°C is also evident in the ϵ measurements.

(iii) The rapidly rising value of $\epsilon_{||}$ at low temperature suggests that there is a further structure change below—209°C.

Measurements at Higher Fieldstrength

With fields applied either parallel or perpendicular to the *c* axis at room temperature, there is no significant departure from a linear relation between electric polarization and field for fieldstrengths up to 80 kv/cm. Above this fieldstrength breakdown frequently occurs, but 8 samples have been observed with fields greater than 90 kv/cm.

Fig. 6

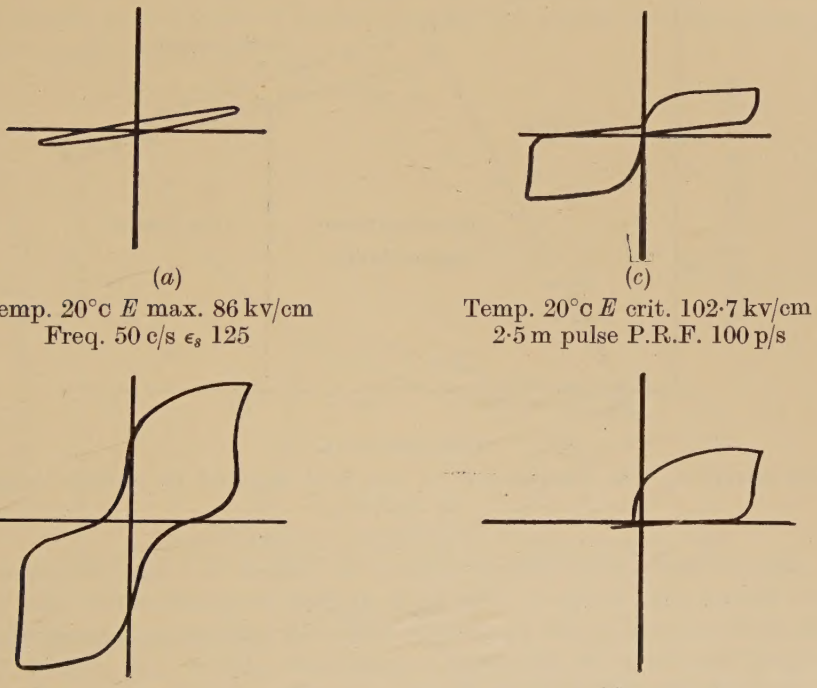

(*a*) Temp. 20°C E max. 86 kv/cm Freq. 50 c/s ϵ_s 125

(*c*) Temp. 20°C E crit. 102·7 kv/cm 2·5 m pulse P.R.F. 100 p/s

(*b*) Temp. 20°C E crit. 91 kv/cm P_i 8·75 μc/cm^2. Freq. 50 c/s

(*d*) Temp. 20°C E crit. 101·4 2·5 m pulse P.R.F. 50 p/s

Electric hysteresis in $NaNbO_3$ for fields applied perpendicular to the orthorhombic *c* axis.

At these fieldstrengths, five cystals which had the *c* axis perpendicular to the field direction all gave evidence of double hysteresis. The effect with a 50 cycle a.c. field is shown in figs. 6 (*a*), (*b*). Up to a critical fieldstrength, the $P \propto E$ relation is approximately linear. Increasing the

maximum field above this value, a double hysteresis loop opens out, the curve reverting to a straight line when the maximum field is reduced below the critical value.

The mean value for the critical field measured at 50 cycles in the five specimens was 87·5±4 kv/cm, and the maximum value of extrapolated polarization 11·4μ coulombs/cm^2. The effects of pulsed fields is shown in figs. 6 (*c*), (*d*).

In the three crystals which had '*c*' parallel to the field direction, no hysteresis effects were observed at room temperature up to electric breakdown at about 100 kv/cm. One sample which had regions of parallel and symmetric extinction under the electrode also gave evidence of double hysteresis, though the magnitude of the step in polarization at the critical field was reduced. There was no evidence of any motion of the twin boundaries.

Fig. 7

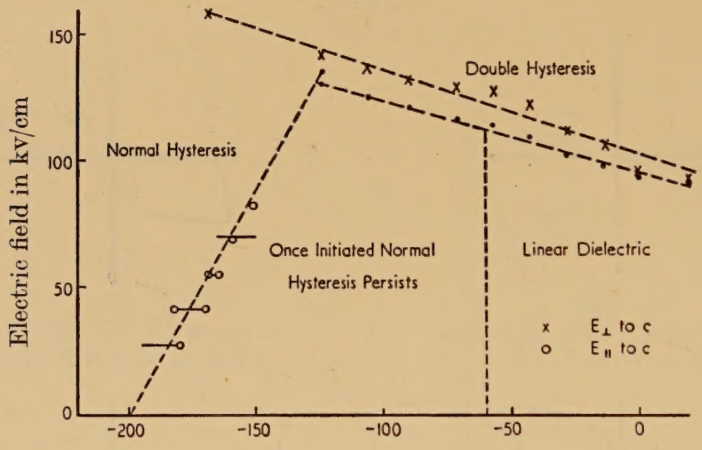

The variation with temperature of the field required to produce hysteresis in $NaNbO_3$.

The variation with temperature of the effects of a high 50 cycles field are summarized in fig. 7. For fields applied perpendicular to the *c* axis, the field required to initiate double hysteresis appears to increase approximately linearly with decreasing temperature.

With the field applied parallel to '*c*', the linear behaviour is maintained down to approximately −120°c. Below this temperature the crystal behaves in a linear manner up to a critical fieldstrength, above which a *normal* hysteresis curve appears. The onset of hysteresis is sudden and once initiated persists to low fieldstrength, the linear polarization field relation only being restored if the specimen is reheated above −55°c. Hysteresis has been observed in all samples of this orientation which have been tested, the maximum value of the extrapolated polarization being 11·7μc/cm^2.

Hysteresis is also observed in crystals of mixed orientations, but the magnitude of the remanent polarization is reduced. The most perfect specimen with '*c*' oriented perpendicular to the field which we have measured at low temperature gave clear evidence of double hysteresis down to −169°C, and at −193°C the normal hysteresis curve gave a value of extrapolated polarization of less than 0·4 μc/cm^2.

The changes produced by a high a.c. field applied parallel to the '*c*' axis are also evident when the weak field dielectric constant is measured after the application of a field (fig. 8). The reduction in $\epsilon_{||}$ appears to be permanent and there is no measurable increase after 24 hours at low temperature. The return change does not occur until −55°C. It was thought that this long thermal hysteresis might be due to the forced transition, but one sample has been observed in which the change occurs pontaneously at −145°C on cooling, and −40°C on re-heating. A preliminary optical examination of this specimen reveals no major change at −145°C. There is a minor change in the extinction, which would be consistent with a shear of the (001) plane, but further work is necessary to check these properties.

Fig. 8

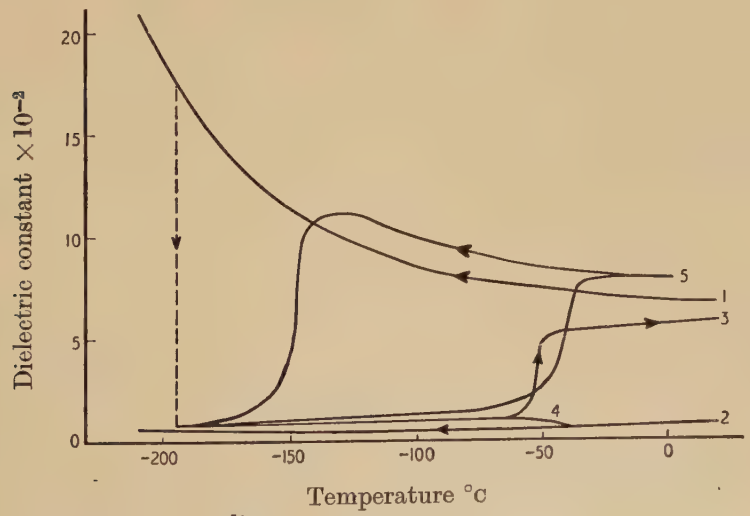

(1) Field || to *c*, cooling.
(2) Field ⊥ to *c*, cooling.
(3) Field || to *c*, heating after the application of 60 kv/cm at −195°C.
(4) Field ⊥ to *c*, heating after the application of 71 kv/cm at −195°C.
(5) Spontaneous change observed in one crystal.

The variation of dielectric constant with temperature in $NaNbO_3$ at low temperature.

Some measurements have also been carried out on less perfect semiconducting specimens (tan δ ranging from 2·0 to 0·05 at 50 cycles/sec). The trace from a conventional 'Sawyer and Tower' display on these crystals shows a wide ellipse due to the integrated conduction, which

however cannot be compensated by a phase shift of the x voltage (fig. 9 (*a*)). This is found to be due to the rapid non-ohmic rise of conduction with applied field (fig. 9 (*b*)).

Increasing the cycling frequency reduces the conduction effect and at frequencies above 10 kc/sec even the poorest samples can be compensated to give a linear $P \propto E$ of slope comparable to the values obtained on the more perfect crystals (fig. 9 (*c*)).

Fig. 9

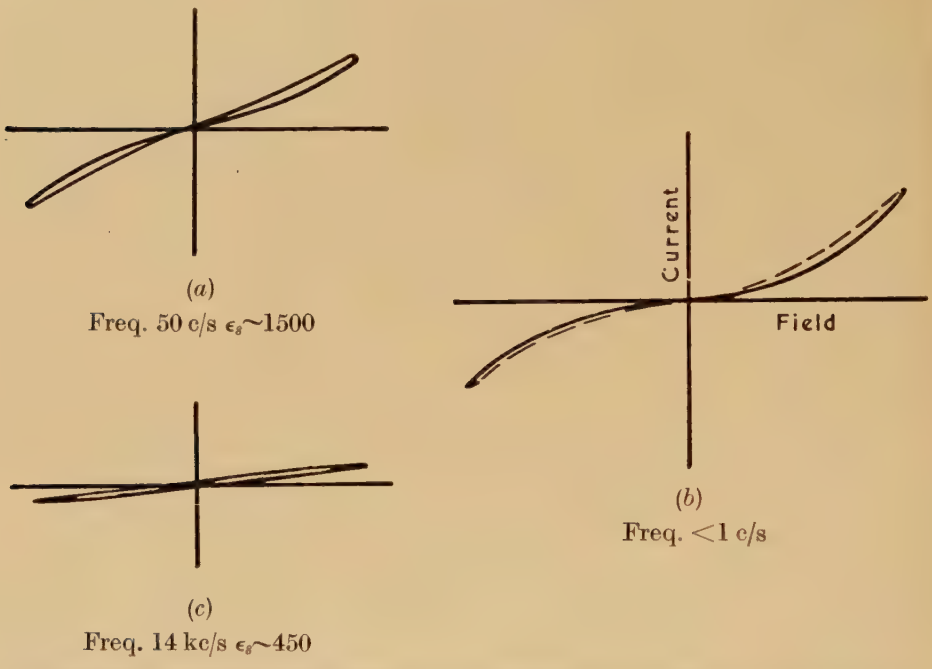

(*a*)
Freq. 50 c/s $\epsilon_s \sim 1500$

(*b*)
Freq. <1 c/s

(*c*)
Freq. 14 kc/s $\epsilon_s \sim 450$

The effects of increasing frequency on the hysteresis figure from semi-conducting $NaNbO_3$.

Increasing the applied field, the current continues to rise rapidly until electric breakdown shatters or melts the specimen or removes the electrode contact. If however, the breakdown current is limited by a high series resistance the breakdown is modified. As the crystal resistance collapses, the current increase through the external resistance reduces the voltage applied. Limited in this manner the breakdown is reproducible and is accompanied by optical changes in the specimen. The optical changes only occur transiently at the maximum fieldstrength and it has not been possible to determine the exact nature of the effects. It is, however, certain that this is not a simple migration of twin boundaries increasing the area of a particular orientation under the electrode. The breakdown field varies widely between different specimens and reproducible effects have been produced from 4 kv/cm to 70 kv/cm.

Once the specimen has been broken down in this manner, it becomes water sensitive. The weak field powerfactor increases with time and the specimen may be made to produce a type of hysteresis figure at low fieldstrength (fig. 10). The nature of this moisture effect has not been completely determined, but the looping may be eliminated by drying the sample in a desiccator (fig. 10). The spurious effect can be quite large, and in one case, an apparent extrapolated polarization of the order of 33 μc/cm^2 was observed.

Fig. 10

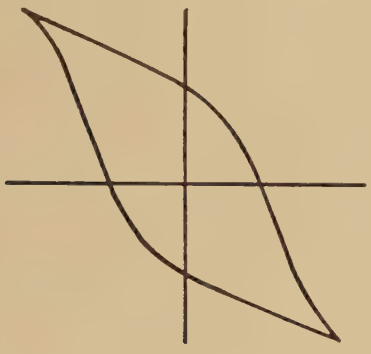

(*a*)

Temp. 20°c *E*, max. 27·8 kv/cm
P_i 33·0 μc/cm^2, P 32·0 μc/cm^2
Freq. 50 c/s

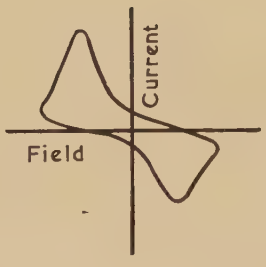

(*c*)

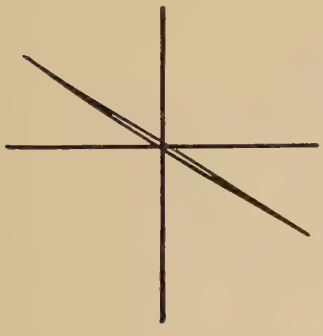

(*b*)

Temp. 20°c, *E* max. 18·6 kv/cm
ϵ_s 1113, Freq. 50 c/s.

(*a*) Electric hysteresis in a damp crystal.
(*b*) The same crystal after drying, amplification ×10.
(*c*) The current during hysteresis.

The effect of moisture on the properties of $NaNbO_3$, after previous electric breakdown.

§ 5. Discussion of Results

The electrical measurements at high fieldstrength on the more perfect crystals are in agreement with the structure determined by Vousden (1951 b). The double hysteresis curves obtained when the field is applied

perpendicular to the orthorhombic '*c*' axis and the absence of any hysteresis effects for fields parallel to '*c*' show that the normal state is not spontaneously polarized. The rapid rise of polarization at the critical fieldstrength in the double hysteresis curves also suggests that it is possible to reorient one of the sets of anti-parallel ion displacements in the (001) plane. There is evidence of a similar type of polarization change in $PbZrO_3$ (Shirane *et al.* 1951) but this only occurs in the ceramic material close to the Curie temperature at 230°c. Sodium niobate would appear to be the first material in which it is possible to effect this reorientation at temperatures remote from any spontaneous change, and clearly, in this structure the difference in free energy between ferroelectric and anti-ferroelectric states must be very small.

The weak field dielectric constant values show that, as has been demonstrated for a ferroelectric material of Perovskite structure (Merz 1949), it is easier to increase the intrinsic polarization perpendicular to the direction of spontaneous displacement, than it is to increase the polarization in the direction of the displacements. In contrast to the ferroelectric, however, since $NaNbO_3$ is not polar, there is no tendency for the spontaneous displacement system to rotate into the field direction by twin boundary motion, so that the high linear dielectric constant persists to very high fieldstrengths.

The ferroelectric properties at low temperature might be produced by a spontaneous reorientation of one of the anti-parallel sub-lattices, as in the electrically forced transition in the double hysteresis curve. Such a spontaneous rotation, however, appears improbable. The electric field required to induce the change at room temperature is high and increases with decreasing temperature, also, the maximum ferroelectric hysteresis occurs when the field is applied parallel to the '*c*' axis.

It appears more likely that there are additional ferroelectric displacements of the ions in a direction perpendicular to the (001) plane. A polarization in this manner, along the '*c*' axis of the orthorhombic unit, would be expected to produce an additional shear in the (001) plane and there is some optical evidence to suggest that this occurs. The presence of both ferroelectric and anti-ferroelectric displacements would also explain the very peculiar distorted hysteresis curves which occur in specimens of mixed orientation near −120°c, and appear to be compounded from both normal and double hysteresis curves.

There appears to be no intrinsic reason why both ferroelectric and anti-ferroelectric displacements should not occur simultaneously and it may be that at low temperature $NaNbO_3$ is the electrical analogue of a ferrimagnetic material.

The x-ray data (Wood 1951) show that the multiple unit cell persists to high temperature. We have not been able to confirm the anti-ferroelectric hysteresis at high temperatures, due to increasing conduction, but the balance of evidence suggests that the pseudo-tetragonal structure above 350°c is also anti-ferroelectric. The almost linear variation of

optical strain with temperature below 500°c, in both pseudo-tetragonal and orthorhombic structures also suggests that the onset of anti-ferroelectricity is a second order change and, as has been demonstrated by Kittel (*loc. cit.*), this would account for the absence of any major discontinuity in the dielectric constant at the transition temperature.

The change from orthorhombic to tetragonal symmetry in ferroelectric $BaTiO_3$ is accomplished by a rotation of the spontaneous polarization from a '[101]' to an [001] direction. In the higher temperature form '*c*', the unique polar axis has fourfold symmetry, and the structure is tetragonal.

In orthorhombic $NaNbO_3$ the ion displacements are again along '[101]'. The ion in different (001) planes are, however, displaced in different directions, the Nb ions for example occurring in double layers displaced alternately in opposition (Vousden 1951 b).

If, as we suppose, the antiferroelectric character is preserved above 350°c, it is probable that the structure will again consist of layers with anti-parallel displacements. Clearly then, there is no fourfold symmetry axis in the '*c*' direction and the symmetry can not be tetragonal. The very small optical anisotropy in the (001) plane is probably a measure of the difference in spacing between similar ions displaced in the same direction along '*c*' (ions in the same sheet) and similar ions displaced in opposite directions along '*c*' (ions in adjacent sheets) and again reflects the very small difference between ferroelectric and anti-ferroelectric linkage.

A complete investigation of the properties of the less perfect crystals has not been attempted and this work is only mentioned as it may help to explain some of the electrical properties which have been previously reported. To avoid confusion, however, it must be stressed that in no specimen have we observed any optical change to be produced by an electric field, except in the region of high conduction immediately preceding electric breakdown and that even after repeated breakdown, normal hysteresis was only observed at room temperature in wet crystals.

A more complete correlation of the properties of sodium niobate has been attempted, by extending the Kittel–Devonshire treatment of anti-ferroelectricity (Kittel, *loc. cit.*, Devonshire 1954) to the case of polarization in three dimensions in a pseudo-cubic crystal. This enables a direct correlation of the polarizations, susceptibilities and transition tempera tures and an indirect correlation with the optical strain. It is hoped to publish the results of this treatment shortly.*

The authors wish to express their sincere thanks to Professor E. C. Stoner, under whose direction this work has been carried out and to the

* *Note added in proof.*—The authors' attention has been directed to a recent article by G. Shirane, R. Newnham and R. Pepinsky (*Phys. Rev.*, 1954, **96**, 581) giving x-ray, optical and electrical data for $NaNbO_3$. Where the measurements are comparable, our results appear to be in reasonable agreement, and these authors also find no evidence of ferroelectricity at room temperatature.

British Electrical and Allied Industries Research Association for permission to publish this article. They are also indebted to the Imperial Chemical Industries Ltd. (L. E. C.) for a research fellowship and to the Ministry of Education (B. J. N.) for a maintenance grant.

References

Cross, L. E., and Nicholson, B. J., 1954, *Research Correspondence*, 7.
Devonshire, A. F., 1954, *Advances in Physics*, **3**, 85.
Kittel, C., 1951, *Phys. Rev.*, **82**, 729.
Matthias, B., 1949, *Phys. Rev.*, **75**, 1771.
Matthias, B., and Remeika, J. P., 1951, *Phys. Rev.*, **82**, 727.
Merz, W. J., 1949, *Phys. Rev.*, **76**, 1221.
Shirane, G., Sawaguchi, E., and Takeda, A., 1951, *Phys. Rev.*, **84**, 476.
Vousden, P., 1951 a, *Acta Cryst.*, **4**, 373; 1951 b, *Ibid.*, 545.
Wood, E. A., 1951, *Acta Cryst.*, **4**, 353.

LVI. *Notes on the Energy Spectra and Frequencies of Production of V^0-particles*

By D. B. GaythER
The Physical Laboratories, The University, Manchester*

and C. C. Butler
The Physics Department, Imperial College, London†

[Received February 11, 1955]

Abstract

An analysis is made of the decays of 45 V^0-particles associated with nuclear interactions in a lead plate mounted inside a cloud chamber. Data are given on the energy spectra of the Λ^0- and θ^0-particles and possible sources of experimental bias are discussed. Distributions are also given of ϕ, the angle between the path of the primary of the interaction in which a V^0-particle is produced and the line of flight of the V^0-particle in the laboratory frame of reference. The ϕ-distribution for Λ^0-particles is found to be similar to that of the grey particles produced in nuclear interactions while that for the θ^0-particles is similar to the angular distribution of the shower particles. Both Λ^0- and θ^0-particles are found to occur at frequencies of about 3·0% of the charged π-mesons in nuclear interactions of mean energy (5–10) Bev. A discussion is given of the data in terms of possible modes of production.

§ 1. Introduction

Observations show that the decays of V^0-particles are frequently associated with nuclear interactions, although little is known about their modes and frequencies of production by different types of primary particle. It has been demonstrated by several groups that V^0-decays are generally coplanar with their apparent points of origin. This shows not only that V^0-particles probably undergo two-body decay, but also that they are directly produced in nuclear interactions, or are the products of other particles which have a mean lifetime of less than 10^{-11} sec.

It has been known for some time that V^0-particles are produced with a frequency of the order of 1% of that of charged π-mesons produced in nuclear interactions. If we assume that V^0-particles are produced singly, this frequency indicates that their mean lifetimes should be about 10^{-21} sec, whereas the measured lifetimes are all about 10^{-10} sec. Pais (1952) has suggested that these facts can be reconciled by assuming that a V^0-particle is produced together with some other heavy unstable particle.

* Now at A.E.R.E. Harwell.
† Communicated by the Authors.

Fowler *et al.* (1953, 1954) have obtained convincing evidence for the pair production of V^0-particles. They observed four events showing the production of V^0-particles in the collision of 1·5 Bev π-mesons with the protons in a hydrogen filled diffusion chamber. In two events a Λ^0-particle is seen to decay, and if it is assumed that only one other particle is produced, the dynamics of the events show that it must be a K^0-particle of mass about 1200 m_e. In each of the remaining two events, a Λ^0- and θ^0-particle are seen to decay. The dynamics of these events are consistent with the production scheme

$$\pi^- + P \rightarrow \Lambda^0 + \theta^0. \qquad . \; . \; . \; . \; . \; . \; . \; (1.1)$$

In the present experiment, 45 V^0-decays have been observed which are associated with nuclear interactions in a lead plate mounted inside a cloud chamber. The classification of these events has been described in a previous publication (Gayther 1954) : it was assumed that the decays were produced only by Λ^0- and θ^0-particles. In the following sections, the energy spectra, frequencies of production, the various angular relationships between the decays and their points of origin, and possible modes of production are discussed.

§ 2. Experimental Arrangement

The apparatus has been described in a previous paper (Gayther 1954). The cloud chamber has an illuminated volume of approximately $40 \times 30 \times 20$ cm^3, and is operated without a magnetic field. The majority of the photographs were taken with the chamber containing an upper 4 cm lead plate and a lower 1·5 cm lead plate, and controlled by an arrangement of neutron counters which selected nuclear interactions of energy greater than several Bev in the 4 cm plate. Decays of V^0-particles which appeared to be produced in nuclear interactions in the 4 cm plate were selected for analysis.

§ 3. The Differential Energy Spectra of Λ^0- and θ^0-Particles

To obtain the energy spectrum of V^0-particles at production, the observed spectrum has to be corrected for the fact that a particular V^0-particle has a probability of decaying in the illuminated region of the chamber, which depends on its energy. Suppose a particle decays in the illuminated region, and the time of flight measured from its point of production to the point inside the chamber where it can just be identified and measured is t ; suppose also that the time measured from the same origin to the farthest point inside the chamber where the decay could still be analysed is T. Then the probability of having observed this V^0-decay, is simply the probability that it decays in the time interval t to T, which is

$$\mathscr{P}(t, T) = \exp(-t/\tau_0) - \exp(-T/\tau_0), \quad . \; . \; . \; . \; (3.1)$$

where τ_0 is the mean life of the V^0-particles, and t and T are obtained

from the corresponding measured lengths l and L by using relations like

$$t = \frac{l}{3(P/M)}\, 10^{-10} \text{ sec}, \qquad \ldots\ldots \quad (3.2)$$

where P is the momentum, and M the mass of the V^0-particle. Hence the detection probability, $\mathscr{P}$, depends on the momentum of the particle. Each event must be weighted by the factor $W = 1/\mathscr{P}$ in order to obtain the energy spectrum. In this way, account is taken of the particles which decay before entering or after leaving the illuminated region. The extent to which $\mathscr{P}$ depends on the kinetic energy of a Λ^0- or θ^0-particle is shown in fig. 1. The curves apply to the present chamber, and were obtained

Fig. 1

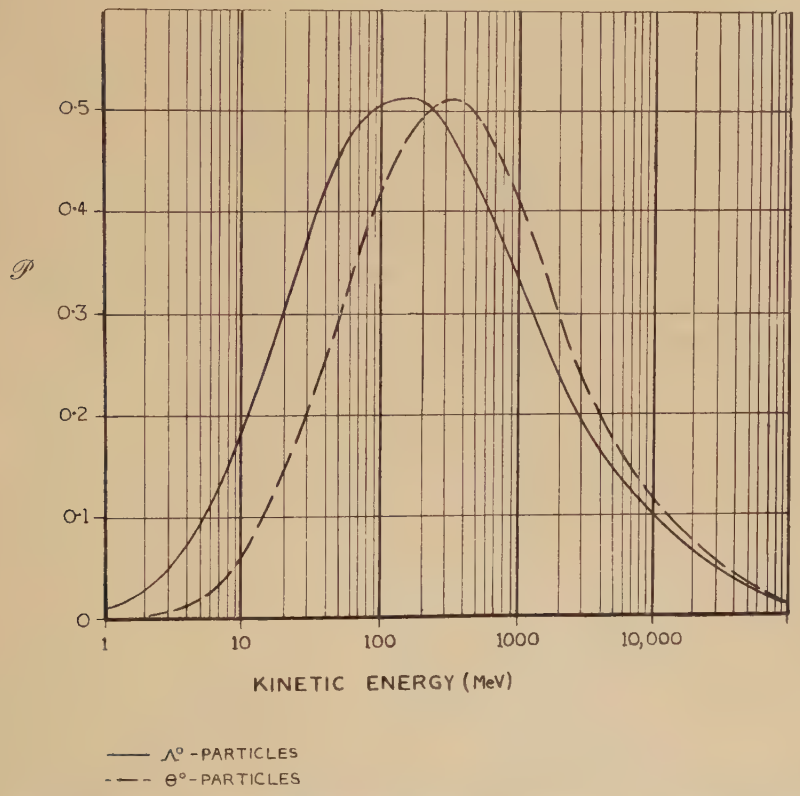

Average detection probability as a function of energy for Λ^0- and θ^0-particles.

by using the observed mean values of l and L which were 2·5 cm and 11·5 cm respectively for Λ^0-particles, and 2·85 cm and 14·5 cm for θ^0-particles. This assumes that l and L are not themselves functions of the energy of the V^0-particles. This is not strictly correct, since results which are discussed later show that low energy Λ^0-particles are often emitted backwards in the laboratory system, and because of the chamber geometry these particles will have smaller values of L than those emitted in the

forward direction. However, the value of $\mathscr{P}$ at low energies depends largely on l, which should not differ appreciably for forward or backward moving particles. High energy Λ^0-particles are generally emitted in the forward direction, and the chosen value of L may be too small with the result that $\mathscr{P}$ is slightly underestimated. The θ^0-particles observed in this experiment were well collimated in the forward direction, and therefore L probably does not depend to a marked extent on their energy. In calculating the curves shown in fig. 1 it was assumed that the mean lifetimes of Λ^0- and θ^0-particles are $3{\cdot}7\times10^{-10}$ sec and $1{\cdot}7\times10^{-10}$ sec respectively. The curves show that the average maximum probability of detection is about 0·5 for both types of V^0-particles, and occurs at an energy of 150 Mev for Λ^0-particles, and 350 Mev for θ^0-particles. The

Fig. 2

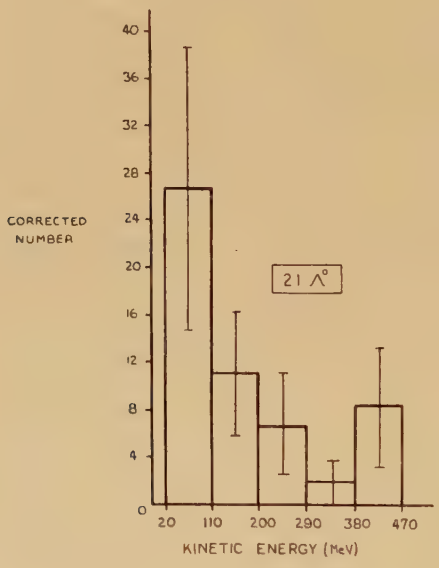

Energy spectrum of Λ^0-particles.

value of $\mathscr{P}$ falls to half the maximum value at 15 Mev and 2 Bev for Λ^0-particles, and 40 Mev and 3 Bev for θ^0-particles. So far, no allowance has been made for the possibility that V^0-particles may interact in the lead plate, and not be observed. The cross section would probably be geometrical at high energies, and since each particle traverses on the average 2·2 cm of lead, before entering the illuminated region, the fraction not observed due to interaction would be only 0·14.

The momenta, P, kinetic energies, E, and weighting factors, W, are listed in the first three columns of table 1 for Λ^0- and θ^0-particles. The corrected energy spectrum for the 21 identified Λ^0-particles is shown in fig. 2. The standard deviation in the corrected number of events in each energy interval is represented by the vertical line, and is given by $(\Sigma W_r^2)^{1/2}$, where W_r is the weighting factor of the rth event in the

interval. The observed Λ^0-particles all had energies inside the range (20–470) MeV, and outside this range no direct information about the energy spectrum can be obtained.

Before discussing the shape of the energy spectrum, known sources of bias in the results must be considered. It is shown in § 4 below that the energy of the Λ^0-particles decreases as ϕ, the angle of emission with respect to the direction of the primary particle making the nuclear interaction, increases. Now the presence of the lead plate inside the chamber effectively prevents the observation of many events with ϕ in the range (70–110)°. These decays usually have energies of 100 MeV or less so that the low energy end of the spectrum given in fig. 2 is probably underestimated.

Owing to the very limited amount of data available, the functional form of the energy spectrum cannot be determined. After allowing for the bias effects already discussed, it seems very probable that the spectrum rises below 100 MeV and may continue to do so below 20 MeV.

Reynolds and Treiman (1954) and James and Salmeron (1955) have obtained data on the energy spectrum of Λ^0-particles. Reynolds and Treiman did not apply lifetime and geometrical corrections to each individual decay but they concluded that *at least* 10% of Λ^0-particles have energies of less than 70 MeV. The corresponding figure for the present data is 40%. James and Salmeron have made an approximate measurement of the differential energy spectrum of Λ^0-particles covering a higher energy range than the present data. An extrapolation of this spectrum is consistent with the spectrum of fig. 2.

In general, because of their shorter lifetimes, the θ^0-particles which are observed to decay have higher velocities than the observed Λ^0-particles. The ten θ^0-decays were produced by θ^0-particles with energies in the range 18 MeV to 1·3 BeV.

§ 4. The Angular Distributions

The values of ϕ, the angle between the path of the primary of the interaction in which a V^0-particle is produced and the line of flight of the V^0-particle are given in column (4) of table 1.

Explanation of table 1.

Column (1) Momentum of V-particle; (2) Kinetic energy of V-particle; (3) Weighting factor≡1/probability of detection; (4) Angle between path of V-particle and path of primary of interaction; (5) Angle between decay plane and production plane; (6) Type of primary particle. S—charged secondary (probably π-meson) from another interaction. S(O)—neutral secondary (probably neutron) from another interaction, P—primary proton (unaccompanied in top section of chamber); (7) Number of penetrating particles and fast particles which are probably π-mesons.

Table 1. Production Data for 38 V^0-particles

Event	(1) P (Mev/c)	(2) E (Mev)	(3) W	(4) ϕ (deg)	(5) ψ (deg)	(6) Primary	(7) No. of shower particles
21 identified Λ^0-particles							
A 419	490	104	2·4	43	85	S	1
B 596	510	113	1·6	123	41	P	7
B2166	1120	461	3·7	16	0	P	6
B4312	720	215	2·7	60	15	P	10
C 389	380	62	2·2	36	61	P	8
C 718	1120	461	2·8	29	9	P	2
C1060	360	55	2·1	21	20	S(O)	6
D 532	520	117	3·0	109	46	P	11
D 721	1120	461	2·0	67	0	S	1
D1060	360	55	1·8	110	85	P	7
D2050	670	185	2·0	30	27	S	4
D2941	220	22	9·1	102	10	P	1
D5255	690	196	2·5	39	11	P	2
D6193	720	215	2·1	15	18	P	2
D6379	740	222	1·7	11	22	S	5
D6384	290	37	1·5	32	61	P	0
D6501	250	27	1·9	114	35	P	6
D7230	220	22	3·6	140	70	S	10
D7561	310	42	2·3	29	40	P	4
D8364	590	147	2·1	23	65	P	2
D8570	910	327	2·1	7	51	S(O)	7
7 probable Λ^0-particles							
A 680	330	50	1·7	—	—	S	8
A1337	780	250	1·3	31	—	S	6
B 979	450	85	1·7	48	—	S	10
B2695	450	85	1·7	21	—	P	10
D2153	1000	400	2·0	28	—	P	3
D3031	280	35	3·7	144	—	S	10
D7438	280	35	5·0	131	—	P	10
8 identified θ^0-particles							
A1208	150	18	4·6	18	57	S	0
B1843	300	63	4·3	20	74	S	1
B1990	250	45	3·0	76	6	S	10
D1967	290	61	2·5	29	18	P	2
D3587	1800	1300	2·7	32	42	S	6
D3754	170	30	16·7	16	46	P	7
D5123	230	50	3·0	21	50	P	1
D5155	490	220	1·5	12	37	P	1
2 probable θ^0-particles							
B3602	340	110	4·6	32	—	P	5
D 319	310	85	1·8	48	—	S	1

The ϕ distributions for the Λ^0- and θ^0-particles are shown in fig. 3. The first distribution includes six events which are only probable Λ^0-decays while two probable θ^0-decays are included in the second distribution. The classification of these events is referred to in § 6. Each event in the distribution is weighted by the appropriate factor W. Superficially the two distributions are different ; that for the Λ^0-particles resembles the angular distribution of grey tracks in stars while that for the θ^0-particles is very similar to the distribution for shower particles (Camerini *et al.* 1951). Before examining this conclusion, possible sources of bias must be considered.

Fig. 3

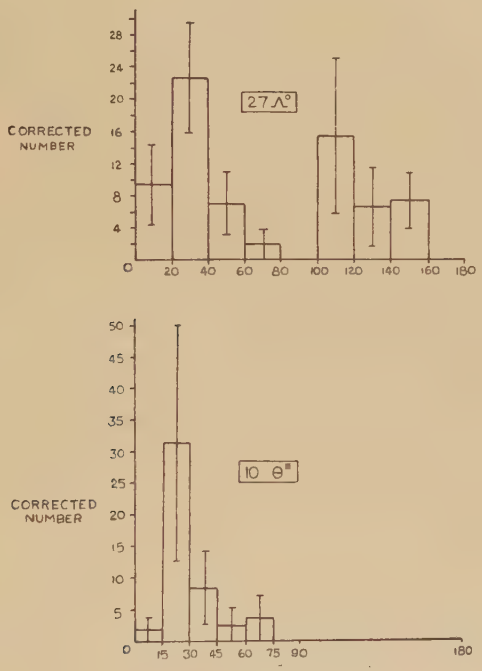

The ϕ-distributions.

The presence of the lead plate in the chamber generally prevents observations of ϕ in the range 70°–110°. The observed ϕ-distributions would also be affected if the energy spectrum of the V^0-particles depends on ϕ. In the case of the Λ^0-particles reference to table 1 shows that there is a tendency for only the lower energy Λ^0-particles to be emitted in the backward direction, in fact, the mean energy of the forward emitted Λ^0-particles is 211 Mev while the mean energy of the backward emitted decays is only 55 Mev. Figure 1 shows that, for Λ^0-particles, the probability of observation falls for energies below 50 Mev. Thus it seems likely that the number of events with $\phi > 90°$, compared with the number having $\phi < 90°$, has been underestimated.

Only a very small sample of data on θ^0-decays is available. No marked dependence of the energy on ϕ is observed but this cannot be regarded as significant. In practice, no upward moving θ^0-decay was observed. If upward θ^0-particles are produced with an average energy of 50 MeV, the appropriate curve in fig. 1 shows that the probability of observation of any one decay should be about 0·3. Owing to the small number of θ^0-decays observed, it is difficult to assess the precise significance of the probability although it is not much smaller than the value for many of the observed decays.

Taking into account bias effects we conclude that our results are consistent with the assumption that as many upward as downward moving Λ^0-particles were produced in the lead plate. The θ^0-particles were probably mainly projected in the forward direction but we cannot conclude that the angular distribution for these particles is certainly different from that of the Λ^0-particles.

Fig. 4

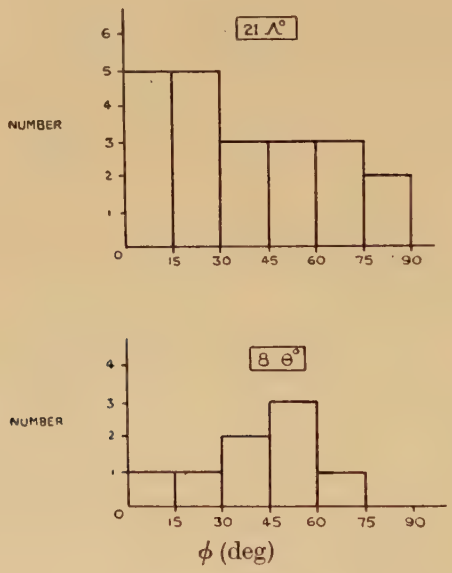

The ψ-distributions.

§ 5. Polarization Effects

We denote by ψ the angle between the plane containing the primary and the path of the V^0-particle and the plane including the decay secondaries. The observed values of ψ are given in column (5) of table 1, and the distributions are shown in fig. 4. The ψ-distribution for Λ^0-particles is not inconsistent with random orientation of the two planes, since then all values of ψ would be equally probable. There is a slight indication of a preference for small values of ψ, but this may be due to some unknown bias effect.

§ 6. The Frequencies of Production of Λ^0- and θ^0-particles

6.1. *The Numbers of Λ^0- and θ^0-particles at Production*

In the determination of a production frequency, account must be taken of the lifetime and geometrical biases by weighting each event by the factor W. When a mixture of particles is present, it is also useful to be able to separate all the particles into the known types. The classification of the 45 V^0-events has been described previously (Gaythe 1954) and it was found that 29 of these could be classified into the decays of Λ^0- and θ^0-particles ; these are the ' identified ' Λ^0- and θ^0-particles in table 1. It was found that event D319 probably represents the decay of a θ^0-particle, but this interpretation is not certain. This event is now assumed to be due to a θ^0-particle. For the remaining 15 events approximate measurements showed that seven of these decays were almost certainly produced by Λ^0-particles, and one was almost certainly produced by a θ^0-particle. These events with uncertain classification are called ' probable ' Λ^0- and θ^0-particles in table 1. Seven of the events cannot be classified by any method, and in what follows these events are assumed to be produced by Λ^0-particles, which form the majority of the V^0-events. Thus 35 events are assumed to be Λ^0-decays and 10 are assumed to be θ^0-decays, with the reservation that the number of Λ^0-particles has probably been overestimated. Anomalous decays have been ignored in the classification since they only form a small proportion of V^0-events. To determine the number of Λ^0- and θ^0-particles at production, the weighting factors W, must be found. This has already been done for the 29 identified V^0-particles. For each of the seven probable Λ^0-decays and two probable θ^0-decays, approximate values of l, L and P/M can be obtained which give fairly accurate values of W. For each of the seven assumed Λ^0-decays a value of W is assigned which is the mean value for identified Λ^0-particles. The last assumption is reasonable since the values of W for identified Λ^0-particles have only a small spread.

The numbers of Λ^0- and θ^0-particles at production are found to be :

$$\text{Number of } \Lambda^0\text{-particles } 90 \pm 17,$$

$$\text{Number of } \theta^0\text{-particles } 45 \pm 19.$$

These figures are influenced by the following effects :

(i) *Uncertainties in the Classification*

If we assume that the seven unclassified V^0-events are all produced by θ^0-particles instead of Λ^0-particles, the numbers at production become 72 Λ^0-particles and 75 θ^0-particles.

(ii) *The Different Detection Biases for the Two Types of Particles*

The number of low energy Λ^0-particles decaying in the plate is unknown, and this figure may be large if the spectrum shown in fig. 2 continues to rise below 20 MEV. The ϕ-distribution for Λ^0-particles shows that the corrected number may have to be increased by as much as 50% to account for particles emitted with ϕ close to 90°. Because of the large bias

against the observation of low velocity θ^0-particles, an unknown number must have decayed in the plate. Since the biases are different for the two types of particle, and the corresponding corrections to be applied to obtain the numbers at production are unknown, a definite conclusion cannot be reached. The numbers at production, however, are probably not inconsistent with the possibility that equal numbers of Λ^0- and θ^0-particles are produced, a fact which would support the hypothesis that they are produced in pairs.

Only one photograph shows the decays of two V^0-particles produced in a single nuclear interaction. Unfortunately, it is impossible to analyse both decays in detail. Leighton *et al.* (1953) and Fretter *et al.* (1953) have both observed several examples of the simultaneous production of two V^0-particles but they also were unable to reach any definite conclusions about the nature of the associated V^0-particles or whether they were always produced in pairs. The results of Fowler *et al.* (1954) and Thompson *et al.* (1954) are of much greater significance. However, even if the production scheme (1.1) of § 1, which explains the results of these workers, is assumed to be the exclusive mechanism for the production of V^0-particles, it is difficult to calculate the expected number of associated decays. This is due to the complex geometrical relations which must be considered and furthermore to the possibility, pointed out by Pais (1953) that both Λ^0- and θ^0-particles may sometimes decay into pairs of neutral particles and so leave no visible track in the chamber.

6.2. *Comparison with the Number of Shower Particles*

To account for the difficulty of recognizing V^0-events in large showers, a somewhat arbitrary separation of the nuclear interactions in the plate is made. A second scan of the photographs revealed no more V^0-events associated with nuclear interactions in which the estimated number of shower particles was less than about eight, whereas in the larger interactions several additional decays were noticed. It is therefore assumed that the efficiency of the observer for the detection of V^0-events produced in interactions with an estimated number of shower particles less than or equal to eight approached unity, and the following discussion refers to V^0-particles produced in such interactions. Showers with large electronic components are also excluded.

A track emerging from an interaction in the upper plate can only be identified with certainty as a fast proton or π-meson if it is observed to penetrate the lower plate. For this reason the comparison is made between the number of penetrating particles and the number of V^0-particles whose trajectories below the lower plate traverse the illuminated region. We denote by n_s the number of such identified shower particles from an interaction; since some of the V^0-events are emitted backwards, n_s also includes an estimate of the number of backward emitted shower particles. The frequency distributions of the number of events with a given value of n_s are given in table 2.

Table 2. Multiplicity Distributions

n_s	0	1	2	3	4	5	6	7	8	>8
(1) No. Interactions	458	470	323	179	115	81	31	37	20	275
(2) Corrected No. interactions	949	508	323	179	115	81	31	37	20	275
(3) No. V^0-events	4	7	4	5	4	1	5	1	1	10
(4) Corrected No. V^0-events	10·5	25·1	10·1	10·5	11·6	2·6	26·2	1·6	1·7	29·6

Row (2) of the table contains a correction for the number of low multiplicity interactions which fail to satisfy the selection criteria for nuclear interactions. The corrected number of V^0-events in Row (4) of the table are obtained by weighting each event by the factor W.

The total number of n_s particles observed in all the interactions with $n_s \leqslant 8$ is denoted by N_s and is equal to 3161. The corrected total number of V^0-events, N_{V^0}, is (100 ± 23), and the ratio at production is then

$$N_{V^0}/N_s \approx 3\%.$$

In the determination of this ratio only V^0-particles with angles of emission ϕ with respect to the primary particles within the same range as the corresponding angles for the shower particles have been considered. Since the true ϕ-distribution for V^0-particles is probably broader than that for the shower particles, the production frequency is underestimated, probably by about 20%. In addition, a number of low energy V^0-particles decay before entering the illuminated region. Since the form of the spectrum at low energies is unknown, and in any case is probably different for the two types of V^0-particle, a correction for this effect cannot be applied. Furthermore, the value of N_s does not include all the π-mesons produced in the showers since some of the low-energy π-mesons will fail to emerge from the lead plate or else fail to penetrate the lower plate. We consider that the production frequency must only be regarded as correct within a factor of about two.

The observed production frequencies of the two different V^0-particles are given in table 3.

Table 3. Frequencies of Production

Type of particle	No. produced	No. produced/N_s (%)
V^0	100 ± 23	3·2
Λ^0	58 ± 13	1·8
θ^0	42 ± 19	1·4

These figures refer to interactions for which $n_s \leqslant 8$, and comparison with the data of Camerini *et al.* (1951) shows that the majority of the interactions were produced by primaries with energies in the range (1–50) Bev, their mean energy being about (5–10) Bev. The work of Camerini *et al.* (1951) shows that π-mesons form about 60% of the shower particles in interactions of these energies, hence we obtain

$$N_{\Lambda^0}/N_{\pi^\pm} \approx N_{\theta^0}/N_{\pi^\pm} \approx 3\%.$$

6.3. *Dependence of Frequency of Production on the Energy of the Interaction*

Production frequencies of all the V^0-events for three different groups of nuclear interactions are given in table 4. The interactions with $n_s < 4$ have energies of only a few Bev while those with $n_s > 8$ probably have energies of greater than 50 Bev. The figures in table 4 show that the frequency of production of V^0-particles probably increases as the energy available in the nuclear interaction increases. Fretter *et al.* (1953) did not find such a marked effect but they pointed out that they found it difficult to identify the decays of V^0-particles in showers of high multiplicity. The above conclusion, on the increase of production of V^0-particles with the interaction energy, would be misleading if the average energy of the V^0-particles has a marked dependence on the average multiplicity of the interactions. Since there is a bias against detecting V^0-particles of less than 20 Mev (see § 3), this might account for the apparently low production in the low energy interactions. In order to consider this possibility, the average energies and average detection probabilities are given in rows (5) and (6) of table 4.

Table 4. Dependence of Production on n_s

(1) No. of shower particles n_s	$n_s < 4$	$4 \leqslant n_s \leqslant 8$	$n_s > 8$
(2) No. of interactions per V^0	33 ± 8	$6 \pm 2{\cdot}5$	$9{\cdot}5 \pm 3$
(3) No. of interactions per Λ^0	47 ± 14	13 ± 4	$10 \pm 3{\cdot}5$
(4) No. of interactions per θ^0	110 ± 48	12 ± 8	~ 93
(5) Average energy $\overline{E}$ (Mev)	125 ± 30	170 ± 60	70 ± 20
(6) Average detection probability $\overline{\mathscr{P}}$	$0{\cdot}36 \pm 0{\cdot}06$	$0{\cdot}28 \pm 0{\cdot}12$	$0{\cdot}34 \pm 0{\cdot}08$

Evidently $\overline{E}$ does not increase rapidly with n_s and the average detection probability $\overline{\mathscr{P}}$ is independent of n_s. Thus there is no evidence that low energy V^0-particles are produced preferentially in showers of low multiplicity. Hence the production of both Λ^0- and θ^0-particles probably does increase with the energy of the nuclear interaction.

§ 7. Discussion

Recently several groups of workers have obtained important results on production processes for V-particles. Fowler *et al.* (1954), Thompson *et al.* (1954), Dahanayake *et al.* (1954) and Debenedetti *et al.* (1954) have all obtained evidence for the associated production of hyperons and K-mesons, probably according to the following general scheme :

$$\pi+\mathrm{P}\rightarrow\mathrm{Y}+\mathrm{K}. \qquad . \ . \ . \quad (7.1)$$

Fowler *et al.* were the first to observe the simultaneous production of a Λ^0- and a θ^0-particle by the collision of a negative π-meson with a proton. They also obtained several photographs each of which probably shows the production of a charged hyperon with a charged K-meson. Debenedetti *et al.* (1954) have also studied an event in which a V^0-particle and a charged K-meson were emitted from the same star. Recently Block *et al.* (1954) have reported an event due to a proton which can be interpreted by the scheme

$$\mathrm{P}+\mathrm{P}\rightarrow\mathrm{Y}^+ +\mathrm{K}^+ +n, \qquad . \ . \ . \ . \ . \ . \ . \quad (7.2)$$

so that it is reasonable to suggest that neutral Y and K particles can also be produced by the interaction of nucleons.

It is interesting to consider whether the data described in this paper is in accord with scheme (7.1) or a more general form of (7.2). In § 6 it was shown that approximately equal numbers of Λ^0- and θ^0-particles are produced. A similar result was reported by Newth (1953). It is reasonable to expect that Y^0 and K^0 decays should occur with equal frequency if scheme (7.1) is the main source of V^0-particles. It is possible that both types of V^0-particle sometimes decay with neutral secondaries. This type of decay has not yet been detected ; if it occurs with the same frequency as the decay into charged secondaries for both types of V^0-particles, then the observed frequencies of production are consistent with scheme (7.1).

In the present experiment the Λ^0- and θ^0-particles were produced in high-energy nuclear interactions in lead nuclei. The probable identity of the particles responsible for the interactions is given in column (6) of table 1. More than half of the V^0-particles were produced by charged particles which were unaccompanied in the top compartment of the chamber. The majority of these were undoubtedly protons ; a small percentage, however, were probably π-mesons produced in interactions above the chamber and from which only one charged particle entered the chamber. Most of the remaining V^0-particles were produced by the interaction of π-mesons.

The interactions in which the V^0-particles were produced are all of high energy and many contain penetrating secondary particles (see column (7) of table 1). Thus some of the V^0-particles may have been produced in secondary interactions of π-mesons. Furthermore, the V^0-particles may undergo scattering before they emerge from the lead plate. These facts must be taken into account when analysing the data by means of scheme (7.1).

The simplest possible model for the production of the V^0-particles is built on the following postulates :

(i) The incident charged particles are protons or π-mesons.

(ii) The interaction occurs with a single target nucleon assumed to be at rest.

(iii) The V^0-particle is emitted without being scattered.

(iv) In addition to the V^0-particle, any number of other particles are produced.

Using this model and the data in table 1 and assuming reasonable minimum values for the energy of the primary particles, it can easily be shown that the majority of the Λ^0-particles were emitted *upwards* in the centre of mass system. It is interesting to note that in all the events seen by Fowler *et al.* (1954) and by Thompson *et al.* (1954), which are interpreted by scheme (7.1), the Λ^0-particles were also emitted in the upward direction in the centre of mass system.

James and Salmeron (1955) have recently investigated the dynamics of process (7.1) assuming the target nucleon to be at rest. Their calculated curves show that the large upward fraction of Λ^0-decays observed in the present experiment cannot be interpreted by scheme (7.1) if the Λ^0 does not suffer scattering after production. Of the eight Λ^0-particles emitted upwards in the laboratory system, only two were probably produced by π-mesons. The above conclusion, however, is not altered if the initiating particles are assumed to be protons instead of π-mesons.

The data on θ^0-particles given in table 1 can also be analysed using the calculations of James and Salmeron. If it is assumed that the incident particle is always a π-meson according to scheme (7.1), it is found that five out of ten decays have angles of emission ϕ and momenta such that the deduced momentum of the incident π-meson was less than the threshold value of about 1 Bev/c. Thus it is most probable that the θ^0-particles were produced in secondary collisions within the target nucleus or else by a complex process such as scheme (7.2).

In the previous paragraphs it has been assumed that the Λ^0- and θ^0-particles observed were produced in the first collision in the nucleus. No simple treatment of production in secondary interactions, of scattering effects, or of the effect of the Fermi energy of the nucleons within the target nucleus can be given. Thus it is still possible that scheme (7.1) is an important mechanism for the production of Λ^0- and θ^0-particles, although some of the data does not seem to be dynamically consistent with it.

Acknowledgments

It is a pleasure to thank Professor P. M. S. Blackett for his interest in our experiment. We have had several valuable discussions with Mr. J. A. Newth and Dr. K. H. Barker. We are indebted to Dr. J. Rosch, the Director of the Observatoire du Pic-du-Midi, for providing excellent laboratory facilities. We have received financial assistance from the Department of Scientific and Industrial Research, and one of us (D. B. G.) wishes to acknowledge the receipt of a maintenance grant.

References

Ballam, J., Harris, D. R., Hodson, A. L., Martin, W., Rau, R., Reynolds, G. T., and Treiman, S. B., 1954, private communication.

Block, M. M., Harth, E. M., Fowler, W. B., Shutt, R. P., Thorndike, A. M., and Whittemore, W. L., 1954, *Bull. Am. Phys. Soc.*, **29**, 7, 33.

Camerini, U., Davies, J. H., Fowler, P. H., Franzinetti, C., Muirhead, H., Lock, W. O., Perkins, D. H., and Yekutieli, G., 1951, *Phil. Mag.*, **42**, 1241.

Dahanayake, C., Francois, P. E., Fujimato, Y., Iredale, P., Waddington, C. J., and Yasin, M., 1954, *Phil. Mag.*, **45**, 855.

Debenedetti, A., Garelli, C. M., Tallone, L., and Vigone, M., 1954, *Nuovo Cimento*, **12**, 369.

Fowler, W. B., Shutt, R. P., Thorndike, A. M., and Whittemore, W. L., 1953, *Phys. Rev.*, **91**, 1287 ; 1954, *Ibid.*, **93**,, 861.

Fretter, W. B., May, M. M., and Nakada, M. P., 1953, *Phys. Rev.*, **89**, 168.

Gaythér, D. B., 1954, *Phil. Mag.*, **45**, 570.

James, G. D., and Salmeron, R., 1955, private communication.

Leighton, R. B., Wanlass, S. D., and Anderson, C. D., 1953, *Phys. Rev.*, **89**, 148.

Newth, J. A., 1953, *Report on Bagneres-de-Bigorre Conference.*

Pais, A., 1952, *Phys. Rev.*, **86**, 663 ; 1953, *Physica*, **9**, 869.

Reynolds, G. T., and Treiman, S. B., 1954, *Phys. Rev.*, **94**, 207.

Thompson, R. W., Burwell, J. R., Huggett, R. W., and Karzmark, C. J., 1954, *Phys. Rev.*, **95**, 661.

LVII. *Radioactive ^{184}Tantalum*

By F. D. S. Butement and A. J. Poë
Atomic Energy Research Establishment, Harwell*

[Received January 13, 1955]

Abstract

The new isotope ^{184}Ta has been produced and its decay characteristics determined as follows :

Half-life	8·7±0·1 h
β-energy (Mev)	0·15, 1·26
γ-energy (kev)	110, 160, 210, 240, 300, 405, 780, 890, 1180.

The mass assignment of this isotope was confirmed by its preparation by a (n, p) reaction on tungstic acid enriched in ^{184}W.

§ 1. Introduction

The isotope ^{184}Ta has not previously been reported, and this paper describes the preparation and properties of this radioisotope.

§ 2. Experimental Techniques

A mixture of radioactive tantalum isotopes was prepared by the irradiation of tungstic acid with fast neutrons produced by the bombardment of a beryllium target with 20 Mev protons. The principal yield was due to (n, p) reactions, with a much smaller yield from (n, pn) reactions.

The tungstic acid was dissolved in sodium hydroxide solution and the tantalum coprecipitated with ferric hydroxide by the addition of ferric chloride solution. The washed precipitate was dissolved in hydrochloric acid and a second precipitation carried out by the addition of a solution of inactive sodium tungstate (as a hold-back carrier) in sodium hydroxide. The precipitate was ignited to ferric oxide, fused with sodium hydroxide and potassium tantalate, and the product boiled with hydrochloric acid to precipitate tantalic acid, which was filtered out, washed, and ignited to provide a source of radiotantalum isotopes.

§ 3. Results

The sources showed beta-activities with half-lives of 8·7 hours, 5·0 days (^{183}Ta) and approximately 120 days (^{182}Ta).

The best values for the half-life of 8·7±0·1 h were obtained from five sources the decay of which was followed by counting those beta-particles

* Communicated by the Authors.

Fig. 1

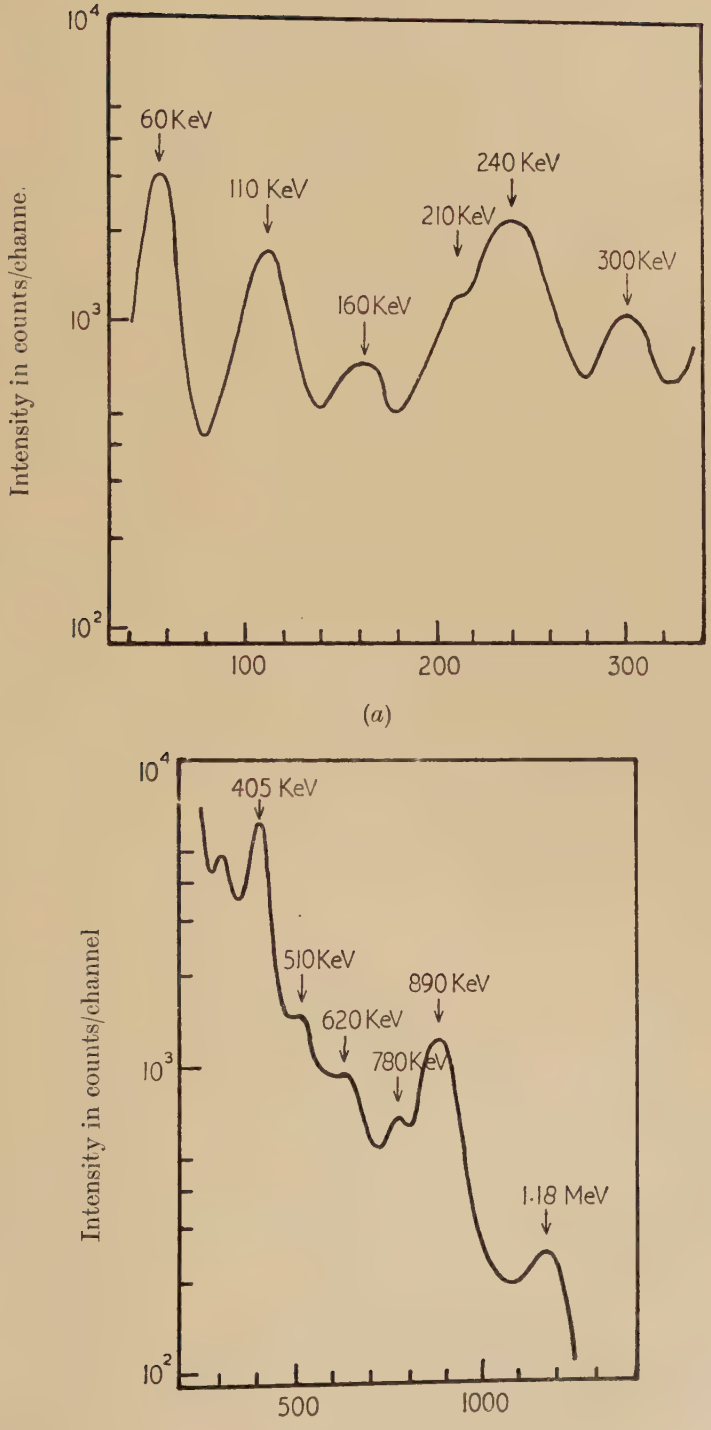

Gamma-ray energy spectrum of 8·7 h ^{184}Ta

which passed through 228 mg/cm^2 of aluminium, this being sufficient to absorb all the beta-particles from longer-lived activity present. The long-lived background activity was then reduced to that due to inefficiently counted gamma-rays.

The mass assignment of the 8·7 h activity was made by the use of tungstic acid enriched in the tungsten isotope of mass 184. Equal weights of normal and enriched tungstic acid were irradiated and tantalum samples separated and counted under identical conditions. The irradiations were monitored with the 12·8 hour activity induced in thin copper foils placed between the samples and the neutron source. The ratio of the abundances of each of the tungsten isotopes of mass 180, 182, 183, 184 and 186 in the enriched sample to the abundances of the corresponding isotopes in the normal sample was 0·5, 0·045, 0·11, 2·97 and 0·21 : 1 respectively. The ratio of the yields of the 8·7 hour activity from the enriched sample to that from the normal sample was 3·06 : 1, a value corresponding to the enrichment of ^{184}W, and indicating that the activity is ^{184}Ta produced by a (n, p) reaction.

The maximum beta-particle energy was found to be 1·20 MeV from Feather analysis of aluminium absorption curves. Applying Behrens' nomogram (Behrens 1950) to the same curves an energy of 1·4 MeV was obtained. The average of seven values obtained from Fermi plots derived from the beta-particle spectra measured with an anthracene scintillation spectrometer was 1·26 MeV, all the results lying within 0·07 MeV of this value. Fermi beta-disintegration functions calculated by Bleuler and Zünti (1946) were used. The aluminium absorption curves also indicated a low energy component of about 0·15 MeV amounting to 30–40% of the total counting rate. The absorption curve of beta-particles in coincidence with gamma- and x-rays was identical with the normal absorption curve. The 1·26 MeV beta-transition therefore does not go to the ground state of the tungsten nucleus.

The gamma-ray spectrum was examined with the scintillation spectrometer, the results being shown in figs. 1 (*a*) and 1 (*b*), corrections for longer-lived gamma-rays having been applied. These may be interpreted to indicate radiations of energies 405, 890, 240, 1180, 60, 300, 110, 780, 160 and 210 kev with the approximate relative intensities 10 : 9 : 6 : 5 : 4 : 3·5 : 3 : 1·7 : 1 : 1 respectively. The 60 kev component is presumably a K x-ray. The 510 and 620 kev components are most probably Compton scatter peaks from the 780 and 890 kev gamma-rays. The 780 kev peak cannot be the Compton peak of the 1180 kev gamma-ray which has a value of about 900 kev and is masked by the 890 kev photo-electric absorption peak.

References

Behrens, D. J., 1950, *A.E.R.E. Report* T/M 6.
Bleuler, E., and Zünti, W., 1946, *Helv. Phys. Acta*, **19**, 375.

LVIII. *Some Vibrational Properties of Solid Helium*

By D. J. Hooton*
Department of Mathematical Physics, University of Edinburgh†

[Received November 6, 1954]

Summary

A series of experimental measurements on the specific heat and other vibrational properties of solid helium, due to J. S. Dugdale and F. E. Simon, are here given a theoretical basis in terms of a new form of harmonic lattice dynamics, due originally to Born, and further developed in two previous papers by the present author. The relative magnitude of the zero-point energy in solid helium is such that the customary lattice dynamics, which takes no account of the anharmonic terms in the actual lattice motion, breaks down (the proper frequencies becoming negative); the new theory provides a harmonic approximation with frequencies anharmonically defined, and can be used over the full range of molar volumes which can be achieved in solid helium. The results are expressed in terms of a Debye approximation with characteristic temperature θ; this θ differs in absolute value from the purely empirical Debye-type parameter introduced by Dugdale and Simon, but otherwise has similar properties. The significance according to this theory of the Grüneisen equation of state found by these authors is fully discussed. Some vibrational properties on the melting curve, treated by C. Domb, are reconsidered from a properly anharmonic point of view.

§ 1

The vibrational properties of solid helium are almost completely outside the scope of the usual harmonic lattice dynamics. Domb (1952) has shown that near 0°K the zero-point energy produces at melting a relative displacement of the atoms from their lattice sites of about $\frac{1}{5}$, whereas in normal solids the displacement is never more than about $\frac{1}{10}$; such strong vibrational energy must be regarded as essentially anharmonic. Coupled with a relatively weak cohesive potential—about two-thirds the zero-energy between 0 and 20°K—this strong vibrational anharmonicity produces a large expansion of the lattice from its static volume (at a given pressure), so that the characteristic vibrational frequencies of the

* Communicated by Professor M. Born, F.R.S.

† Completed in the Institut für theoretische Physik der Universität, München, during tenure of a Leverhulme European Scholarship, 1954.

harmonic theory become imaginary at easily attainable molar volumes (Domb, *loc. cit.*).

The theory developed from a method due to Born (1951) in two preceding papers (Hooton 1955a, b, referred to as I and II) provides a way of treating such strongly anharmonic vibrations in terms of a generalized harmonic approximation to which the Debye theory can be adapted. We shall here use the previous results to describe the specific heat at constant volume, as measured by Dugdale and Simon (1953), together with some properties of solid helium at melting; the zero-energy will also be calculated by this method and used (following Dugdale and Simon) to give an estimate of the lattice potential.

§ 2

The helium lattice is generally considered to be of the close-packed hexagonal structure, which has very similar properties to the face-centred cubic. A phase transition in solid helium at about 15°K (12 cm³ molar volume) is described by Dugdale and Simon, who consider it to be a transition from the hexagonal to the cubic lattice, and it can be seen from their results that the accompanying thermodynamical changes are relatively very small. Because of this practical equivalence it is sufficient to use the face-centred cubic structure for thermodynamical purposes, especially since the lattice potential is not the major influence in the solid; for the present work we then have the advantage that the symmetry of the cubic structure is close to the isotropic symmetry assumed in II, so that the Debye formulae developed there can be used with some confidence. Thus the molar volume V and the next-neighbour distance a will be related by

$$V=Na^3/\sqrt{2}. \qquad \ldots\ldots\ldots \quad (1)$$

The lattice potential U_0 can then be evaluated once the inter-atomic potential $\phi(r)$ is known (central forces may be used for the inert gas atoms); this will be done in a later paper in terms of the most recent* determination of ϕ by Yntema and Schneider (1950)—the result is indicated in fig. 6 where a Lennard-Jones approximation has been used (see remarks below).

To apply the thermodynamical formulae (II, eqns. (5), (6)) we need to know the function f, or f_V, defined at each volume as an average over the lattice spectrum of the quantity

$$f_j=1-\frac{\omega_j^{02}}{\omega_j^2}, \qquad \ldots\ldots\ldots \quad (2)$$

where ω_j^{02}, ω_j^2 are the lattice frequencies as reckoned in the usual harmonic theory and the new harmonic approximation respectively. Here any temperature dependence of f at constant volume will be neglected, since near 0°K and for such large zero energy the approximate

* At the time of writing.

formula (I, eqn. (27)) for ω_j^2—written out in terms of (I, eqn. (21))—is sufficient:

$$\left.\begin{aligned}\omega_j^2&=\omega_j^{02}+\sum_{kk'}\frac{e_{kj}\,e_{k'j}}{m}\sum_{k''k'''}U_{kk'k''k'''}\,A_{k''k'''},\\ \omega_j^{02}&=\sum_{kk'}\frac{e_{kj}\,e_{k'j}}{m}\,U_{kk'},\\ A_{kk'}&=\frac{\hbar}{4}\sum_j\frac{e_{kj}\,e_{k'j}}{m}\,\omega_j^{-1}.\end{aligned}\right\}\quad\ldots\quad(3)$$

As a first approximation to f we shall use the corresponding function $f(r)$ reckoned from (2) and (3) for a linear chain of helium atoms. It can be shown* that in a linear chain (with next-neighbour interactions) f_j is constant for all j, the solutions of (3) being of the type

$$\left.\begin{aligned}\omega_j^2&=\frac{4}{m}\psi(r)\sin^2\frac{\pi_j}{N},\\ \omega_j^{02}&=\frac{4}{m}\frac{\partial^2\phi(r)}{\partial r^2}\sin^2\frac{\pi_j}{N};\end{aligned}\right\}\quad\ldots\ldots\ldots\quad(4)$$

here N is the number of atoms (cyclic boundary conditions) and $\psi(r)$ a function of the second and fourth derivatives of ϕ. Thus,

$$f(r)=1-\frac{\partial^2\phi(r)/\partial r^2}{\psi(r)}\;;\quad\ldots\ldots\ldots\quad(5)$$

we may notice that for the linear chain $0<f(r)<1$ implies that the usual harmonic vibrations are stable, $f(r)>1$ that the corresponding harmonic theory fails.

Table 1. Auxiliary Functions from the Helium Linear Chain

r (cm$\times10^{-8}$)	$\psi(r)$ (erg/cm^2)	$\partial^2\phi(r)/\partial r^2$ (erg/cm^2)	$f(r)$
2·8	$8{\cdot}75\times10^2$	$3{\cdot}37\times10^2$	0·615
3·0	$3{\cdot}53\times10^2$	$9{\cdot}20\times10$	0·740
3·2	$1{\cdot}46\times10^2$	$1{\cdot}67\times10$	0·886
3·4	$5{\cdot}95\times10$	−4·88	1·08
3·6	$2{\cdot}19\times10$	−9·44	1·43
3·8	5·28	−8·92	2·69

The derivation of $\psi(r)$ is lengthy and only numerical values will be given here; they are calculated from a Lennard-Jones potential $\phi(r)$ chosen to fit the empirical curve of Yntema and Schneider as closely as possible over a range of r covering the minimum and inflexion points—the region of interest for lattice dynamics. This choice of ϕ will be discussed together with the lattice potential in the later paper; the relevant results, together with values of $f(r)$, are shown (rounded to three significant figures) in table 1.

* To be published.

It is found that $\psi(r)$ has just one well-determined positive value for all r less than 3·98 Å, at which point $\partial^4\phi/\partial r^4$ becomes negative and the new theory also breaks down. However, if we set $r \approx a$, the next-neighbour distance in the helium lattice, this limit corresponds to a molar volume $\sim$23 cm^3, which is beyond the melting volume at 0°K ($\sim$21·5 cm^3), the largest volume attainable; the function (5) then provides a reasonable approximation to the unknown f of the three-dimensional lattice, and in terms of it the theory is valid over the whole experimental range.

We may notice that the value of f gives an indication of the relative importance of the quadratic and quartic parts of the vibrational energy. For helium the new maximum lattice frequency would still be about 14% greater than the maximum frequency in the usual spectrum ω_j^0 (both estimated according to (4)) under a pressure $\gg$4000 atm at 0°K (molar volume $\sim$4 cm^3); Dugdale and Simon quote Bridgman's contention that all substances reduce to normal behaviour at high pressure, implying that this state is approached for helium at the pressures studied ($<$3000 atm)—in fact, normal dynamical behaviour lies well beyond the present available range of experimental conditions. In the other direction, no substance could be relatively so far expanded by reduced pressure as is helium near 0°K unless the quartic part of its vibrational energy were able to provide a stabilizing influence on the lattice vibrations; this depends in the first place on the shape of the interatomic potential ϕ, and of course on the structure and degree of interaction of the lattice.

Table 2. The Function f_V for Solid Helium

V (cm^3)	a (cm$\times 10^{-8}$)	f_V	V (cm^3)	a (cm$\times 10^{-8}$)	f_V
10	2·862	0·750	17	3·416	1·360
11	2·955	0·811	18	3·482	1·545
12	3·042	0·878	19	3·545	1·788
13	3·124	0·950	20	3·606	2·195
14	3·202	1·030	21	3·665	3·22
15	3·276	1·119	22	3·723	$\sim$8
16	3·348	1·227			

To make $f(r)$ give as far as possible the properties to be expected of f_V we define the spacing r in the linear model not as the next-neighbour distance of the helium lattice exactly, but by the relation

$$r = a + \delta.$$

δ is chosen so that the critical value $f(r)=1$, corresponding to $\partial^2\phi/\partial r^2 = 0$, goes over into $f_V = 1$ when V is determined by $\partial^2 U_0/\partial V^2 = 0$; as discussed in II, the latter condition characterizes the failure of the three-dimensional lattice dynamics. Thus,

$$f_V \equiv f(a+\delta), \qquad \ldots\ldots\ldots \quad (6)$$

V and a being related by (1); δ is the difference between the inflexion distances r_i of $\phi(r)$ and a_i of U_0 and from the lattice calculations quoted above we find $\delta=0{\cdot}153$ Å. The function (6) is given in table 2; it increases rapidly near the upper volume limit and can there be no more than a rough approximation.

§ 3

With f_V as in table 2, the thermodynamical formulae (II, eqns. (5), (6)) for the specific heat at constant volume and the energy, viz.

$$\left.\begin{aligned}\mathscr{C}&=(1+\tfrac{3}{4}f_V)C^D(x)-\tfrac{3}{4}f_V C^E(x),\\ \mathscr{E}&=U_0+(1-\tfrac{1}{4}f_V)E^D(x)+\tfrac{1}{4}f_V TC^D(x),\end{aligned}\right\} \quad . \quad . \quad . \quad . \quad (7)$$

Fig. 1

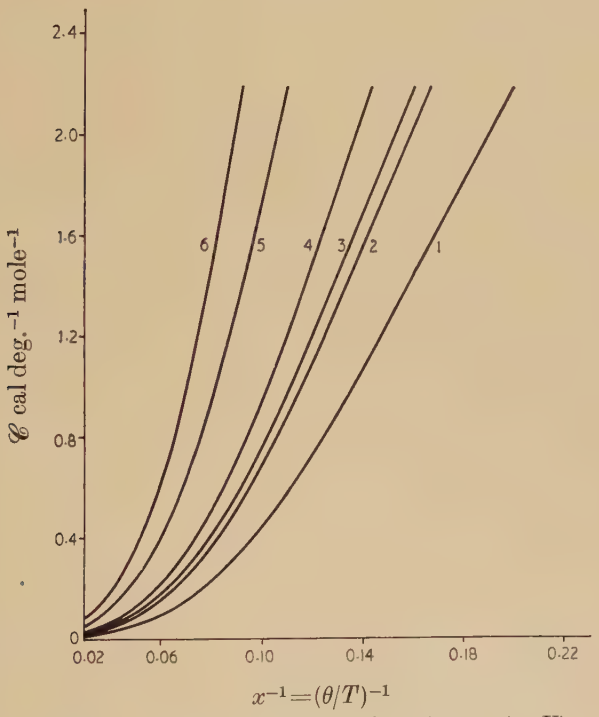

The reduced specific heat functions $\mathscr{C}(x, V)$.
1 : $f=0$ (Debye); 2 : $V=10{\cdot}61$ cm^3, $f=0{\cdot}788$; 3 : $V=13{\cdot}6$ cm^3, $f=1$;
4 : $V=18{\cdot}30$ cm^3, $f=1{\cdot}61$; 5 : $V=21{\cdot}08$ cm^3, $f=4{\cdot}05$; 6 : $V\approx21{\cdot}5$ cm^3, $f=7$.

may be evaluated in terms of the reduced variable $x=\theta/T$. C^D and C^E are the well-known Debye and Einstein specific heat functions (per mole); the parameter θ, a function of the volume (see II), will be determined below. For comparison with the work of Dugdale and Simon (1953) we consider first the specific heat $\mathscr{C}$. The function (7) has been calculated for seven molar volumes at which these authors have made specific heat measurements and for two volumes at a lower density considered by Keesom and Keesom (1936). Some of the resulting curves are shown in fig. 1; the explicit volume dependence, arising from the factors f_V, is

clear. Debye's function $C^D(x)$ is drawn for comparison; it would correspond to a volume at which $f_V=0$—which implies that the old and new frequencies are approximately identical—but the preceding discussion shows that this volume lies far outside the experimental range. The curves for $f_V=1, 7$ have also been included in the figure; the one corresponds to the point $\partial^2 U_0/\partial V^2=0$, marking the limit of validity of the usual quadratic theory, and the other, together with the Debye curve $f=0$, encloses the full range of functions which could be possible for solid helium ($f\approx 7$ for the melting volume at 0°K, approximately 21·5 cm³). The spread of these curves gives an indication of the degree to which extreme inaccuracy in the value of f might influence the reduced specific heat function at any particular volume.

Dugdale and Simon have found that their experimental specific heat curves $\mathscr{C}_V(T)$ can be superimposed with considerable accuracy by the choice of reduced variables* $x=\phi/T$, $\phi=\phi(V)$. At first sight the resulting single reduced curve $\mathscr{C}(x)$, say, stands in contrast to our various theoretical reduced functions (7), say $\mathscr{C}(x, V)$. But within the range of variables attainable in the solid state we can make a similar empirical superposition of the theoretical $\mathscr{C}(x, V)$ curves themselves, and to the same degree of accuracy. That this is not an exact theoretical property is clear, since otherwise all the functions $\mathscr{C}(x, V)$ would have to be reducible to the Debye function by a change of scale in x. For if the superposition were made by multiplying x by a function $\rho(V)$, to give a new reduced variable $x=\rho\theta/T$ at each volume, we could choose the arbitrary multiplying factor in ρ so that $\rho=1, f=0$ together. But it is not to be expected that such an exact reduction is compatible with (7).

On the other hand, the differences in shape between the various $\mathscr{C}(x, V)$ curves are not very great and it requires a wide range of x and V (or f) for them to be significant. This is seen clearly in fig. 2 where the $\mathscr{C}(x, V)$ curves have been superimposed (by a suitable choice of the function $\rho(V)$) for the possible values of x between the limits given by the lowest practicable temperature and the melting temperature at each volume. Even when f ranges from 0·8 ($\sim$10 cm³/mole) to 4 ($\sim$21 cm³/mole, experiments of Keesom and Keesom (1936)), a very accurate superposition is evidently possible in the restricted range of x. The dotted lines represent the extreme cases $f=0$ (a Debye curve) and $f=7$ ($V\sim$the melting volume at 0°K); for the first a difference is everywhere apparent, but we have seen that $f=0$ lies well outside the experimental range; the second is used to illustrate the obvious failure of the superposition once the curves were extended far beyond the available values of x (which in this case are limited practically to the left-hand origin).

The arbitrary factor in $\rho(V)$ has been chosen so as to fit the curves as closely as possible to the empirical $\mathscr{C}(x)$ of Dugdale and Simon, shown as a full line in the figure. The agreement is very close, except in the

---

* We use the reciprocal of Dugdale and Simon's ϕ for convenience.

region of large values of $\mathscr{C}$ (where only the small molar volumes appear); here—see also below—the Debye approximation of II does not suffice.

Fig. 2

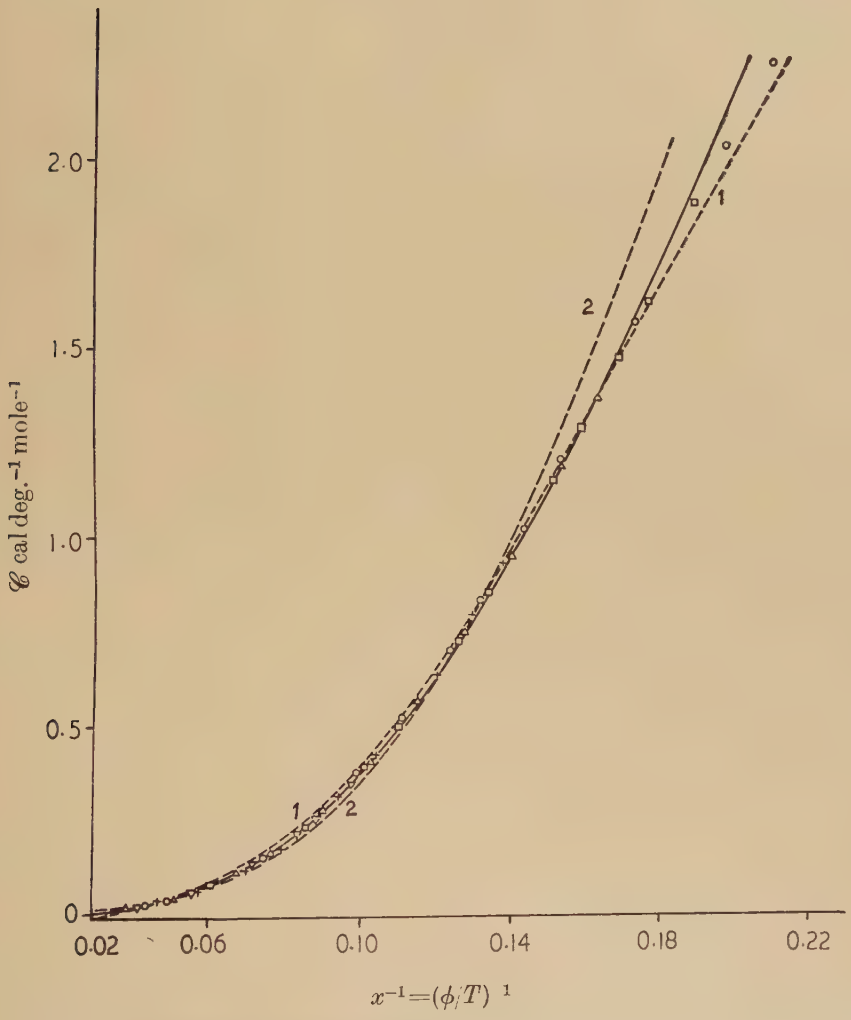

Approximate theoretical superposition of the reduced specific heat functions.
1 : $f=0$ (Debye) ; 2 : $f=7$; ○ : $V=10{\cdot}61$ cm^3, $f=0{\cdot}788$;
□ : $V=11{\cdot}67$ cm^3, $f=0{\cdot}858$; △ : $V=13{\cdot}03$ cm^3, $f=0{\cdot}951$;
▽ : $V=14{\cdot}44$ cm^3, $f=1{\cdot}068$; + : $V=18{\cdot}30$ cm^3, $f=1{\cdot}610$.

Over most of the experimental range the foregoing discussion provides a theoretical explanation for the observed reduced specific heat curve of Dugdale and Simon, as an approximate description of the anharmonic thermal properties. However, it might also be inferred that the observations at higher densities (and temperatures) would no longer be empirically reducible to one curve, since the theoretical superposition

there becomes progressively worse within itself, the range of x becoming too wide.

§ 4

The specific heat as a function of temperature, $\mathscr{C}_V(T)$, can be read off from the various $\mathscr{C}(x, V)$ once the parameter θ is known. The theoretical determination of θ in the anharmonic theory, and in particular for solid helium, has been discussed in II. However, we must here fall back on the empirical practice of fitting the specific heat formula, now (7), to the experimental measurements in order to fix an empirical average parameter θ at each volume since we have no knowledge of the new lattice spectrum in solid helium by which to carry out the theoretical determination. Nor has the differential equation (II, eqn. (13)) any ready means of solution for solid helium; we cannot estimate θ (or its volume derivatives) on the right-hand side from empirical elastic constants or expansion coefficients since these do not refer to the new harmonic approximation with respect to which θ is defined (see, for example, the definition of Grüneisen's coefficient γ in § 5). The empirical θ found here by fitting (7) is of course not the same as the empirical Debye parameter, called θ' in II, given by Dugdale and Simon, which has no real place in the theory; nevertheless, the empirical temperature dependence at constant volume is much the same in the two cases and the correction in absolute value given by the anharmonic theory relatively small (see table 3 below).

Table 3. Fitted ' Debye ' Parameters as Functions of Volume

V (cm^3)	θ (°K)	θ' (°K)	ϕ (°K)	$\rho(V)$
10·61	137·36 (132·5)	118·0 (110·0)	111·0	0·81
11·67	112·99 (110·1)	94·6 (91·5)	90·6	0·80
13·03	86·90 (86·5)	72·1 (71·0)	68·0	0·78
14·44	67·84 (67·5)	55·5 (54·5)	52·0	0·77
18·30	44·10 (41·5)	33·8 (31·5)	30·2	0·69

This temperature dependence is shown in fig. 3. Clearly, a one-parameter Debye theory gives a good approximation to the specific heat in the middle range of helium temperatures only. At the lowest temperatures, at any rate for the low densities studied by the Keesoms, the use

of an average θ is very crude—as already remarked by Webb *et al.* (1952) and again by Dugdale and Simon, in regard to θ'. No results are available at the higher densities and such low temperatures, but there are indications in fig. 3 that this failure is general and for the higher densities extends to higher temperatures. Again at higher densities the approximation is bad near the melting point (the melting curve is shown as a dotted line in fig. 3). The existence of a constant limiting empirical θ at high enough temperatures, inferred by analogy with many ordinary substances, is not substantiated for helium (cf. Domb 1952, and the discussion of II). It appears instead that there is a region of almost constant θ in the central part of the range at each volume, provided the melting temperature is high enough for it to be reached, and here the new Debye approximation may be expected to give good results. It would be of interest to have experimental values at still higher densities to see whether this feature remains.

Fig. 3

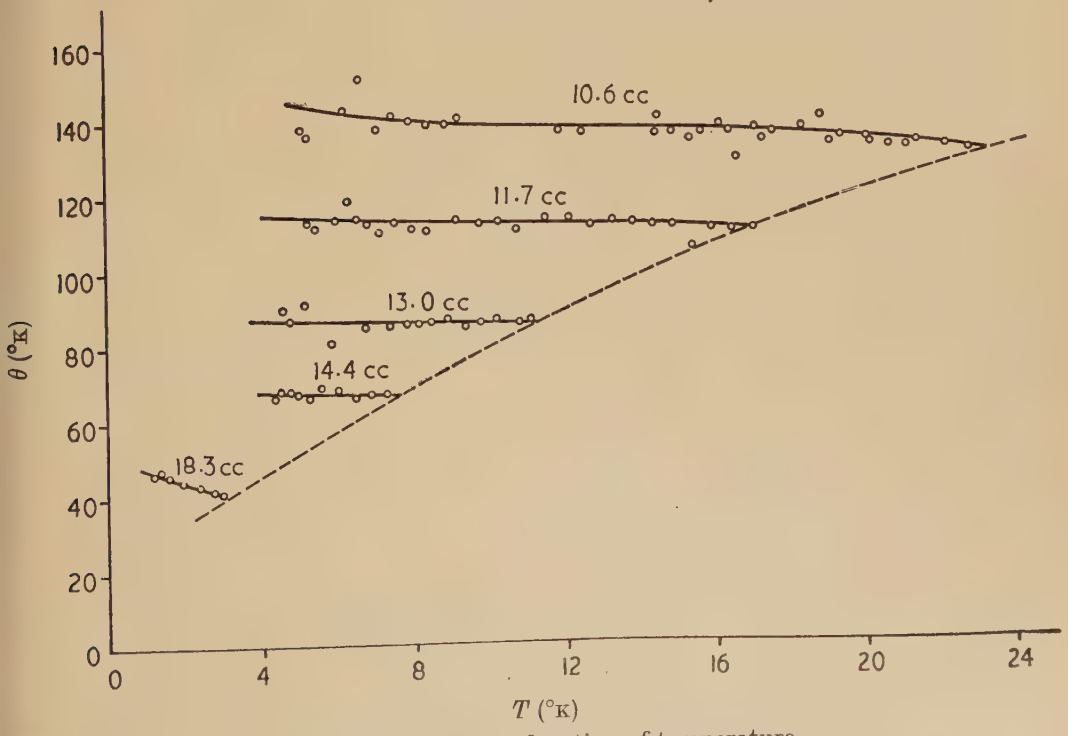

Fitted Debye θ as a function of temperature.

The average values of θ from fig. 3 are shown in table 3 (the figures in brackets are the values on the melting curve). The corresponding values of θ' due to Dugdale and Simon are given for comparison. These authors have evidently defined their empirical specific heat curve $\mathscr{C}(x)$, $x=\phi/T$ by choosing for the parameter ϕ values near those of θ' on melting; this empirical ϕ, which is not the result of fitting a Debye specific heat

formula, could equally be made to agree with θ, and most sensibly to agree with the constant value of θ in the central part of the temperature range. However, Dugdale and Simon's values of ϕ are shown in the table for reference, together with the function $\rho(V)$ as used in § 3.,

Fig. 4

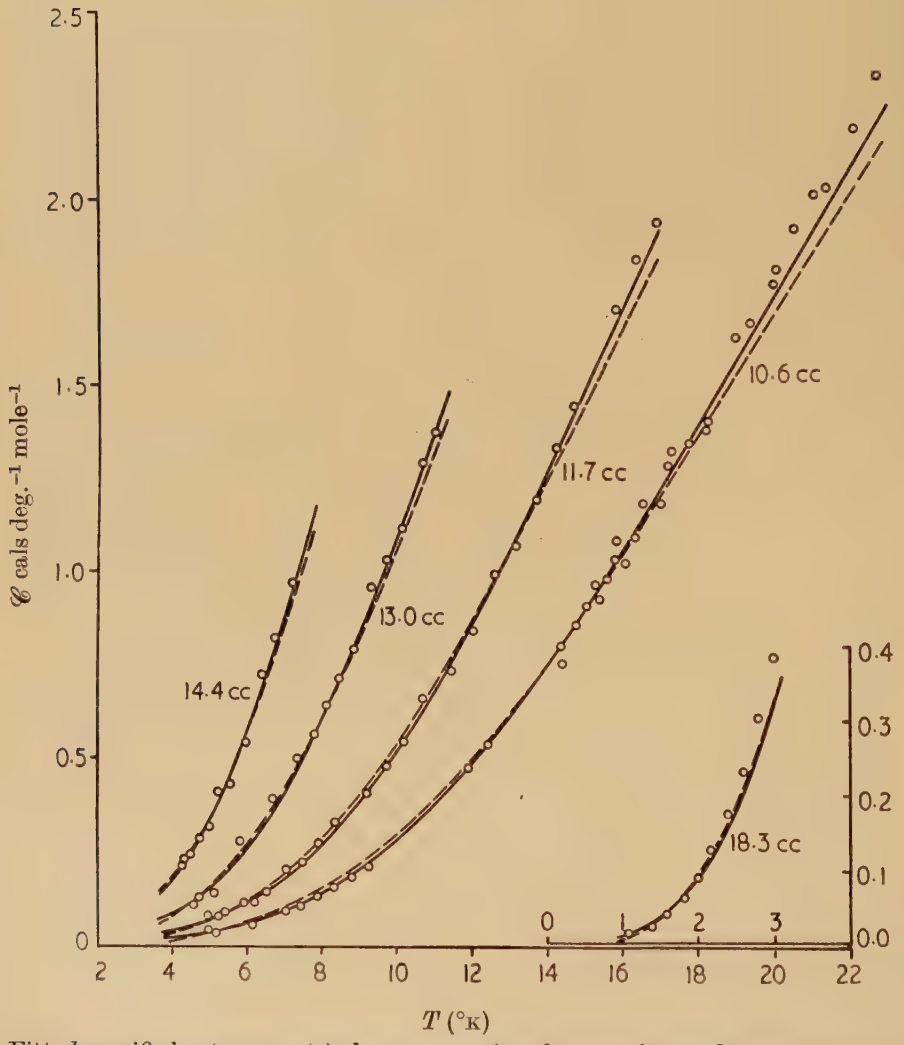

Fitted specific heat curves (circles representing the experimental measurements).

We may notice that although the fitted θ's depend directly on the exact determination of the function f_V the fitted specific heat curves $\mathscr{C}_V(T)$ which follow from them are insensitive to changes in f. Thus the approximate determination of f does not affect the practical specific heat results very greatly; it is of importance only where the absolute values of θ are concerned, and by contrast only the large relative changes in θ are of real interest in this case.

The curves $\mathscr{C}_V(T)$, got from (7) with the help of θ as in table 3, are shown in fig. 4; the circles denote the experimental points. A good fit is obtained between theory and experiment except near melting at the higher densities or at very low temperatures, as noted previously; if values of θ nearer the limits at melting are chosen in these cases the overall fit of the $\mathscr{C}_V(T)$ curves is not so good. In the figure the dotted curves are derived from the Debye function $C^D(x)$ with the help of the fitted θ' of table 3; the agreement is worse at higher temperatures and smaller volumes. This is to be expected, since here the short lattice waves—essentially anharmonic in nature—are of more importance, and we have seen that their effects can not be described by simple Debye formulae alone. It should be remarked that although the specific heat at the lowest temperatures depends only on the long lattice waves, which *are* effectively those of a harmonic continuum, the energy, for example, does not—the zero energy always introduces an essential anharmonicity which can not be described by the simple Debye formulae corresponding to θ', and we should not use this θ' uncritically to give other vibrational properties.

§ 5

It is of interest to see the influence of the anharmonicity on some other thermodynamical properties considered by Dugdale and Simon. From (7) the zero-point energy is to be written

$$\mathscr{E}_0 = \tfrac{9}{8}R\theta(1-\tfrac{1}{4}f_V); \quad \ldots\ldots\ldots \quad (8)$$

approximated by the fitted θ of § 4, (8) is shown in fig. 5. As with the fitted specific heat functions $\mathscr{C}_V(T)$, the product $\theta(1-\frac{1}{4}f)$ tends to remain constant when f is varied at a given volume; thus the zero energy is also insensitive to the previous approximations. Dugdale and Simon's empirical expression $\frac{9}{8}R\theta'$, in which the average fitted θ' of table 3 is now used,* is shown by a dotted line in the figure; it lies within about 7% of the present estimate (8). By reference to the discussion given in II we see that there would be an approximate equality between these estimates of the zero energy (the second having a meaning only in an empirical sense), $\theta' \approx \theta(1-\frac{1}{4}f)$, provided the work of Domb and Salter quoted there were applicable to the values of the fitted θ and θ' we have used. It is possible that these constant values of θ, θ' (in the central part of the temperature range) play the rôle for helium of the constant limiting fitted Debye parameter in ordinary substances, but the present results do not give any real evidence one way or the other.

Following Dugdale and Simon, we can now make an estimate of the lattice potential U_0 based on the anharmonic theory by subtracting our

* Dugdale and Simon themselves use the values of the fitted θ' extrapolated to 0°K, but there is no special justification for this: by analogy with Domb and Salter's work they should have used values near melting. If we do use the figures in brackets from table 3 the modification in fig. 5 is very slight.

Fig. 5

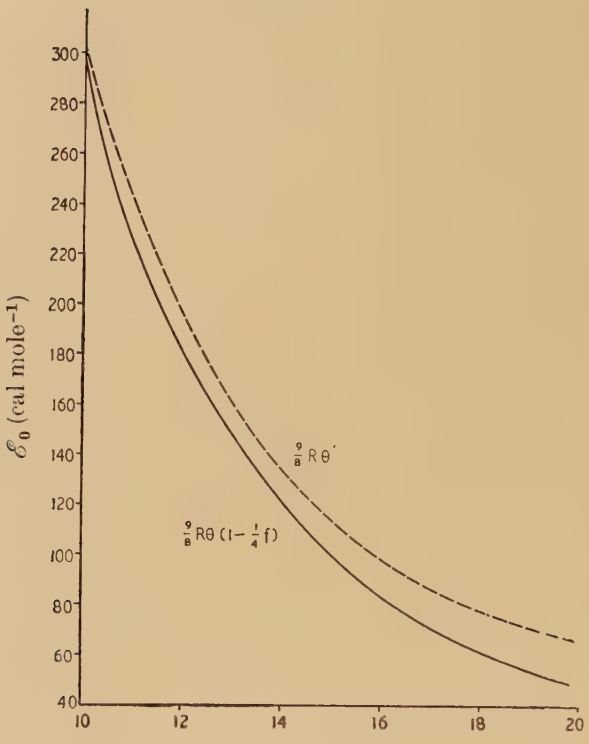

The zero-energy.

Fig. 6

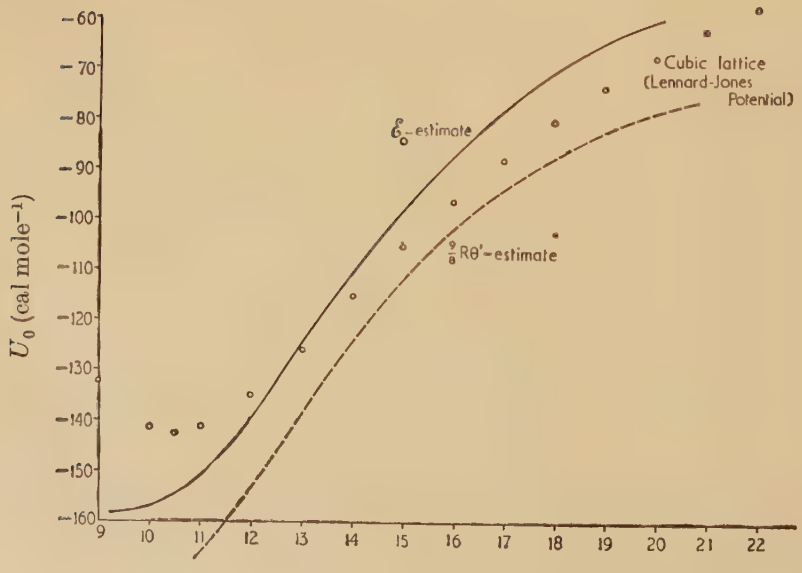

The lattice potential.

value of the zero-point energy from the internal energy at 0°K; the latter is of course properly to be calculated from the empirical Grüneisen equation of state $\mathscr{C}=\mathscr{C}(x)$, $x=\phi/T$, $\phi=\phi(V)$ quoted in § 2. Estimating this internal energy from Dugdale and Simon's graph, we get from (8) for U_0 the curve shown in fig. 6. The dotted line is got when the empirical zero-energy $\frac{9}{8}R\theta'$ (θ' as in table 3) is used; it is similar to Dugdale and Simon's estimate (the minimum of their curve appears to be much too shallow) and is shown here for comparison with the anharmonic result. The circles represent the lattice calculation quoted in § 1, made with the help of the Lennard-Jones potential used in determining the function $f(r)$. There is a general measure of agreement between this calculated lattice energy and the estimate given by the dynamical theory, although the minimum of the latter is some 15% deeper.

Table 4. Vibrational Amplitudes and the Lindemann Constant

T_m (°K)	V (cm^3)	Vibrational amplitude		Lindemann constant (g$^{1/2}$ deg.$^{1/2}$ cm)		
		from θ	from Domb	from θ	from θ'	from ϕ
20·8	11	0·168	—	127	108	102
17·7	11·5	—	0·201	—	—	—
15·1	12	0·178	—	124	105	99
13·1	12·5	—	0·212	—	—	—
11·2	13	0·192	—	122	102	96
8·7	14	0·198	0·228	120	99	93
6·8	15	0·208	—	118	96	90
5·4	16	0·218	0·251	117	94	87
4·3	17	0·224	—	121	96	88
3·3	18	0·226	0·277	131	102	92
	Average:	0·202	0·234	123	100	93

A further property which has been discussed for helium is the mean-square deviation of the atoms about their lattice sites along the melting curve (see Domb 1952). This can now be properly estimated with allowance for the anharmonicity since by Born's approximation (see I, eqn. (22)) the actual mean-square deviation, say $\langle(x_k-x_k^0)^2\rangle$, is the same as the mean-square deviation $\overline{(x_k-x_k^0)^2}$ reckoned over the new independent harmonic oscillations of frequencies ω_j. Thus Domb's formula (*loc. cit.*) can be used provided the empirical θ' is replaced by the new parameter θ, corresponding to the use of a theoretically valid harmonic approximation; for helium, of course, an expansion in powers of T/θ is required. The ratio $\langle(x_k-x_k^0)^2\rangle^{1/2}/a$ (a defined as in (1)) is given in table 4; the anharmonic correction reduces Domb's results by about 15%, but still gives twice the value found in a normal substance and preserves the relatively strong volume dependence; Domb's figures

are given for comparison. Also shown in the table are some values of the constant in the Lindemann melting formula

$$\theta = \text{const.}\ \sqrt{(T_m/MV^{2/3})}\,; \qquad \ldots\ldots\ (9)$$

it *is* a constant to a fair approximation, and in the present theory has a value rather nearer those of the other inert gases than was found by Domb who worked (incorrectly) from the empirical parameter θ'. As Dugdale and Simon point out, this validity of Lindemann's formula is remarkable, since the original derivation is no longer true: in particular we see that the ratio $\langle(x_k-x_k^0)^2\rangle^{1/2}/a$ is not constant, which is the assumption behind the constant in (9), nor can it be replaced by the expression $\frac{9}{2}RT/M(k\theta/\hbar)^2$ (cf. Domb, *loc. cit.*) which is appropriate for *large* values of T/θ.

Naturally, any theory of these vibrational considerations must depend on a properly valid parameter θ, and in the present theory the thermodynamical calculations of Dugdale and Simon—based on the single reduced specific heat function $\mathscr{C}(x)$, with parameter ϕ—represent an empirical description of limited validity which is *not* an approximation to an exact theoretical property. Whether the existence of a Lindemann formula is an exact theoretical property (written then in terms of the true parameter θ) has not been shown. The derivation of Simon's melting formula due to L. Salter, quoted by Dugdale and Simon, also has only the character of an empirical description since it depends on the existence of both $\mathscr{C}(\phi/T)$ and a Lindemann constant (in this case presumably to be reckoned from the same ϕ). Grüneisen's relation,

$$\gamma = \frac{\alpha V}{\kappa \mathscr{C}}, \quad \gamma = -\frac{d\log\phi}{d\log V},$$

otherwise proved only in the harmonic theory, is also here an empirical one. Of course, the difference between θ and ϕ is in practice not very great ($\rho\theta=\phi$, with ρ a function of volume whose average may be put equal to 1), but it is as well to keep in mind the exact significance and validity of the different Debye-type parameters which occur.

Acknowledgments

I wish to thank Professor Max Born for his continued interest in this work, and to acknowledge the receipt of a Carnegie Research Award during the greater part of the research.

References

Born, M., 1951, *Fest. d. Akad. Wiss. Göttingen* (Math.-Phys. Kl.), **1**.
Domb, C., 1952, *Comptes Rendus 2e Réunion Chimie Physique*. Paris.
Dugdale, J. S., and Simon, F. E., 1953, *Proc. Roy. Soc.* A, **218**, 291.
Hooton, D. J., 1955 a, *Phil. Mag.*, **46**, 422; 1955 b, *Ibid.*, 433.
Keesom, W. H., and A. P., 1936, *Physica*, **3**, 105.
Webb, F. J., Wilkinson, K. R., and Wilks, J., 1952, *Proc. Roy. Soc.* A, **214**, 546.
Yntema, J. L., and Schneider, W. G., 1950, *J. Chem. Phys.*, **18**, 646.

LIX. *The Magnetic Moments of Cobalt–Copper Alloys*

By J. Crangle
Physics Department, The University, Sheffield*

[Received December 29, 1954]

Abstract

The rate of change of atomic moment with electron concentration for the high-temperature face-centred cubic form of the solid solution of copper in cobalt has been derived from measurements on the variation of spontaneous magnetization of suitable alloys with temperature. It is quite close to the rate previously observed for solutions of copper in nickel, and the moment extrapolates to a value at the electron concentration of pure nickel which is near that previously measured directly. The Law of Corresponding States does not hold for this system, and the fullness of the reduced magnetization temperature curves increases with the copper concentration, in contrast with the decrease in fullness often observed previously in similar measurements on other alloy systems.

§ 1. Introduction

The results of measurements on the saturation magnetic moments of the ferromagnetic elements and of their solid solution alloys with other elements and with each other are generally thought to give data which are among the most useful in the theory of the metallic properties of these elements. The data on the effect of composition on magnetic moment in alloys of nickel with other elements are fairly comprehensive, being mainly due to Alder (1916), Sadron (1932), and Marian (1937). In the particular case of the nickel–copper system, the variation of magnetic moment with composition has been very simply explained on a collective electron basis. The Fermi limit in the common 3d band is assumed to rise progressively as copper is added to nickel until at about 60% of copper the band is filled and the magnetic moment disappears. In alloys of nickel with other elements, the rate of extinction of the moment has been in several cases correlated with the valency of the added element, suggesting that the vacant parts of the 3d band in nickel were being filled by transfer of electrons from atoms of the solute elements.

The position with regard to data on the effect of added elements on the magnetic moments of iron and of cobalt is much less satisfactory than that for the nickel alloys. Very few suitable elements dissolve in iron to any marked extent, and for cobalt certain difficulties have hitherto

* Communicated by Professor W. Sucksmith, F.R.S.

prevented sufficiently reliable data from being obtained. The aim of the work, of which the present paper describes the first part, is to bridge the gap in the case of the cobalt alloys.

Previous measurements of the magnetic moments of cobalt–copper alloys have been made by Meyer and Taglang (1950). They compared the dependence of the moment on copper content with that observed for a similar dilution with copper of an equiatomic iron–nickel alloy. It was expected from a simple collective electron treatment that cobalt and the nickel–iron alloy would show the same rate of change of moment with composition, but this was not found experimentally. Their work was on the hexagonal phase in cobalt.

There appear to have been no previous measurements on the magnetic moments of the face-centred cubic phase of the cobalt–copper system. In order to be able to make instructive comparisons between the properties of different alloy systems, it would appear that where possible alloys having the same crystal structure should be considered.

§ 2. Previous Work

It is well known that in pure cobalt a change of phase occurs near 400°C. The equilibrium crystal structure is face-centred cubic at temperatures above this change and a close-packed hexagonal structure predominates below. At room temperature and at lower temperatures the magnetocrystalline anisotropy of the hexagonal phase is large, and very strong magnetic fields must be applied before it is possible to approach magnetic saturation in polycrystalline material. The only simple way in which the spontaneous magnetization $\sigma_{,T}$ (at any temperature T) and in particular the magnetization at the absolute zero $\sigma_{0,0}$ may be measured for hexagonal cobalt is by using single crystals with the magnetic field applied along the easy direction of magnetization. Since the cubic phase does not normally exist alone at a temperature sufficiently low to allow a direct measurement of its magnetic moment, an extrapolation procedure has to be devised to enable measurements made above the temperature of the phase change to be used. Myers and Sucksmith (1951) used a method based on the similarity in shape of the graphs of spontaneous magnetization against temperature which they found for cubic cobalt and for nickel.

They deduced that the moment of cubic cobalt at the absolute zero is about 3% greater than that for the hexagonal form. Also, each phase appeared to possess a different kind of dependence of spontaneous magnetization on temperature.

The previous measurements of the magnetic moments of cobalt–copper alloys made by Meyer and Taglang (1950) were made on polycrystalline alloys that were predominantly hexagonal-phase, in the region of extreme magnetic hardness. In spite of the difficulties of extrapolating first to saturation conditions, and then to the absolute zero, it is unlikely that the errors could have been sufficient to account for the differences they

observed between the dilution properties of these alloys and those formed on the nickel–iron base.

Hashimoto (1937) found that the equilibrium solubility of copper in hexagonal cobalt at room temperature is 9·4% (by weight), with a slight increase in solubility in the cubic phase and at higher temperatures. The addition of copper causes the equilibrium temperature of the hexagonal-to-cubic phase change to fall from above 400°c in pure cobalt to about 340°c at the solubility limit. The change is sluggish, and on cooling from high temperatures the cubic phase can be retained in a non-equilibrium state for a significant range of temperature below the equilibrium phase-change temperature.

The present observations have all been carried out on the high-temperature cubic phase of the system. Attempts to obtain very reliable data on the hexagonal phase at the same time have failed because of the difficulty of preparing suitable single crystals of this phase in alloys containing useful amounts of the solute ; and also because of the tendency for some of the cubic phase to be retained on cooling to the hexagonal region.

§ 3. Materials Used

The alloys were made by melting together appropriate amounts of cobalt and copper in an induction furnace under an atmosphere of argon at a pressure of about 10 cm of mercury. To reduce the chance of inhomogeneity within the alloys, all members of the alloy series were heated *in vacuo* at about 1200°c for three days.

The cobalt used was of high purity and had been presented by the Société Générale Métallurgique de Hoboken, Antwerp, Belgium. The copper was spectrographically pure material obtained from Johnson Matthey and Co., Ltd.

The alloys were analysed chemically for the amount of the solute element, and also spectrographically for the presence of impurities.* The analyses are shown in table 1.

Table 1. Analyses

Alloy	D3	D5	D1	D6	D7
% Cu (weight)	3·69	5·66	7·89	9·76	11·68
% Cu (atomic)	3·43	5·26	7·34	9·10	10·91

Impurities : Fe and Ni were the only elements detected, and these were both present in amounts of less than 0·01%.

Metallographic evidence was obtained, with the kind assistance of Dr. D. W. Wakeman, of the Department of Metallurgy, University of Sheffield, that the 10·91% alloy in the homogenized state contained a small amount of some second phase, situated at its grain boundaries. This was absent in the alloys of lower composition, but a 25% alloy similarly treated showed the presence of a copper-rich phase at the grain

* The analysis was performed by the Sheffield Smelting Co., Ltd.

boundaries in easily recognizable quantities. This tends to support the magnetic evidence, mentioned later, that the first four of these alloys were homogeneous solid solutions.

§ 4. Experimental Methods

Magnetization measurements were made using a ring balance (Sucksmith 1939). They were standardized against a specimen of 99·96% pure iron supplied by the British Iron and Steel Research Association. Its specific magnetization was assumed to be 217·7 c.g.s. units at 17°c in an applied field of 17 000 oersteds (Weiss and Forrer 1929). Values in lower fields for this specimen were measured relative to this value by Dr. J. E. Thompson, using the method described by Sucksmith and Thompson (1954).

Temperatures from room temperature upwards to well above 1100°c were obtainable by means of a small vacuum furnace similar to the one described by Sucksmith and Pearce (1938). A platinum/13% platinum–rhodium alloy thermocouple placed with its hot junction in close contact with the specimen was used to measure temperature.

The specimens were in the form of rough ellipsoids, 4 mm long by 1·8 mm diameter. All were assumed to have a constant demagnetizing coefficient $N\rho$ of 17·5. Any slight error in this arising from the variation of the density of the alloys with composition would have a negligible effect on the interpretation of the magnetic measurements.

To obtain the cubic phases over the widest temperature range, measurements in the region of the phase change were made while cooling the specimens from higher temperatures. Because of the danger of solute loss by preferential evaporation at the highest temperatures, however, it was desirable that the specimens should only be heated into this range after all the measurements required at lower temperatures had been completed. The usual sequence was therefore to measure magnetizations from about 600°c downwards to the temperature of the phase change, and then from 600°c upwards to the Curie point.

The spontaneous magnetization of a ferromagnetic is the value of its intrinsic, or domain, magnetization in zero applied field. Because of complications associated with the domain structure, it is not possible to measure this quantity directly. It must be obtained by suitable extrapolation of measurements of the intrinsic magnetization obtained in strong fields.

In the present alloys, all of which had Curie points of higher than 1000°c, there was no detectable variation of intrinsic magnetization ($\sigma_{H,\,T}$) with field (H) in the cubic phase below 800°c. It was thus adequate to take the spontaneous magnetization ($\sigma_{0,\,T}$) below 800°c as being the same as the high-field magnetization ($\sigma_{H,\,T}$). At slightly higher temperatures, where $\sigma_{H,\,T}$ increased slowly with increasing field, $\sigma_{0,\,T}$ could be obtained simply by linear extrapolation to zero internal field. For temperatures approaching that of the Curie point, however, this was not possible because of curvature of the ($\sigma_{H\ T}$, H) isothermals.

For this region, the extrapolation technique devised by Weiss and Forrer (1926) was adopted.

In this procedure, graphs of internal field (H_i) against temperature (T) for chosen constant magnetizations may be drawn by interpolation

Fig. 1

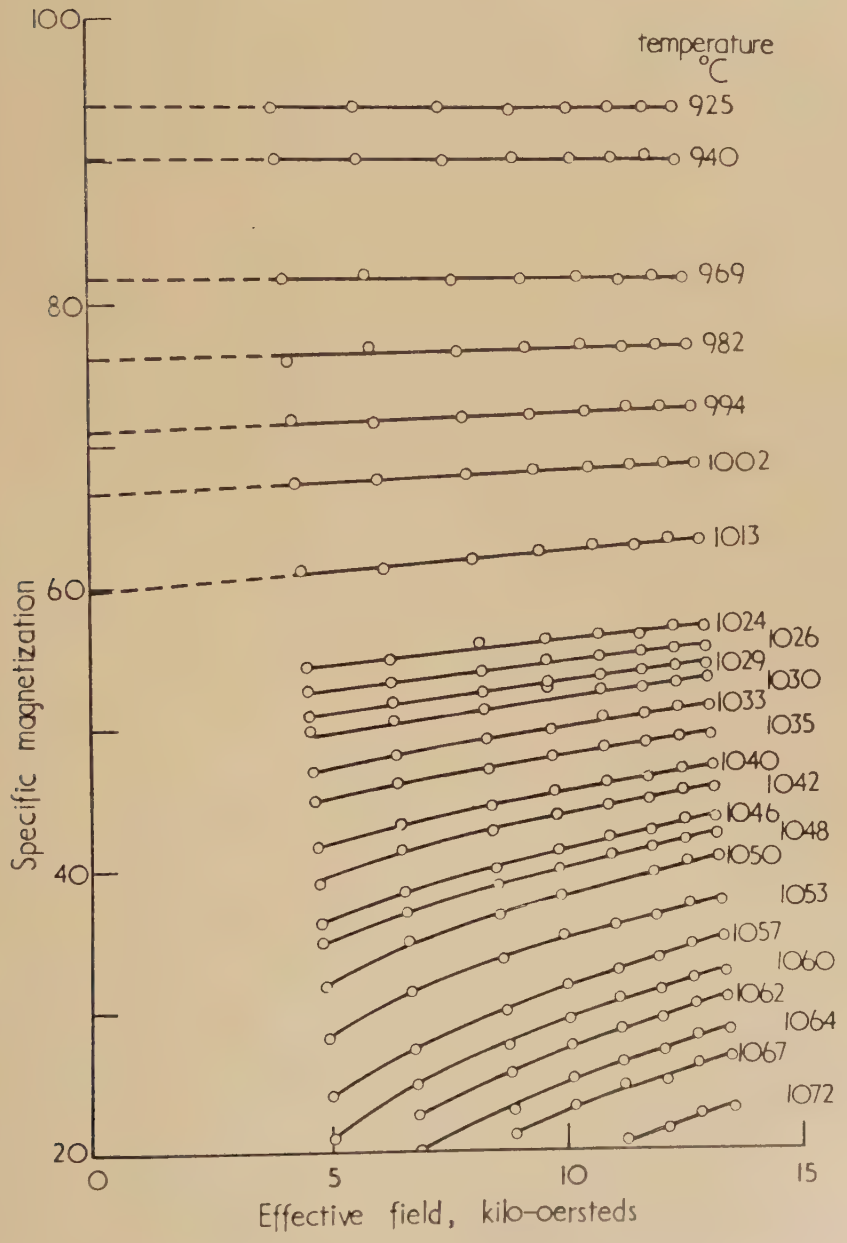

($\sigma_{H,T}$, H_i) isothermals for alloy containing 7·34 atomic % of copper.

of values from the $(\sigma_{H,T}, H_i)$ isothermals. The curves of constant magnetization so obtained are straight lines for the higher values of H_i and become convex towards the temperature axis in low fields. The straight lines can easily be extrapolated to $H_i=0$ to give the temperature at which the spontaneous magnetization has the particular value chosen.

By constructing a family of these curves of constant magnetization, values of the spontaneous magnetization at temperatures close to the Curie point may be obtained. Weiss and Forrer (1926) and Oliver and Sucksmith (1953) showed that the values of spontaneous magnetization so obtained are identical with those obtained from measurements of the magnetocaloric effect, except in the region of the tail on the $(\sigma_{0,T}, T)$ graph near the Curie point. Detailed examination of these two sets of

Fig. 2

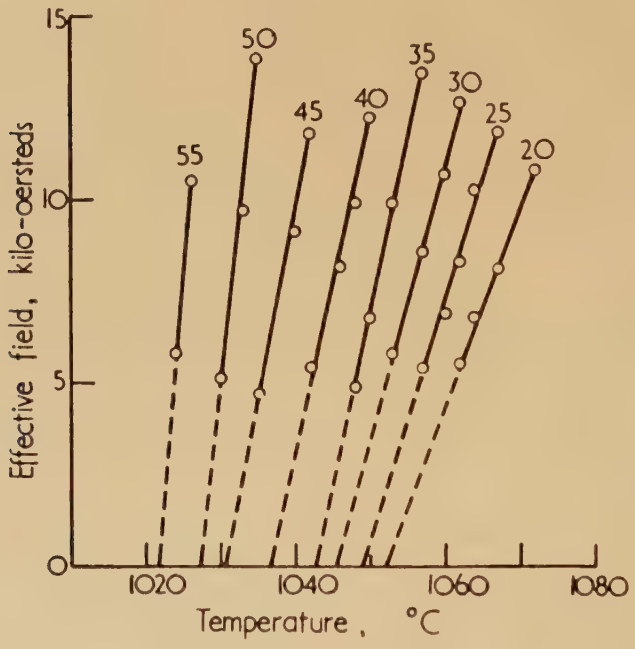

Curves of constant magnetization for the 7·34% alloy.

measurements has shown that what deviation does occur arises from the use of $(\sigma_{H,T}, H_i)$ isothermals corresponding to temperatures above the Curie point, where paramagnetic behaviour is becoming apparent. In the present work, it was possible to obtain all the data necessary to enable the Curie points to be estimated without using temperatures so high as to cause such errors to arise.

Part of the set of $(\sigma_{H,T}, H_i)$ isothermals of the 7·34% cobalt–copper alloy is shown in fig. 1, and the corresponding curves of constant magnetization for the same alloy are shown in fig. 2.

§ 5. Results

Pure Cobalt

Myers and Sucksmith previously observed a marked dependence of the magnetization of polycrystalline cubic cobalt on previous heat treatment. With this in view, new measurements were carried out on a sample which had been taken from the batch of cobalt from which the present alloys were made, and remelted under exactly the same conditions as obtained during the alloy preparations. This material was not of the same batch as that used in the work cited. In this new polycrystalline material no dependence of magnetization on previous heat treatment was found, and the measurements agreed very well with those obtained by the earlier workers for single crystals that had been taken into the cubic phase region. Values of the spontaneous magnetization at different temperatures up to the Curie point are given in the first column of table 2. The Curie point, estimated by extrapolating the graph of the square of the spontaneous magnetization against temperature to the temperature axis, was 1117°C, in good agreement with the value of 1121°C found by Myers and Sucksmith.

To obtain a value for the spontaneous magnetization of cubic cobalt at the absolute zero of temperature ($\sigma_{0,\,0}$), the methods adopted by Myers and Sucksmith were followed. If the form is known for the variation of the reduced magnetization ($\sigma_{0,\,T}/\sigma_{0,\,0}$) with reduced temperature (T/θ), where θ is the absolute Curie temperature), then $\sigma_{0,\,0}$ may be obtained from measurements of $\sigma_{0,\,T}$. In the general case, the form of this variation is not known initially, for it has been shown for several materials that there is no strict adherence to the Law of Corresponding States. Before any calculation of $\sigma_{0,\,0}$ can be made, then, it is first necessary to find the form of the reduced magnetization-temperature relationship.

The method used by Myers and Sucksmith was to plot a secondary reduced magnetization-temperature characteristic, in which the magnetization was reduced against a value $\sigma_{0,\,\phi}$, where ϕ was the most convenient low temperature for which the magnetization was determinable directly. ϕ was made equal to $0{\cdot}5\,\theta$. Comparison with data for nickel reduced in the same way showed that both cubic cobalt and nickel possessed the same characteristic for values of T/θ between 0·5 and 1·0. It was inferred from this that the two characteristics were therefore identical over the full range of T/θ from 0 to 1.

The present measurements on pure cobalt were evaluated in the same way. Magnetizations reduced against $\sigma_{0,\,\phi}$ agreed to a degree similar to that found previously with the corresponding ones for nickel (taken from the work of Weiss and Forrer 1926). It was thus inferred that this cobalt obeys in its cubic phase the same reduced magnetization-temperature characteristic as nickel, and the reduced data for nickel were used to calculate a new value for the spontaneous magnetization of cubic cobalt

at the absolute zero. The value so obtained was $\sigma_{0,0}=166{\cdot}1$ e.g.s. units per gram, or $1{\cdot}75_1$ Bohr magnetons per atom.

Table 2. Spontaneous Magnetizations for pure Cobalt and the Alloys for the whole Temperature Range of the Face-centred Cubic Phase

Cobalt θ = 1117°c		3·43% Cu θ 1084°c		5·26% Cu θ = 1070°c		7·34% Cu θ = 1055°c		9·10% Cu θ = 1047°c		10·91% Cu θ = 1045°c	
Temp. °C	$\sigma_{0,T}$	Temp. °C	$\sigma_{0,T}$	Temp. °C	$\sigma_{0,T}$	Temp. °C	$\sigma_{0,T}$	Temp. °C	$\sigma_{0,T}$	Temp. °C	$\sigma_{0,T}$
412	155·2	272	154·0	254	150·7	232	147·8	233	143·7	141	143·3
433	154·4	289	153·5	264	150·3	254	147·2	250	143·2	152	143·1
472	152·7	296	153·6	283	150·4	292	146·1	294	142·5	160	143·0
532	149·4	317	152·8	325	149·0	300	146·0	328	141·3	182	142·4
594	146·0	333	152·2	354	147·9	354	144·1	348	140·8	207	142·1
626	144·0	354	151·5	384	146·9	405	142·1	390	139·6	227	141·7
663	141·0	376	150·5	441	144·6	448	140·5	463	136·8	251	141·2
698	138·1	433	148·0	500	141·7	479	139·0	521	134·0	275	140·6
773	130·7	457	147·0	546	139·2	553	134·8	571	131·1	306	139·6
832	124·0	493	145·3	588	136·9	600	132·0	613	128·4	339	138·6
889	115·4	508	144·7	616	134·9	640	129·2	622	128·0	421	135·6
941	106·5	527	143·6	633	133·5	687	126·0	637	127·2	496	132·3
971	100·0	550	142·2	655	132·2	732	121·9	686	123·5	549	129·7
993	94·9	572	140·6	680	130·2	781	117·0	730	119·7	615	126·0
1022	86·1	596	139·4	704	128·3	818	112·7	791	113·7	642	124·0
1046	77·6	612	138·4	755	123·6	850	108·3	834	108·5	672	121·9
1063	69·5	642	135·9	803	118·2	880	103·0	851	106·0	743	115·7
1076	63·9	681	133·1	842	112·4	909	97·3	872	102·8	806	109·1
1085	57·2	712	130·4	874	107·2	925	93·8	875	102·0	862	102·0
1089	55·0	765	124·9	903	101·7	940	90·1	912	95·5	890	96·4
1096	49·0	787	122·2	927	96·5	969	81·7	917	94·6	911	91·7
1099	45·0	834	116·1	932	94·7	982	76·2	924	92·7	937	95·1
1103	40·0	854	113·0	947	91·3	994	71·0	930	91·7	952	80·1
1106	35·0	886	107·9	956	87·9	1002	66·7	933	90·4	966	75·1
1108	32·0	909	103·6	971	84·2	1013	59·8	960	82·6	980	70·9
1111	25·0	928	99·7	984	80·1	1022	55·0	975	77·7	995	63·3
1115	20·0	945	95·6	994	76·7	1027	50·0	989	71·8	1001	59·9
		958	93·0	997	75·0	1030	45·0	990	71·1	1012	55·0
		974	88·8	1007	71·0	1037	40·0	1011	60·0	1016	50·0
		981	86·7	1016	67·0	1043	35·0	1018	55·0	1023	45·0
		999	80·9	1026	62·1	1046	30·0	1023	50·0	1027	40·0
		1013	75·7	1029	60·3	1049	25·0	1027	45·0	1029	35·0
		1025	70·5	1029	60·0	1052	20·0	1031	40·0	1033	30·0
		1037	64·8	1035	56·0			1034	35·0	1038	25·0
		1041	62·5	1038	53·0			1038	30·0	1040	20·0
		1051	60·0	1042	50·0			1041	25·0		
		1059	55·0	1052	44·0			1043	20·0		
		1066	50·0	1056	40·0						
		1070	45·0	1061	35·0						
		1074	40·0	1064	25·0						
		1078	35·0	1066	20·0						
		1081	30·0								
		1085	25·0								
		1089	20·0								

Cobalt–Copper Alloys

As in the case of pure cobalt, no dependence of the magnetization of the face-centred cubic phase of the five cobalt–copper alloys on previous heat treatment was observed, so long as the heat treatment was not carried out at such a high temperature that preferential evaporation of the copper caused the alloy composition to alter.

Magnetizations were measured at different applied fields and temperatures for each alloy, and the spontaneous magnetizations obtained from them are given in the various columns of table 2. In this table, the Curie points of the materials are given also. From them, and their variation with alloy composition, it is evident that in the 10·91% alloy the solubility limit had been exceeded.

To test the applicability of the Law of Corresponding States to the alloy system as a whole, the technique that had been previously applied to pure cobalt was used. For each alloy respectively, spontaneous magnetizations reduced against a value $\sigma_{0,\phi}$ measured at a temperature ϕ°K$(=\frac{1}{2}\theta)$ are given in table 3. It is apparent that there is no strict adherence to the Law of Corresponding States: the reduced magnetization at constant reduced temperature appears to rise with increasing copper concentration within the solid solution.

Table 3. Spontaneous Magnetizations of Pure Cobalt and the Alloys reduced against the respective Values of the Magnetization at a Temperature $\phi=\frac{1}{2}\theta$

$\frac{T}{\theta}$	Co	3·43% Cu	5·26% Cu	7·34% Cu	9·10% Cu	10·91% Cu*
1·0	0	0	0	0	0	0
0·95	0·496	0·501	0·500	0·521	0·542	0·521
0·9	0·636	0·636	0·640	0·662	0·680	0·667
0·85	0·724	0·729	0·738	0·751	0·761	0·760
0·8	0·792	0·798	0·810	0·814	0·821	0·810
0·75	0·845	0·851	0·859	0·859	0·866	0·864
0·7	0·888	0·894	0·897	0·897	0·903	0·901
0·65	0·925	0·928	0·930	0·929	0·933	0·933
0·6	0·954	0·957	0·957	0·957	0·961	0·958
0·55	0·978	0·981	0·981	0·980	0·983	0·981
0·5	1	1	1	1	1	1

* Beyond the solubility limit.

Because of the departure from the Law of Corresponding States, the method used to estimate the magnetization of pure cobalt at zero temperature could not be used for the alloys, and another technique had to be devised. This is most easily described by considering first the case of a system to which the Law of Corresponding States does apply, and where the variation of spontaneous magnetization with composition

at a low temperature has been observed to be linear. That is, when $T/\theta=0$, put $(\sigma_0)_c=(\sigma_0)_0-c(\partial\sigma/\partial c)_{T/\theta=0}$ where $(\partial\sigma/\partial c)_{T/\theta=0}$ is the rate of change of moment with composition at the absolute zero, and c is the composition of the alloy.

Let a graph now be constructed, showing the variation of moment with composition at constant values of reduced temperature (T/θ). These lines of constant (T/θ) will also be lines of constant $(\sigma_T)_c/(\sigma_0)_c$ for variable c, if the Law of Corresponding States applies ; i.e.

$$\frac{(\sigma_T)_0}{(\sigma_0)_0}=\frac{(\sigma_T)_c}{(\sigma_0)_c}$$

(where the subscript 0 outside the brackets signifies data for the pure solvent) i.e.

$$\frac{(\sigma_T)_c}{(\sigma_T)_0}=\frac{(\sigma_0)_c}{(\sigma_0)_0}=1-\frac{c}{(\sigma_0)_0}\cdot\left(\frac{\partial\sigma}{\partial c}\right)_0$$

or

$$(\sigma_T)_c=(\sigma_T)_0-c\left(\frac{\partial\sigma}{\partial c}\right)_{T/\theta},\quad \text{where}\quad \left(\frac{\partial\sigma}{\partial c}\right)_{T/\theta}=\frac{(\sigma_T)_0}{(\sigma_0)_0}\cdot\left(\frac{\partial\sigma}{\partial c}\right)_0.$$

Fig. 3

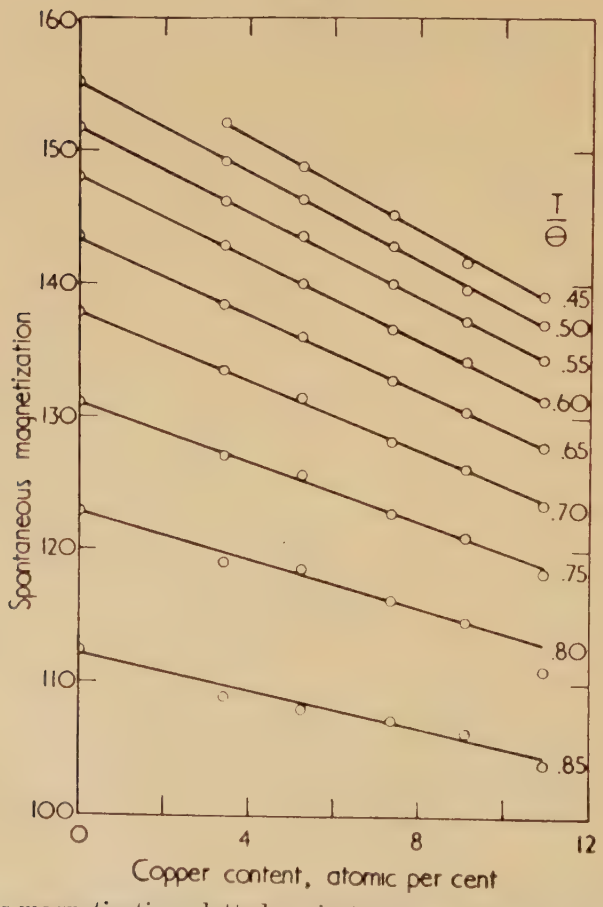

Spontaneous magnetization plotted against copper content for constant values of the reduced temperature.

Thus in cases where it is required to find $(\partial\sigma/\partial c)_c$ when direct measurements at sufficiently low temperatures cannot be made for the alloys, but where σ_0 is know for the pure solvent metal, it is possible to plot $(\partial\sigma/\partial c)_{T/\theta}$ as a function of the corresponding reduced magnetization of the pure metal $(\sigma_T)_0/(\sigma_0)_0$, and extrapolate to its value at zero temperature, where $(\sigma_T)_0/(\sigma_0)_0$ is unity. Knowledge of $(\sigma_0)_0$ for the solvent then leads directly to the dependence of $(\sigma_0)_c$ on alloy composition.

It was found that this method could be applied directly to the present alloy system, where there are in fact deviations from the Law of Corresponding States.

Graphs of the observed spontaneous magnetizations of the cobalt–copper alloys, plotted against composition for constant values of the reduced temperature and covering the whole available range of temperature and composition, are shown in fig. 3. These are straight lines, at temperatures not too close to the Curie point. The graph of their gradients $(\partial\sigma/\partial c)_{T/\theta}$ as a function of the reduced magnetizations of pure cobalt that correspond to the respective values of (T/θ) is shown in fig. 4.

Fig. 4

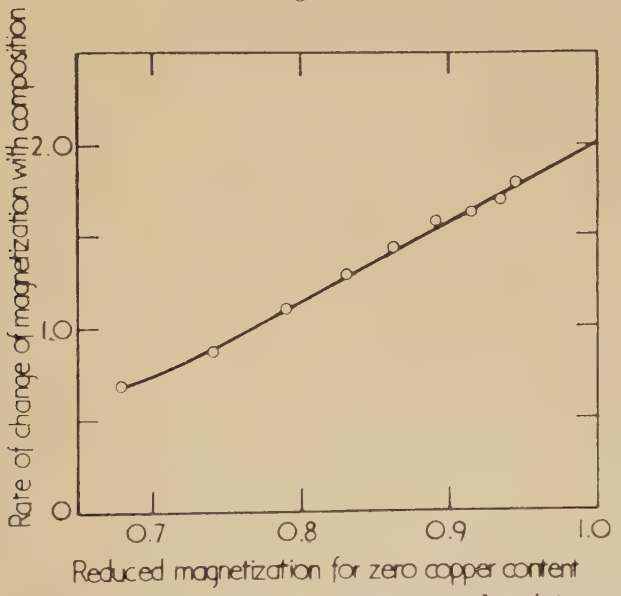

The rate of change of magnetization at constant reduced temperature with composition, plotted against the equivalent reduced magnetization for pure cobalt.

This graph is straight for values of $(\sigma_T)_0/(\sigma_0)_0$ greater than 0·75, and it extrapolates to a value for $(\partial\sigma/\partial c)_0$ of $2{\cdot}0\pm0{\cdot}1$ e.g.s. units per 1% change in composition at the point $(\sigma_T)_0/(\sigma_0)_0=1$.

It is noticeable that this line of fig. 4 is different from that which would occur if the Law of Corresponding States were to hold, for clearly $(\partial\sigma/\partial c)_{T/\theta}$ would then be zero when $(\sigma_T)_0/(\sigma_0)_0=0$, and the variation would be

linear for the whole of the increase up to the maximum value for $(\sigma_T)_0/(\sigma_0)_0$ of unity.

Using the value of $(\partial\sigma/\partial c)_0$ so obtained, and the known value of σ_0 for pure cobalt, the σ_0 values for all the alloys were estimated. Thus reduced magnetizations σ_T/σ_0 for each alloy were obtainable. They are plotted against reduced temperature over the available range in fig. 5.

Fig. 5

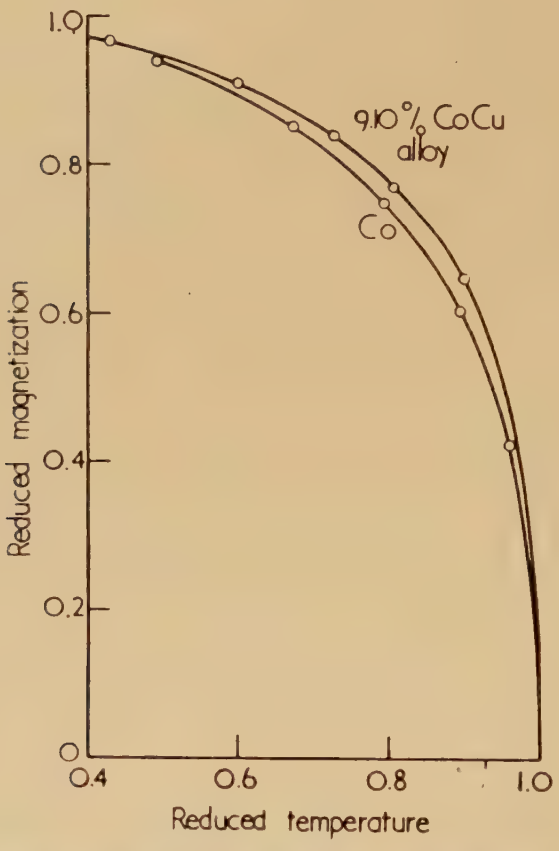

Reduced magnetization-temperature curves for pure cobalt and for the alloy containing 9·10 atomic % of copper.

§ 6. Discussion

The value of $2{\cdot}0\pm0{\cdot}1$ e.g.s. units per 1% change in composition estimated for the rate of decrease of magnetization with copper concentration in the alloys is equivalent to an initial decrease in the moment per atom at the rate of $2{\cdot}25\pm0{\cdot}1$ Bohr magnetons for 100% copper addition. Or, since the difference between the atomic numbers of cobalt and copper is two, a rate of 1·13 Bohr magnetons per electron.

The significance of this result is shown by plotting a graph of atomic moment against electron concentration for the alloys. In fig. 6 the full line is drawn with a gradient of 1·13 Bohr magnetons per electron, and it is made to pass through the value for the known moment of cubic cobalt, $1{\cdot}75_1$ magnetons. It is very striking how the extrapolated part of the line passes almost exactly through the moment for pure nickel, $0{\cdot}60_6$ magnetons (Weiss and Forrer 1929), and reaches zero moment at an electron concentration of 28·55. The old measurements by Alder (1916) on the magnetic moments of nickel–copper alloys extrapolate to give 28·60 as the electron concentration at which the moment becomes zero, although there is a suggestion in the work of Oliver and Sucksmith (1953) that the extrapolation is to a slightly lower electron concentration.

Fig. 6

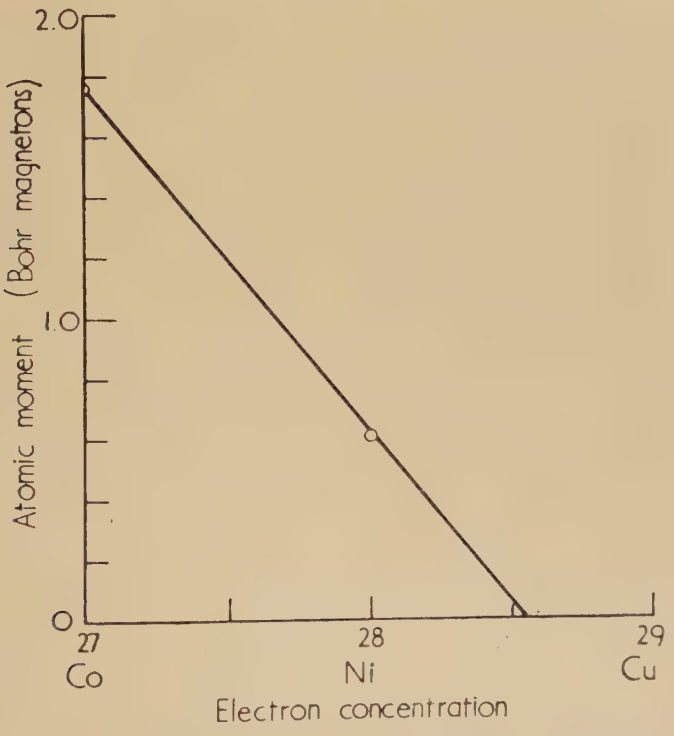

The derived variation of atomic moment with electron concentration for the cobalt–copper alloys, drawn through the moment for pure cobalt and extrapolated to zero moment.

The other important feature of the present work is the way in which the shape of the reduced magnetization-temperature curves changes with alloy composition. The curves increase in fullness as the copper concentration increases. This is a feature which seems not to have been observed before in any alloy system. In other systems for which data are available, such as the nickel–copper system (Alder 1916, Oliver and

Sucksmith 1953), any movement which occurs is towards less convex curves.

The increase in fullness of the reduced curves with increasing copper content that is shown quantitatively for the limiting cases in fig. 5 is also apparent from the data given for all the alloys in table 3. It should be emphasized that while the data in this table only give in their present form a qualitative indication of the increase in fullness, they do not depend at all on any extrapolation techniques other than those that are well established for the estimation of spontaneous magnetizations and of Curie points. The only way in which they could possibly give a spurious indication of the changing fullness is for the respective Curie temperatures to have been estimated wrongly. The Curie temperature at the solubility limit would have to be about 50°C higher than was actually observed, in order to restore the reduced magnetizations to coincidence with those for pure cobalt. An error of this magnitude does not seem possible. Moreover, to account for the uniform increase in reduced magnetization along the various rows of table 3, it would be necessary to postulate an error increasing uniformly with increasing copper content. Such a state of affairs is very unlikely.

In the original treatment of collective electron ferromagnetism, Stoner (1938) assumed as a first approximation that the energy associated with the magnetization, and arising from exchange, was proportional to the square of the magnetization. Hunt (1953) has extended this treatment by the inclusion of an additional term in the magnetic energy proportional to the fourth power of the magnetization, and controlled in magnitude by an adjustable, dimensionless parameter A. In this treatment, Hunt was able to calculate the forms of the reduced magnetization-temperature curves for nickel, nickel–copper alloys, and cobalt, and good agreement with experiment was obtained. The A values for nickel and cobalt were about the same, and as copper was added to nickel, A decreased and eventually became zero. Wohlfarth (1953) has given a justification for this variation of the coefficient A on alloying, and has suggested that A should decrease as the number of vacancies in the 3d band of the ferromagnetic metal decreases. Thus on this basis alone one would expect the shapes of the reduced magnetization-temperature curves of cobalt-copper alloys to behave similarly to those for nickel–copper alloys. However, with the additional possibility of a variation on alloying of Stoner's original coefficient, the observed increasing fullness is not necessarily in contradiction with the predictions of the collective electron treatment.

Further experimental work, both on this aspect and on the variation of magnetic moment with composition for other cobalt alloys is now in progress.

Acknowledgments

The author wishes to record his gratitude to Professor W. Sucksmith, F.R.S. for his help and advice during the course of this work. Thanks are also due to the Société Générale Métallurgique de Hoboken, Antwerp, for their kindness in presenting the cobalt on which the alloys were based.

References

Alder, M., 1916, *Thesis*, Zürich.
Hunt, K. L., 1953, *Proc. Roy. Soc.* A, **216,** 103.
Marian, V., 1937, *Ann. Phys. Paris*, [11] **7,** 459.
Meyer, A. J. P., and Taglang, P., 1950, *C. R. Acad. Sci.* (*Paris*), **231,** 612.
Myers, H. P., and Sucksmith, W., 1951, *Proc. Roy. Soc.* A, **207,** 427.
Oliver, D. J., and Sucksmith, W., 1953, *Proc. Roy. Soc.* A, **219,** 1.
Sadron, C., 1932, *Ann. Phys. Paris*, [10] **17,** 371.
Stoner, E. C., 1938, *Proc. Roy. Soc.* A, **165,** 372.
Sucksmith, W., 1939, *Proc. Roy. Soc.* A, **170,** 551.
Sucksmith, W., and Pearce, R. R., 1938, *Proc. Roy. Soc.* A, **167,** 189.
Sucksmith, W., and Thompson, J. E., 1954, *Proc. Roy. Soc.* A, **225,** 362.
Weiss, P., and Forrer, R., 1926, *Ann. Phys. Paris*, [10] **5,** 153 ; 1929, *Ibid.*, [10] **12,** 279.
Wohlfarth, E. P., 1953, *Rev. Mod. Phys.*, **25,** 211.

LX. *Deviations from Vegard's Law*

By J. Friedel
Centre de Recherches Métallurgiques de l'Ecole des Mines de Paris*

[Received November 15, 1954]

According to Vegard's law, the average lattice parameter x of a substitutional solid solution, as deduced from x-rays or density measurements, varies linearly with concentration c according to the equation

$$x=(1-c)x_1+cx_2,$$

if the two pure components have the same lattice structure with parameters x_1, x_2 (Barrett 1953). When they have different lattice structures, this law is still applicable to the radii r, r_1, r_2 of the atomic spheres ($4\pi r_i^3/3$=atomic volume).

Vegard's law is only approximate, and in this note we wish to point out that the deviations observed may be partly due just to the difference in the *compressibilities* χ_1, χ_2 of the two components. Such a difference should obviously produce a deviation : if for instance the solute atoms are much more compressible than the matrix, the lattice parameter of the solution should, at small concentrations c, be equal to that of the matrix.

This effect can be studied quantitatively using a simple model which we recall briefly (cf. Friedel 1954 for references). We shall also take this opportunity to correct a small error in the energy of solution obtained with this model.

Spherical holes with radius r_1 are cut in the matrix ; spheres with radius r_2, representing solute atoms, are introduced ; matrix and solute atoms are treated as continuous, homogeneous and isotropic media with the same elastic properties as the pure components ; they are constrained to touch along spheres of intermediary radius a.

One knows that, at infinite dilution,

$$(a-r_1)/(r_2-a)=\alpha=(1+\nu)\chi_1/2(1-2\nu)\chi_2, \quad . \quad . \quad . \quad . \quad . \quad (1)$$

where ν is Poisson's ratio in the matrix ; there is no dilatation in the matrix. But at finite concentration c, the matrix has a finite dilatation

$$e_1=+3\chi_1\,(r_2-r_1)\,c/(1+\alpha)\,\chi_2 a. \quad . \quad . \quad . \quad . \quad . \quad . \quad (2)$$

This may be shown as follows : according to (1), a solute atom with radius r_2 and compressibility χ_2 behaves as a solute atom with compressibility χ_1 and a radius r_2' such that $(a-r_1)/(r_2'-a)=(1+\nu)/2(1-2\nu)$. One knows that the volume of a medium with *uniform* elastic constants does not change on introducing internal stresses. The introduction of a solute atom thus changes the volume of the matrix by an amount w equal and

* Communicated by the Author.

opposite to the change of volume of this fictitious solute atom with compressibility χ_1. Thus $w=-4\pi a^2(a-r_2')$. This change is due to the action of surface stresses, which are fairly uniform for a uniform concentration c and a large enough volume of alloy (Eshelby 1954). It corresponds therefore to a uniform dilatation given by $e_1=3wc/4\pi r_1^3$. This can easily be put into the form (2) by the use of (1). Then, as is easily shown, the energy of solution σ is given by $\sigma(c)=(1-2c)\sigma(0)$. These formulae differ by a factor χ_1/χ_2 from those given previously (Friedel *loc. cit.*).

The radius r of the average atomic sphere of the solution is given in this model by

$$\frac{r-r_1}{r_1}=\tfrac{1}{3}\left[(1-c)e_1+3c\frac{a-r_1}{r_1}\right]=\frac{r_2-r_1}{r_1}\frac{\alpha+\chi_1/\chi_2}{\alpha+1}c. \quad . \quad . \quad . \quad (3)$$

This formula, valid for small concentrations c, predicts an initial slope $(r-r_1)/cr_1$ with the sign of r_2-r_1 and values between 0 for $\chi_1/\chi_2=0$ and $3(1-\nu)(r_2-r_1)/(1+\nu)r_1$ for $\chi_2/\chi_1=0$. It corresponds to Vegard's linear law (1) only for $r_1=r_2$ or $\chi_1=\chi_2$. A *positive* factor $P=(\chi_2-\chi_1)(r_2-r_1)$ should correspond to radii r smaller than those predicted by Vegard's law at both ends of the diagram ($c=0$ and 1), and thus to a positive curvature d^2r/dc^2. A *negative* value of P should correspond to a negative curvature.*

Most of the alloys with complete miscibility listed by Barrett (1953) follow these predictions : AuPd for instance follows Vegard's law ($\chi_2=\chi_1$), while AgPd (with $P>0$) shows a positive and CuPd (with $P<0$) shows a negative curvature. The quantitative agreement with experiment is however not very good, especially for components belonging to different periods. This is seen in the following table, which gives the computed and observed deviations,

$$y=(r-r_v)/(r_2-r_1)c=(\chi_1/\chi_2-1)/(\alpha+1)$$

in alloys rich in Al, Cu, Ag and Au. r is here the observed radius ; $r_v=r_1+(r_2-r_1)c$ that predicted by Vegard's law. The experimental data are from Barrett (*loc. cit.*), Axon and Hume-Rothery (1948) and Köster and Dannöhl (1936). Values of r_1, r_2, χ_1, χ_2 are taken from Mott and Jones (1936), ν from Köster (1948).

The discrepancies between the computed and observed values of y may have various causes : slight errors in the measured values of r, χ_1, χ_2, ν, important when r_1-r_2 is small ; large size factors $(r_2-r_1)/r_1$ for which first order elasticity theory is not valid ; electrochemical factors : difference in periods ; easy polarization of d shells in Cu, Ag, Au ; electron per atom ratio for overlapping bands.

The sharp bends observed in $r(c)$ for Mg-rich alloys have been explained by a lattice expansion due to such a band overlap (Raynor 1940, 1952 ; Jones 1949). The anomaly given for Zn in Al in the table is perhaps due to such an effect. It must also be noted that the distortions in the Al

* Fournet (1953) reached the same conclusions by considering interactions between nearest neighbours only.

Quantity y defined as above								
Solvent	Al		Cu		Ag		Au	
Solute	comp.	obs.	comp.	obs.	comp.	obs.	comp.	obs.
Li	−0·65	−0·85						
Mg	−0·25	−0·45						
Ni	—	—	+0·1	+0·8	—	—	0	−0·2
Cu	+0·15	+0·15	—	—	+0·05	−0·25	−0·05	−0·2
Zn	−0·1	−0·8	−0·3	−0·35	−0·15	+0·15	−0·3	+0·35
Ga	−0·15	−0·45	−0·35	−0·6	−0·2	−1·4	−0·35	−1·4
Pd			+0·1	+0·25	+0·15	+0·2	0·0	0·0
Ag			−0·1	−0·2	—	—	−0·15	−3
Cd			−0·4	−0·05	−0·25	−0·45	−0·35	−0·5
In			−0·45	−0·2	−0·3	−0·5	−0·4	−0·6
Sn			−0·35	−0·15	−0·25	−0·4	−0·3	−0·5
Pt			—	—	—	—	+0·06	+0·08
Au			+0·1	+0·2	+0·15	+2·6	—	—

matrix around Mg and Zn atoms, as deduced from nuclear magnetic resonance experiments, are not proportional to $a-r_1=[\alpha/(1+\alpha)](r_2-r_1)$, as predicted by our model (Bloembergen 1954).

References

Axon, H. J., and Hume-Rothery, W., 1948, *Proc. Roy. Soc.* A, **193**, 1.
Barrett, C. S., 1953, *Structure of Metals* (New York).
Bloembergen, N., 1954, *Bristol Conference.*
Eshelby, J. D., 1954, *J. Appl. Phys.*, **25**, 255.
Fournet, G., 1953, *J. Phys. Rad.*, **14**, 374.
Friedel, J., 1954, *Advances in Physics*, **3**, 446.
Jones, H., 1949, *Physica*, **15**, 3.
Köster, W., 1948, *Z. Metallk.*, **39**, 145.
Köster, W., and Dannöhl, W., 1936, *Z. Metallk.*, **28**, 248.
Mott, N. F., and Jones, H., 1936, *Metals and Alloys* (Oxford).
Raynor, G. V., 1940, *Proc. Roy. Soc.* A, **174**, 457 ; 1952, *Rep. Progr. Phys.*, **15**, 173.

LXI. *Glancing Angle Reflection of Elastic Waves from a Free Boundary*

By F. C. Roesler
Imperial Chemical Industries Limited, Butterwick Research Laboratories, Welwyn, Herts.*

[Received November 29, 1954]

Abstract

The usual treatment of the reflection of an irrotational wave from a free boundary results for glancing incidence in a seemingly trivial solution where all motion and stress vanishes. In experiment a pressure pulse made to travel at glancing angle along a free boundary trails a shear pulse, but this is properly speaking a diffraction phenomenon, the free boundary beginning at some finite distance. Though this diffraction process cannot be described completely in terms of the reflection treatment, it is possible, by using a limiting process and by changing the interpretation of the variables, to obtain in these terms the asymptotic state far down the free boundary. The result accounts for the trailing shear pulse and is amenable to experimental check.

§ 1. Introduction

The classical treatment of the reflection of plane elastic waves is given in many textbooks; convenient references are Jeffreys (1952) and Kolsky (1953). Below, the notation of the latter book is used.

A two-dimensional treatment applies in the plane strain case and in the plane stress case. In experimental terms, a plane strain case obtains if the wavelength is small compared with all dimensions of the block of material in which the waves travel. A plane stress case obtains if the waves are propagated in a plate such that the wavelength is large compared with the thickness of the plate. In this case a free boundary is given by a free edge of the plate. Below, the general part of the argument will be in terms of the plane strain case.

If an irrotational or P-wave (pressure wave P_1) meets a free boundary then the two boundary conditions, that both the normal and the shear stress vanish, entail that, in general, together with a P-wave (pressure wave P_2) an equivoluminal or S-wave (shear wave S_2) is reflected. The angles of incidence and of emergence for P_1, P_2 and S_2 will be denoted by α_1, α_2 and β_2, and the three amplitudes by A_1, A_2 and A_3. The amplitudes refer to particle displacement or particle velocity, these two quantities being proportional. It is well known that the angles satisfy the conditions $\alpha_2=\alpha_1$ and $\sin\beta_2/\sin\alpha_1=c_2/c_1$, c_2 and c_1 denoting the velocities in the unbounded medium of S- and P-waves respectively. The ratios A_2/A_1 and A_3/A_1 are functions of c_2/c_1 and of α_1 which are given in the

* Communicated by the Author.

literature and will be quoted below. Putting in these formulae $\alpha_1=\pi/2$ (glancing incidence) one finds $A_3=0$ and $A_2=-A_1$. This means that there is no shear wave, while incident and reflected P-waves cancel out completely, throughout the elastic half-space considered, so that there is neither motion nor stress anywhere.

In contrasting this solution with experiments, in which it is possible to make a P-wave of non-vanishing amplitude travel parallel to and along some plane-surfaced gap, cut or slot in the material, it must be remembered that the simple treatment of reflection refers to an infinite body, filling one half of space, with an infinite plane boundary. In experimental work there are limitations to the size of body which can be used, and while these are not trenchant when studying reflection at small angles of incidence they do for large such angles and certainly in

Fig. 1

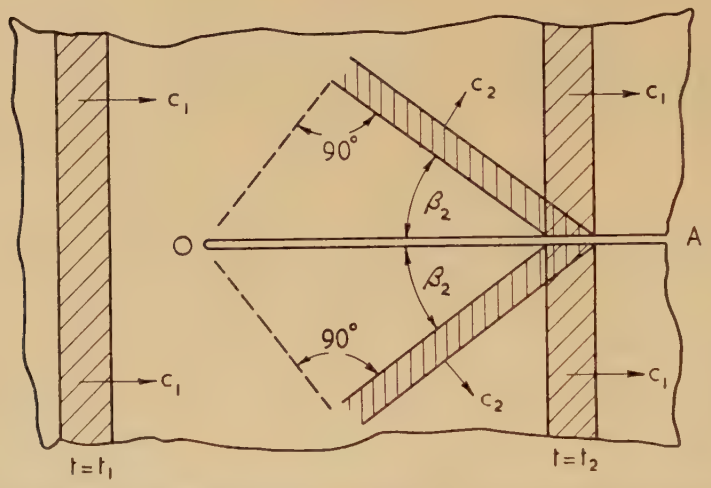

A plane P-wave is shown first ($t=t_1$) before it has reached the slot 0–A and later ($t=t_2$) after it has been split by the slot and draws along the free boundaries two S-wave pulses. P-waves and S-waves travel with different velocities c_1 and c_2 and $\sin\beta_2=c_2/c_1$.

the limiting case of glancing incidence make the correlation of the experimental situation with the mathematical model of the infinite half-space difficult. Consider a pressure pulse of finite length which is made to travel in a block of material towards a cut (cf. fig. 1). On making contact the wave-front is split and two separate pulses travel down the sides of the cut. Observation shows that then the pressure pulses trail shear pulses with an angle of emergence β_2 such that $\sin\beta_2=c_2/c_1$. The whole phenomenon may perhaps in a generalized sense be called 'reflection at a free boundary', but properly speaking it is a diffraction phenomenon, essentially linked to the beginning of the cut. This becomes more evident by considering the flow of energy. The energy which goes into the shear

waves must come from the initial pressure waves, so that these must progressively be weakened as they travel down the cut. Thus the state of the system of waves is not in any sense stationary, i.e. not even if considered in a coordinate system which moves down the cut at speed c_1.

From this discussion it is to be inferred that a complete description of the phenomenon depicted schematically in fig. 1 cannot be given in terms of the finite number of waves used in the simple treatment of reflection. Rather, such a complete description would have to be based on diffraction theory. Maue (1953) has published a general investigation of the diffraction problem for elastic waves. The present case might be accessible through his method of treatment, but the evaluation of the integral expressions encountered would not be easy. As will be seen, it is however possible to adapt the simple treatment of reflection such that it results in a solution in which the flow of energy from the pressure pulse to the shear pulse is constant and finite. This solution, found by a limiting process, appears to correspond to the asymptotic form of the solution of the diffraction problem proper, so that it should describe the situation near to the borders of the cut after the waves have travelled along it for a large distance.

The first careful discussion of the trailing shear wave is due to Schardin (1950). A mathematical treatment was given by Sauter (1950), who investigated the motion of an elastic half-space initiated by an impulse imparted to a straight line of the surface ("half-space struck by a knife edge"). In the solution terms were identified which describe shear waves trailed along the surface by the cylindrical P-wave diverging from the locus of disturbance. It was thus shown that the linear equations of elastic motion actually possess solutions of this type. The less elegant but much simpler treatment given below will confirm Sauter's main conclusion with regard to the dynamics of the process, namely that the pulse which trails the shear wave is not an ordinary P-wave.

§ 2. Reflection Near Glancing Angle

The idea of a limiting process which should lead from the ordinary, known solution of the reflection problem valid for $\alpha_1 < \pi/2$ to one with non-vanishing motion in the case $\alpha_1 = \pi/2$ was put forward by Goodier and Bishop (1952) who succeeded in obtaining certain interesting solutions in this way. These were later shown by Jardetzky (1952) also to be accessible by a general method. The limiting process used below is different from that of Goodier and Bishop and the solution which it is desired to establish by it is different from theirs. (As Goodier and Bishop have noted, their solution does not describe a situation of the type shown in fig. 1, since they postulate a wave the amplitude of which increases linearly with the distance from the free boundary.)

Consider the reflection of a plane P-pulse of finite length at near glancing angle, as depicted in fig. 2. In addition to the remarks on the usual reflection treatment embodied in the introduction, the following

may be noted. For an incident P-wave, and excluding dispersion in the material, the problem of the reflection of a pulse and that of the reflection of a sinusoidal wave are equivalent. The reflection of a P-wave produces no dispersion, and the shape of the pulse is conserved. It is then most convenient to assume a uniform, quasi-rectangular incident pulse, such that the particle velocity (and therefore also the stress) do not vary rapidly within the length of the incident pulse and that they go to zero smoothly at the front and at the tail. The reflected pulses follow in their shape the pattern set by the incident pulse. Under these assumptions the elastic matter of the half-space is at rest and stress-free at all points which, at a given moment, are not just being overrun by one of the three pulses P_1, P_2 and S_2.

Fig. 2

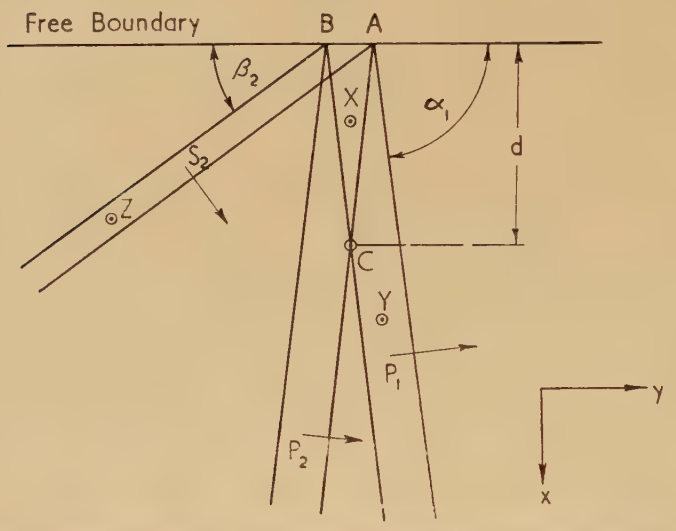

The plane P-wave pulse P_1 produces on reflection at the free boundary the two pulses P_2 and S_2. The angle of incidence α_1 is near to $\pi/2$ and one should imagine it to be even less different from $\pi/2$ than in the drawing, so that the distance d of the point C from the boundary is rather larger. The amplitudes of the wave motion and of the stress at points X and Z are then small compared with the amplitudes at point Y.

The assumptions made do as a matter of fact correspond closely to the real properties of pulses produced by explosions. They are not, however, intended as approximating assumptions, but are only introduced in order to allow of the representation of the reflection process by a simple picture. The conclusions to be derived from this should (suitably reformulated) hold for pulses or waves of arbitrary shape.

In fig. 2, α_1 is near to $\pi/2$ and the amplitude A_3 of the S_2 pulse is therefore small compared with the amplitude A_1 of the P_1 pulse,

$$A_3/A_1=\delta \quad . \quad . \quad . \quad . \quad . \quad . \quad . \quad . \quad (1)$$

where δ is a small number. Also, the two amplitudes A_1 and A_2 of the P_1 and of the P_2 pulse respectively are of but slightly different magnitude, though of opposite sign. Thus

$$(A_1+A_2)/A_1=\epsilon \quad . \quad . \quad . \quad . \quad . \quad . \quad . \quad . \quad (2)$$

where ϵ is another small number. The assertions condensed in (1) and (2) are based on the classical laws for reflection, from which the quantities δ and ϵ are known as functions of α_1 and of c_2/c_1, and it is known that for $\alpha_1 \to \pi/2$ there results $\delta \to 0$, $\epsilon \to 0$. Now in fig. 2 there is a region of the half-space marked by the triangle ABC within which the effects of the two pulses P_1 and P_2 superpose. Within this region, say at point X, the amplitude of the total wave motion is small, of order ϵ, as compared with the amplitude in the pulse P_1 by itself, say at point Y. A third point Z has been marked at which the amplitude of the shear pulse is alone effective, and here the amplitude of the wave motion will be small, of order δ, in comparison with that of the incident P_1 pulse (at point Y).

From the situation depicted in fig. 2 the following inference must be drawn with regard to the glancing incidence case. As α_1 approaches the glancing angle not only will the P_1 and the P_2 pulse cancel more and more completely, so that ϵ and δ become smaller and smaller, but also the point C will move further and further away from the boundary, such that the distance d tends to infinity as $1/(\pi/2-\alpha_1)$, and the regions occupied by the two pulses P_1 and P_2 will coalesce more and more. In effect, the nearer α_1 is to $\pi/2$, the further away from the boundary one has to look for regions where the amplitude of the wave motion is given by A_1 and A_2 singly. Nevertheless, A_1 and A_2 are the relevant quantities in the classical formulae describing the reflection and it is A_1 and A_2 singly which must be measured in order to obtain data which should verify those formulae. In the case $\alpha_1=\pi/2$, however, the amplitudes A_1 and A_2 are not experimentally definable quantities, since the two pulses P_1 and P_2 can no longer be separated. The point C is now at infinity and the region beyond C therefore not accessible to observation.

§ 3. The New Identification Suggested

The above discussion has shown that there is no experimentally well-defined quantity which in the case of glancing incidence could be identified with the pulse P_1. One may tentatively infer that if it is desired to describe a pulse travelling with velocity c_1 parallel to a free boundary this pulse should be identified with the superposition of P_1 and P_2. It must be stressed, recalling the discussion of fig. 1, that by a treatment in which the available variables are (arbitrarily) limited to the three amplitudes of the three plane waves of the half-space model one cannot hope to describe completely the transient phenomena caused by a wave front meeting a cut, as in fig. 1. Granting this, and considering the situation in regions of the solid at a long distance from the beginning of such a cut and near, comparatively, to its borders one may expect that

the initial pulse has here become much modified because of the boundary. Qualitatively, this makes it plausible to regard the type of pulse observed in these regions as a superposition of ' incident ' and ' reflected ' waves (cf. Schardin's (1950) discussion). One may therefore hope that by adopting the identification of the observed pulse with the superposition P_1+P_2 one will approximate successfully to the dynamical state far down the cut. In other words, the attempted identification is a guess as to the form of the asymptotic solution of the diffraction problem proper.

By these considerations one is led to inquire whether δ and ϵ as defined by (1) and (2) tend to zero with $\alpha_1 \to \pi/2$ in such a fashion that the ratio δ/ϵ possesses a finite value in the limit. By referring to the two equations which correspond to the two conditions at the free boundary and which link the quantities A_1, A_2 and A_3 one finds that one of these two equations is sufficient to determine the ratio δ/ϵ. It is the relation which expresses that the normal stress on the boundary vanishes and it reads (see. for instance, Kolsky (1953), eqn. (2.42)) :

$$\frac{A_3}{A_1+A_2} = \frac{\sin \alpha_1 \cos 2\beta_2}{\sin \beta_2 \sin 2\beta_2}. \quad . \quad . \quad . \quad . \quad . \quad . \quad (3)$$

Putting in this $\sin \alpha_1 = 1$ corresponding to $\alpha_1 = \pi/2$ one obtains the required limiting value of the ratio δ/ϵ. The relation may be re-written in various ways, for instance by introducing the quantity c_2/c_1 or the value of Poisson's ratio for the material as independent variable. It is seen from (3) that the limiting value of δ/ϵ as $\alpha_1 \to \pi/2$ is determinate and finite.

The other boundary condition. that the shear stress vanishes, reads (see, for instance, Kolsky (1953), eqn. (2.41)) :

$$\frac{A_3}{A_1-A_2} = \frac{2 \cos \alpha_1 \sin \beta_2}{\cos 2\beta_2}. \quad . \quad . \quad . \quad . \quad . \quad . \quad . \quad . \quad (4)$$

Now $\sin \beta_2$ and $\cos 2\beta_2$ are finite for $\alpha_1 = \pi/2$, but $\cos \alpha_1$ vanishes as the glancing angle is approached. Thus in order to satisfy (4) for a finite A_3 it must be assumed that (A_2-A_1) approaches infinity when α_1 tends to $\pi/2$. Since (A_1+A_2) has been taken to be finite, this implies that A_1 and A_2 are of opposite sign and both become infinite in absolute magnitude. The second boundary condition is then also satisfied.

The introduction of infinite amplitudes A_1 and A_2 asks for some further discussion. In the phenomenon, with the suggested description adopted, neither (A_1-A_2) nor either of these variables singly appears as an observable quantity. There is therefore, in principle, no objection to attributing infinite values to the variables A_1 and A_2. On the other hand it is obvious that both boundary conditions must in some way be satisfied by the actual stresses in the material. One may therefore well ask for a discussion of the second boundary condition in terms of such variables describing the wave motion as remain finite. One way to bring out a second finite quantity, complementary to (A_1+A_2), is to define

$$\cos \alpha_1 (A_1-A_2) \equiv \eta. \quad . \quad . \quad . \quad . \quad . \quad . \quad . \quad . \quad (5)$$

From (4) one finds in the limit $\alpha_1 \to \pi/2$

$$\eta/\delta = \frac{\cos 2\beta_2}{2 \sin \beta_2} . \quad . \quad . \quad . \quad . \quad . \quad . \quad . \quad . \quad . \quad (6)$$

As regards the ratio δ/ϵ discussed further above, one finds from (3) for $\alpha_1 \to \pi/2$:

$$\delta/\epsilon = \frac{\cos 2\beta_2}{\sin \beta_2 \sin 2\beta_2} . \quad . \quad . \quad . \quad . \quad . \quad . \quad . \quad . \quad (7)$$

The two relations (6) and (7) completely specify all variables. The amplitudes A_1, A_2 and A_3 enter into all observable quantities only through δ, ϵ and η, which are all finite.

The argument above shows that with the values of δ, ϵ and η given by (6) and (7) one may obtain a description of a finite shear pulse trailed along a free boundary by a superposition (with finite sum) of a pressure and of a tension pulse, and that all boundary conditions are satisfied in this description. It is worth noting that the superposition P_1+P_2, though it travels with velocity c_1, is not an ordinary P-pulse. The facts that (P_1+P_2) is a plane pulse and that the second boundary condition is satisfied must imply the presence of a shear stress in all surface elements parallel to the boundary and situated in the (P_1+P_2) pulse, independently of the distance from the boundary. (At the boundary, it is this shear stress which cancels the shear stress due to the S_2 pulse.) Of course, in an ordinary P-pulse travelling in the same direction this type of shear stress is absent. One may picture the state of affairs in the (P_1+P_2) pulse by saying that the flank of the pulse which moves along the free boundary experiences a drag. If the state of stress in the (P_1+P_2) pulse is represented by a stress ellipsoid, this will be tilted with reference to the boundary. In Sauter's (1950) paper it was pointed out that in a pulse travelling with velocity c_1 along a free boundary such a rotation of the stress ellipsoid (from its position for an ordinary P-pulse travelling in the same direction) must occur. Combined with the existence of shear stress in surface elements parallel to the boundary there is in the (P_1+P_2) pulse a flow of energy towards the boundary, across the pulse. This balances the energy going into the S_2 pulse.

§ 4. Conditions for Comparison with Experiment

In order to test the proposed description of the glancing angle reflection by an experiment of the type shown in fig. 1 it would be desirable to measure quantities which determine the ratios δ/ϵ and η/δ at a number of points along the cut. The experimental values and their trend should be compared with the predictions (6) and (7) for the asymptotic values. It is not possible on the basis of the present treatment to say how fast the asymptotic values are approached and for this information one has to look to experiment.

There are, of course, many quantities which might be determined in experiment and serve to evaluate the ratios δ/ϵ and η/δ. For every

suitable pair of such functions of the wave amplitudes one could work out the predictions corresponding to (6) and (7). Here, this will be done for certain stress variables which can be measured in experiments on plates, using photo-elastic methods. The only variation possible in such experiments is to vary the material of the plate. One given material may be taken to be characterized by the value of Poisson's ratio ν. Two variables which, when known in addition to ν, define the reflection process completely (which may thus be regarded as representative of δ/ϵ and η/δ) and which can be measured by photo-elastic methods are : (*a*) the ratio, τ_1/τ say, of the maximum shear stress in the (P_1+P_2) pulse and in the S_2 pulse, (*b*) the angle, θ say, by which the stress ellipsoid for the (P_1+P_2) pulse is turned away from the position for an ordinary P-pulse travelling in the same direction, i.e. when it has two of its axes parallel to the boundary.

If a two-dimensional treatment is to apply to waves in plates, the wavelength must be long compared with the plate thickness. Supposing this condition to be satisfied, one then has the plane stress case mentioned in the introduction. The whole treatment of the reflection problem, including the glancing angle case, can then be taken over from the plane strain case by just substituting for c_1 the velocity c_L of (long) pressure pulses in a (thin) plate (cf. Bishop 1953). The value which the angle β_2 attains for glancing incidence is now given by

$$\sin\beta_2 = \frac{c_2}{c_L} = \left(\frac{1-\nu}{2}\right)^{\frac{1}{2}}. \quad . \quad . \quad . \quad . \quad . \quad . \quad (8)$$

Measurement of β_2 can thus serve to determine the value of Poisson's ratio ν.

The chosen quantities τ_1/τ and θ both refer to stresses. This being so, it is most convenient to evaluate them directly from the condition of equilibrium at the boundary rather than through δ/ϵ and η/δ, on the basis of (6) and (7). This direct use of the boundary conditions would, however, be unfounded without the foregoing discussion in terms of amplitudes. To carry the argument through in detail, it is easiest to draw a diagram with Mohr's stress circles for both pulses. This is shown in fig. 3. The diagram is started by drawing the stress circle of the S_2 pulse. The origin of this must coincide with the origin of the diagram, since the state of stress in an S-pulse corresponds to a vanishing mean pressure (principal stresses equal and opposite in sign). The radius of the stress circle of the S_2 pulse is given by τ, the maximum shear stress in this pulse. Using (8), one finds the point B which defines the values of the shear and of the normal stress caused at the boundary by the S_2 pulse. Diametrically opposite is the point B′ which defines opposite, equal stresses, and through this the stress circle of the (P_1+P_2) pulse must pass. Its centre is found by using the general relation (Hooke's Law)

$$\epsilon_{xx} = \frac{1}{E}(\sigma_{xx} - \nu\sigma_{yy} - \nu\sigma_{zz}). \quad . \quad . \quad . \quad . \quad . \quad . \quad (9)$$

In the present case the normal stress in the z-direction, σ_{zz}, is zero (thin plate condition) and the displacement caused by the (P_1+P_2) pulse is independent of x, for the reason that P_1 and P_2 are plane pulses, whence the strain ϵ_{xx} is also zero. One therfore obtains from (9):

$$\sigma_{yy}=\frac{1}{\nu}\sigma_{xx}. \quad . \quad . \quad . \quad . \quad . \quad . \quad . \quad . \quad . \quad (10)$$

The origin of the stress circle for (P_1+P_2) is now defined as the point $\frac{1}{2}(\sigma_{xx}+\sigma_{yy})$ on the σ-axis and the diagram can be completed. One may read off relations which determine the desired ratio of the maximum shear stresses. Using (10) and simplifying one finds this to be

$$\frac{\tau_1}{\tau}=\left\{\nu^2+\left(\frac{1-\nu}{\nu}\right)^2\left(\frac{1-\nu^2}{4}\right)\right\}^{\frac{1}{2}}. \quad . \quad . \quad . \quad . \quad . \quad . \quad . \quad (11)$$

Fig. 3

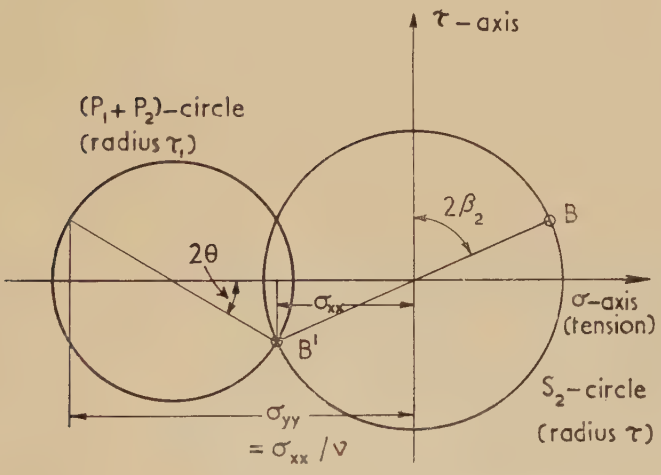

State of stress in S_2-pulse and in (P_1+P_2)-pulse represented by means of Mohr's stress circles for each pulse. The diagram corresponds to a value $\nu=0{\cdot}4$ and thin plate conditions.

Here τ_1 denotes the maximum shear stress in the (P_1+P_2) pulse, given by the radius of the relevant stress circle. One may also read off a relation which determines the angle θ by which the stress ellipsoid of the (P_1+P_2) pulse is rotated with reference to the boundary. Using again (10) the relation for the turning angle becomes

$$\tan 2\theta=\frac{2\nu^2}{(1-\nu)(1-\nu^2)^{\frac{1}{2}}}. \quad . \quad . \quad . \quad . \quad . \quad (12)$$

The formulae (11), (12) and (8) are not difficult to evaluate numerically. One finds, e.g. for Poisson's ratio $\nu=0{\cdot}30$, the ratio of shear stresses $\tau_1/\tau=1{\cdot}15$, the turning angle $\theta=7{\cdot}5°$ and the trail angle $\beta_2=36{\cdot}3°$. For the limiting value $\nu=0{\cdot}5$ one finds $\tau_1/\tau=0{\cdot}66$, $\theta=24{\cdot}5°$ and $\beta_2=30°$.

For a hypothetical value $\nu=0$ one finds $\tau_1/\tau=\infty$, which means that there is no trailing shear wave, and correspondingly one finds $\theta=0$. The trail angle β_2 tends to 45° as ν tends to zero.

The discussion above of possible experiments does not, of course, take proper account of practical restrictions. Mr. D. G. Christie of this laboratory has performed extensive experiments on the reflection of elastic waves, and among these some of the type suggested here. His results are given in a separate paper. It appears that there are considerable difficulties in the way of making exact measurements of τ_1/τ and of θ ; it is also difficult to make these measurements at a long distance from the beginning of the free boundary. Mr. Christie's results do however show that the turning of the stress ellipsoid in the (P_1+P_2) pulse occurs, and they show that even fairly near to the beginning of the free boundary the predictions represented by (11) and (12) give, in any case, the right order of magnitude.

Acknowledgments

The author is much indebted to Dr. H. Kolsky and Mr. D. G. Christie for information and illuminating comment. He also wishes to record his thanks to Professor H. Schardin, who most kindly supplied references to the work done in Germany.

References

Bishop, R. E. D., 1953, *Quart. J. Mech. Appl. Math.*, **6,** 250.
Goodier, J. N., and Bishop, R. E. D., 1952, *J. Appl. Phys.*, **23,** 124.
Jardetzky, W. S., 1952, *J. Appl. Phys.*, **23,** 1279.
Jeffreys, H., 1952, *The Earth*, 3rd edition (Cambridge : University Press).
Kolsky, H., 1953, *Stress Waves in Solids* (Oxford : Clarendon Press).
Maue, A. W., 1953, *Z. angew. Math. Mech.*, **33,** 1.
Sauter, F., 1950, *Z. angew. Math. Mech.*, **30,** 149, 203.
Schardin, H., 1950, *Glastechn. Ber.*, **23,** 1, 67, 325.

LXII. *Reflection of Elastic Waves from a Free Boundary*

By D. G. Christie
Imperial Chemical Industries Limited, Butterwick Research Laboratories, Welwyn, Herts.*

[Received November 29, 1954]

Abstract

A dilatation wave incident on a free surface produces reflected dilatation and distortion waves. The relation between the amplitudes of these waves has already been calculated when the reflection occurs at the surface of an elastic half-space. It is shown in this paper that a similar relation holds for a plane pulse travelling in a plate and reflected from a free edge. An experimental method is described for investigating this reflection problem, together with the results obtained. Agreement between experiment and the classical reflection theory is found to be good, provided that care is taken in defining the observed variables. At glancing incidence the phenomenon should be considered as one of diffraction; however Roesler (1954) has shown that by suitable choice of variables an explanation is possible in terms of reflection theory. His results are found to be in agreement with experiment.

§ 1. Introduction

The general equations of motion for a perfectly elastic homogeneous solid can be solved to show that for an infinite body two types of wave exist: a dilatation or P wave and a distortion or S wave. For a finite solid the problem of finding solutions of the general equations for given boundary conditions has only been carried out for the simplest cases, for example for cylinders by Pochhammer (1876 and Chree (1889) (see also Love 1927) and for plates by Lamb (1917) and Rayleigh (1889). These solutions are for continuous sinusoidal waves; an extension to pulses travelling along a bar has been given by Davies (1948), and Prescott (1942) has treated the problem of plane waves of arbitrary form reflected from the surface of an elastic half-space.

If the length of a pulse is short compared with the dimensions of the body in which it is travelling, it may be assumed that, except at the instant of reflection from the boundaries, the pulse will travel as if in an infinite medium. If the laws of reflection are known then in a bounded medium the subsequent history of any disturbance can be found by considering its propagation as if in an infinite medium and all possible reflections of it from the boundaries. This method has been applied by Kolsky (1954) to the propagation of a pulse along a cylindrical bar.

* Communicated by the Author.

The theoretical expressions for the reflection of plane dilatation and plane distortional sinusoidal waves from the free surface of an elastic half space have, for instance, been given by Kolsky (1953) together with typical graphs of the amplitudes of the reflected waves. Prescott has carried out a similar calculation for an arbitrary shaped elastic pulse. Bishop (1953) has shown that plane strain and plane stress solutions for a particular problem can be changed from one into the other by suitable change of the elastic constants. Thus it might be expected that the same results hold for a plane dilatation pulse travelling through a semi-infinite plate and reflected from its free edge as for a plane dilatation pulse reflected from the surface of an elastic half space. In the first part of this paper this will be shown to be correct; the breakdown of the theory for glancing incidence will then be noted and the modification proposed by Roesler (1954) discussed.

The plates used in the experiments are stress birefringent, and the stress pulses are observed as a series of interference fringes using polarized light. The second section of the paper will deal with the relation between the observed fringes and the pulse amplitudes. A further section will give the effect on the fringe pattern of superimposing two elastic pulses. This is necessary to find the correction to be applied to the fringe count for the determination of the absolute amplitude of a pulse which is superimposed on a known stress field. Finally the experimental results will be shown to justify the theoretical predictions, provided the modification close to glancing incidence is accepted.

§ 2. Reflection of Plane Dilatation Pulse from the Edge of a Plate

The more important symbols used are given here for reference :—

u, v, w=displacements in x, y and z directions.

μ and λ=Lamé's elastic constants.

ρ=density of the medium.

c_1=velocity of dilatation waves in a plate under plane stress conditions=$[4\mu(\lambda+\mu)/\rho(\lambda+2\mu)]^{1/2}=[E/\rho(1-\nu^2)]^{1/2}$, where E=Young's modulus and ν=Poisson's ratio.

c_2=velocity of distortion waves in a plate=$(\mu/\rho)^{1/2}$.

σ_{ij}=stress on a plane normal to i in a direction j, where i, j can be x, y or z.

For a pulse travelling in an infinite plate which is normal to the z axis, if it is assumed that the displacements u and v in the x and y direcl tions respectively are independent of z and further that the stress normal to the plate, σ_{zz}, is everywhere zero, then two solutions of the genera- equations are possible :

$$\rho\frac{\partial^2\phi}{\partial t^2}=\frac{4\mu(\lambda+\mu)}{\lambda+2\mu}\left(\frac{\partial^2\phi}{\partial x^2}+\frac{\partial^2\phi}{\partial y^2}\right) \text{ and } \rho\frac{\partial^2\psi}{\partial t^2}=\mu\left(\frac{\partial^2\psi}{\partial x^2}+\frac{\partial^2\psi}{\partial y^2}\right)$$

where functions ϕ and ψ characterize the dilatation and distortion waves and

$$\left.\begin{aligned} u &= \frac{\partial \phi}{\partial x} + \frac{\partial \psi}{\partial y} \\ v &= \frac{\partial \phi}{\partial y} - \frac{\partial \psi}{\partial x} \end{aligned}\right\} \quad \ldots\ldots\ldots \quad (1)$$

The velocities of the two waves are $c_1=[4\mu(\lambda+\mu)/(\lambda+2\mu)]^{1/2}$ and $c_2=(\mu/\rho)^{1/2}$ where μ and λ are the Lamé elastic constants.

Fig. 1

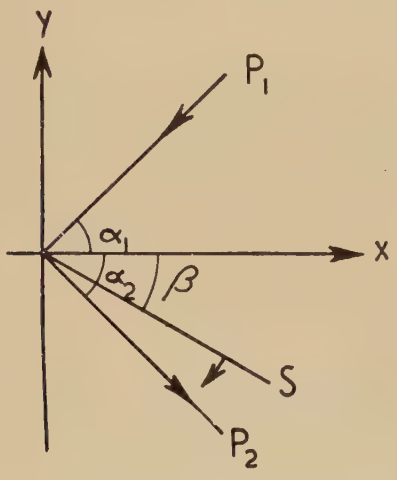

In general the reflection of either a dilatation or a distortion wave from a free boundary produces both distortion and dilatation waves. The amplitudes and angles of reflection of the waves generated when a plane dilatation pulse is reflected from a free boundary under conditions of plane stress can be found from the known solution for plane strain (Kolsky 1953) by substituting new expressions for the elastic constants (Bishop 1953). The method of solution by solving the general elastic equations with suitable boundary conditions is, however, outlined here to show what assumptions are inherent in the final expressions. Consider a plane dilatation pulse P_1, travelling in a plate and incident at an angle α_1 on a free plane edge of the plate (fig. 1) and producing two reflected pulses P_2 and S at angles α_2 and β respectively. The arrows in the figure represent the directions of the particle displacements. It is here assumed and in the calculations which follow, that the wave length or pulse length is large compared with the thickness of the plate. The pulses can be defined by :—

$$\left.\begin{aligned} &\text{for } P_1 \quad \phi_1=\Phi_1(c_1t+x\cos\alpha_1+y\sin\alpha_1), \\ &\text{for } P_2 \quad \phi_2=\Phi_2(c_1t-x\cos\alpha_2+y\sin\alpha_2), \\ &\text{for S} \quad\ \ \psi=\Psi(c_2t-x\cos\beta+y\sin\beta). \end{aligned}\right\} \quad \ldots\ldots \quad (2)$$

For the case of plane stress, i.e., $\sigma_{zz}=0$, it can be shown by direct calculation

that the boundary conditions $\sigma_{xx}=\sigma_{xy}=0$ at $x=0$ for all t and y can be satisfied if

$$\frac{\sin\alpha_1}{c_1}=\frac{\sin\alpha_2}{c_1}=\frac{\sin\beta}{c_2} \quad . \quad . \quad . \quad . \quad . \quad . \quad . \quad (3)$$

i.e., $\alpha_1=\alpha_2=\alpha$, say and $\Phi_1''(c_1t+y\sin\alpha)=\Psi''\left\{\frac{c_2}{c_1}(c_1t+y\sin\alpha)\right\}$.

Then if the displacement amplitudes of the three pulses of eqn. (2) are A_1, A_2, and A_3 respectively, the boundary condition that $\sigma_{xx}=0$ for all t and y becomes

$$(A_1+A_2)(\cos 2\beta\sin\alpha)-A_3\sin 2\beta\sin\beta=0 \quad . \quad . \quad . \quad . \quad (4)$$

and the other boundary condition $\sigma_{xy}=0$ at $x=0$ for all t and y gives

$$2(A_1-A_2)\sin\beta\cos\alpha-A_3\cos 2\beta=0. \quad . \quad . \quad . \quad . \quad (5)$$

Figure 2 is a graph of the ratio of the amplitudes $-(A_2/A_1)$ and (A_3/A_1) plotted for $c_1/c_2=1{\cdot}76$ which is the value of this ratio for unplasticized ' Perspex ' (a form of polymethyl methacrylate), the experimental material

Fig. 2

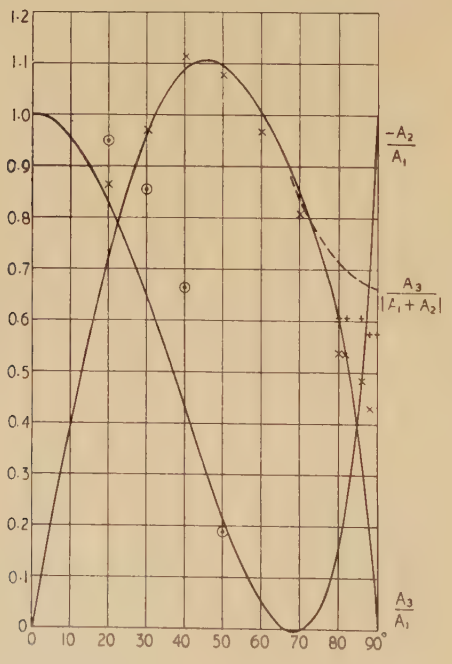

⊙ Experimental points for reflected P_2 pulse. A_3/A_2
× ,, ,, ,, ,, S ,, A_3
\+ ,, ,, ,, ,, S ,, $\overline{|A_1+A_2|}$

used. When $\alpha=90°$, eqns. (4) and (5) give $A_3=0$. Further, since at this angle the incident and reflected P waves superpose and $A_1=-A_2$, these two waves exactly cancel each other. Thus when α is made equal to 90° in

EXPLANATION TO PLATES 7—11

Plate 7

Stress pulses diverging from a point explosive charge detonated on the upper edge of a $\frac{5}{32}$ in. thick sheet of ' Perspex '. Only part of the upper edge of the specimen is visible, and all the other boundaries are outside the field of view. The charge was detonated at the top left hand corner of the picture.

Plate 8

Plane stress pulse travelling down a $\frac{1}{8}$ in. thick sheet of ' Perspex ' and incident at an angle of 30° on a free edge of the sheet. The remaining edges are outside the field of view. Pictures 4 to 8 show the reflection of the incident dilatation pulse as both dilatation and distortion pulses and pictures 6 to 8 the production of cracks.

Plate 9

One picture from eight different experiments showing variation of the intensity of the reflected dilatation and distortion pulses produced when the incident dilatation pulse is reflected at different angles of incidence from a free boundary. The material is $\frac{1}{8}$ in. thick sheet ' Perspex '.

Plate 10

Plane dilatation pulse travelling down a $\frac{1}{8}$ in. thick sheet of ' Perspex ' and reflected at glancing incidence from the right hand edge. The other edges except the lower one are outside the field of view.

Plate 11

Reflection of a plane dilatation pulse from both sides of a slit cut in a $\frac{1}{8}$ in. thick sheet of ' Perspex '. The edges of the specimen are outside the field of view and the photographs were taken using plane polarized light to show the directions of the principal stresses.

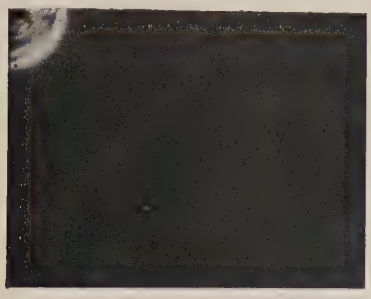

2. 8·5 μ sec.

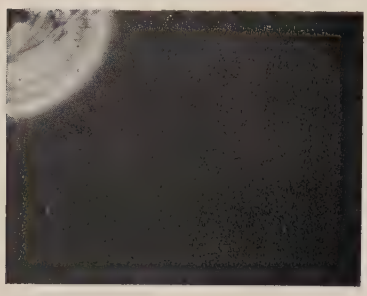

3. 20·0 μ sec.

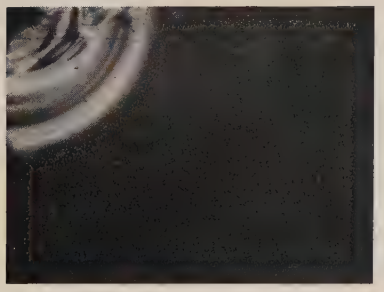

4. 29·4 μ sec.

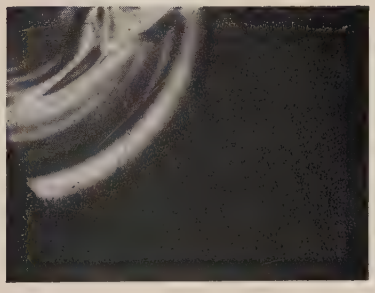

5. 42·2 μ sec.

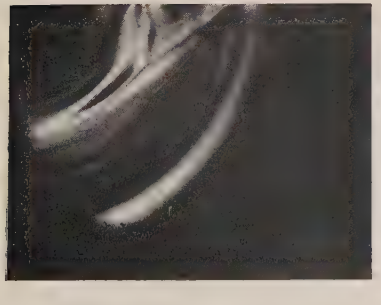

6. 54·7 μ sec.

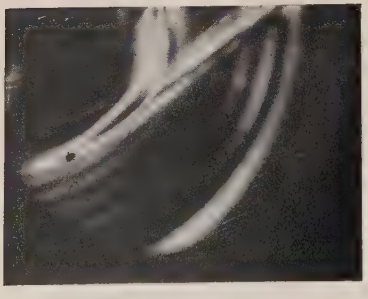

7. 67·2 μ sec.

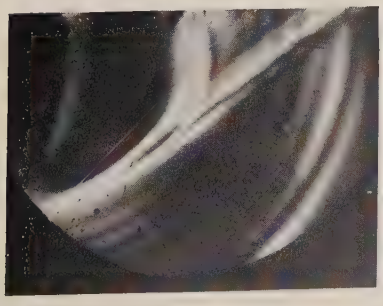

8. 69·3 μ sec.

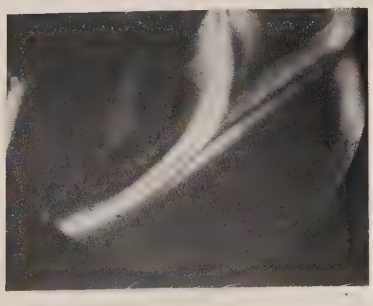

9. 93·5 μ sec.

(All times measured from an arbitrary zero)

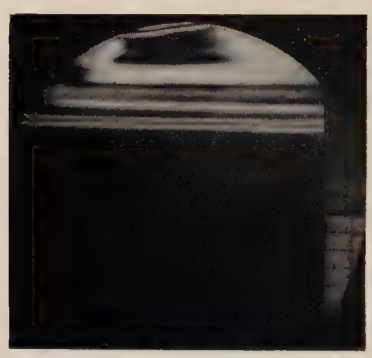

1. 25·3 μ sec.

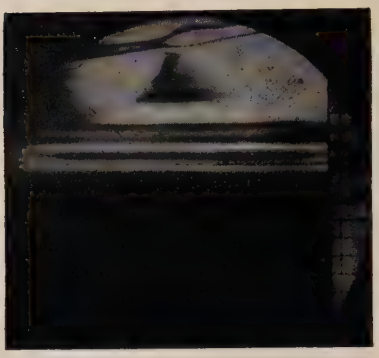

2. 37·2 μ sec.

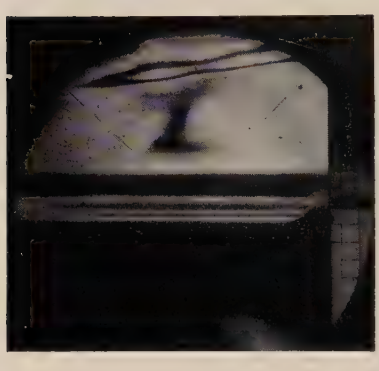

3. 48·3 μ sec.

4. 59·0 μ sec.

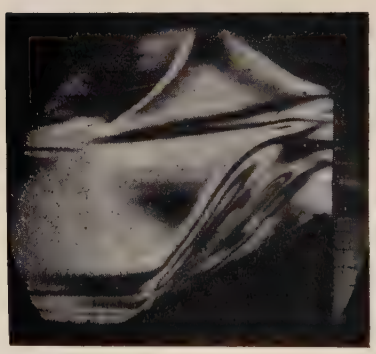

5. 71·1 μ sec.

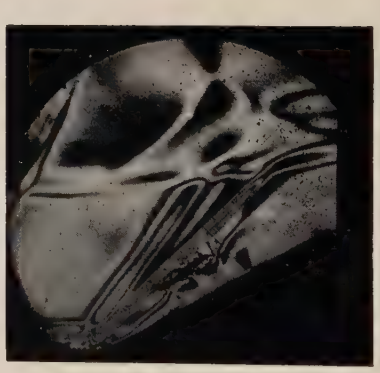

6. 84·0 μ sec.

7. 96·1 μ sec.

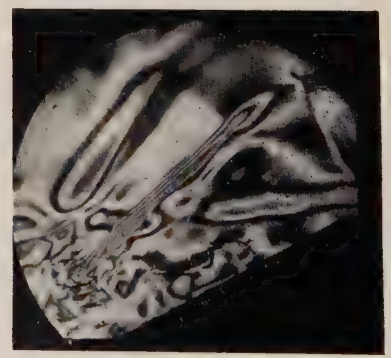

8. 108·2 μ sec.

(All times measured from an arbitrary zero.)

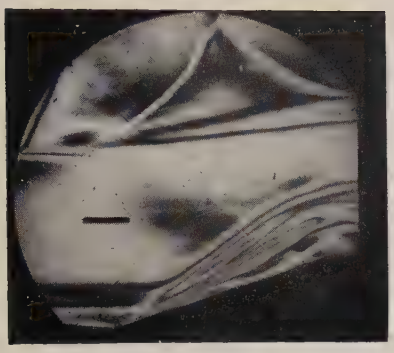

20°

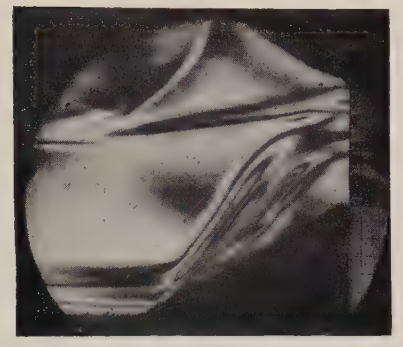

30°

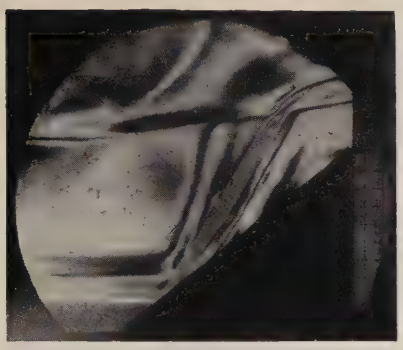

40°

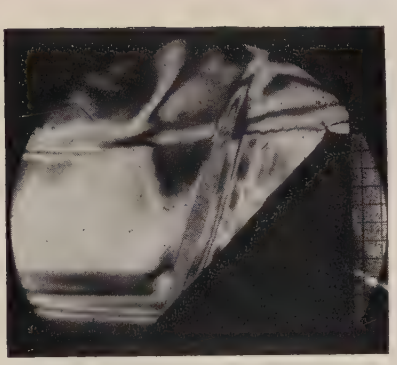

50°

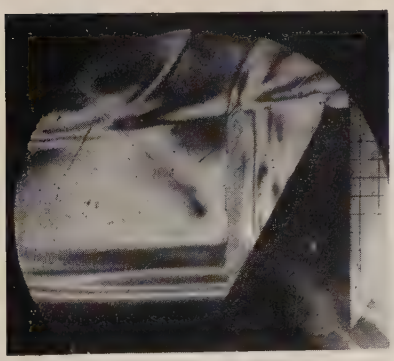

60°

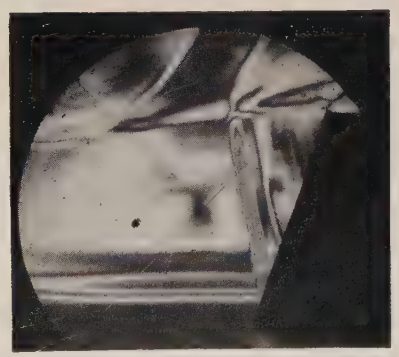

70°

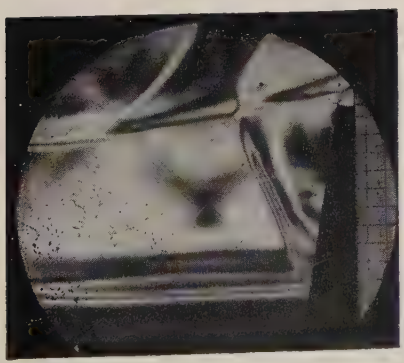

80°

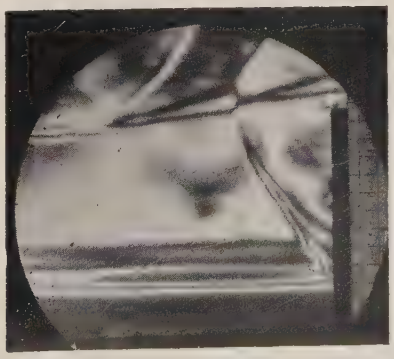

90°

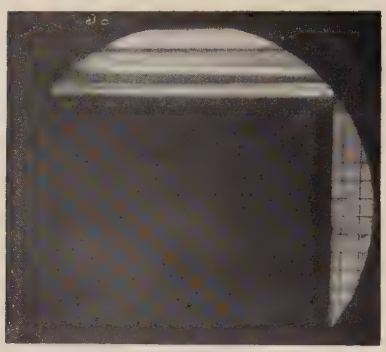

1. 25·0 μ sec.

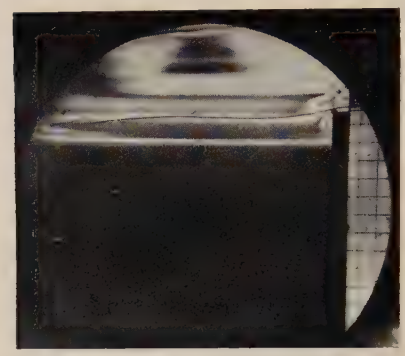

2. 35·8 μ sec.

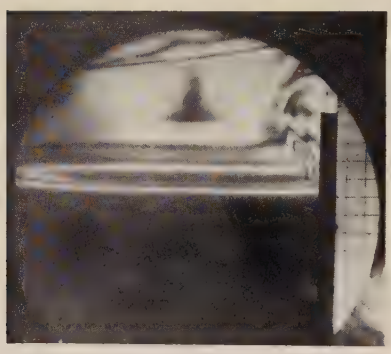

3. 48·2 μ sec.

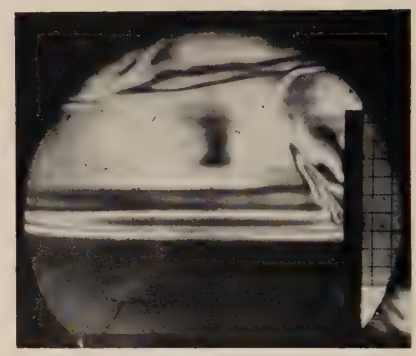

4. 58·7 μ sec.

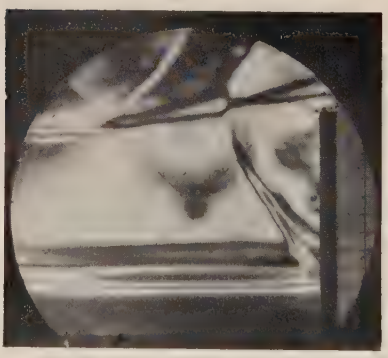

5. 71·1 μ sec.

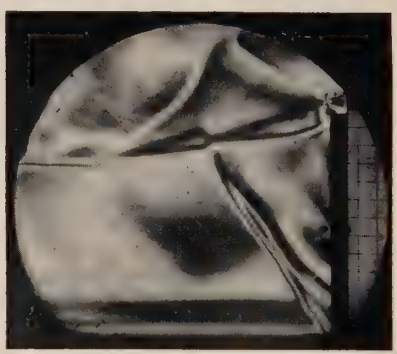

6. 84·2 μ sec.

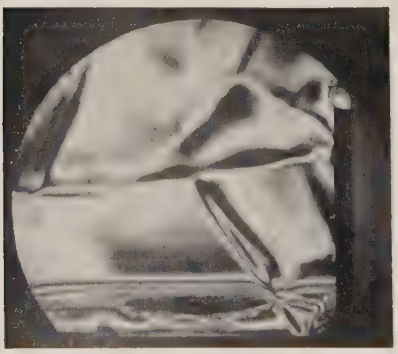

7. 96·1 μ sec.

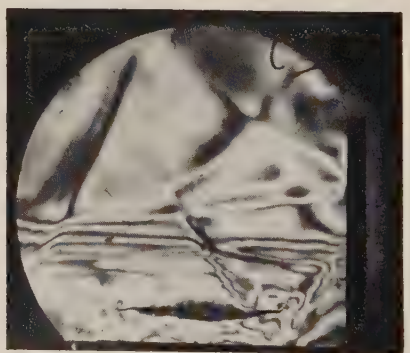

8. 109·2 μ sec.

(All times are

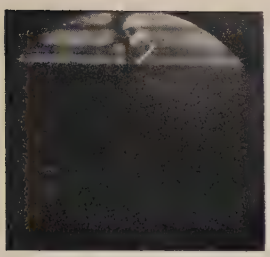

1. 0·0 μ sec.

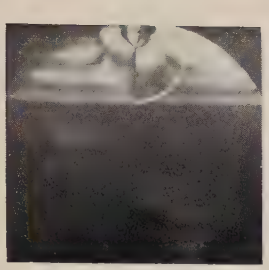

2. 4·5 μ sec.

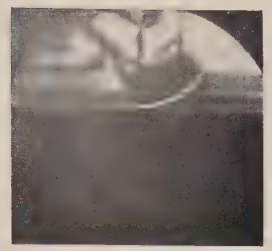

3. 12·1 μ sec.

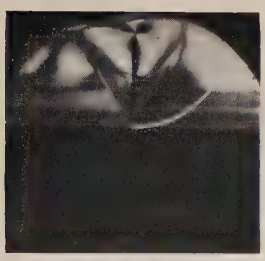

4. 16·5 μ sec.

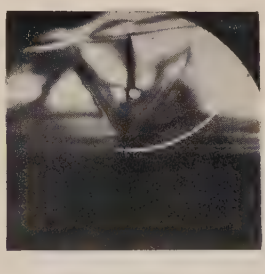

5. 24·3 μ sec.

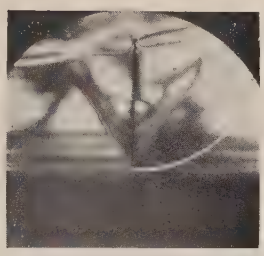

6. 28·8 μ sec.

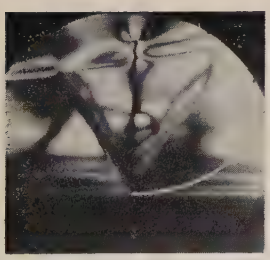

7. 34·3 μ sec.

8. 42·1 μ sec.

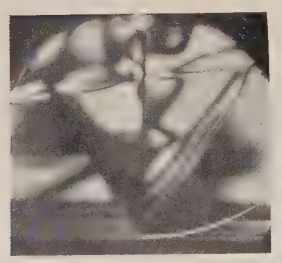

9. 51·9 μ sec.

(All times measured from an arbitrary zero)

the equations a vanishing solution is obtained which corresponds to zero displacement of the specimen. Experimentally it is found that a P wave travelling at glancing incidence along a free boundary produces a trailing S wave. Schardin (1950) has obtained the effect in glass, and Plate 7 shows a similar result in a sheet of ' Perspex '. Here a small charge of lead azide, detonated on the upper edge of the sheet, produced cylindrically diverging P and S pulses. The photographs only show part of the pulses, the remainder of the specimen being outside the field of view. The faster of the two pulses, the P pulse, can be seen to produce a trailing S pulse from the upper edge of the plate. From the geometry of the system the trailing S pulse should be plane and tangential to the circular S pulse and this can be seen to be the case.

Goodier and Bishop (1952) obtained a solution for glancing incidence and found that for an incident P pulse a trailing S pulse was formed but in their solution a wave whose amplitude increased continuously with distance from the reflecting edge was also necessary to satisfy the boundary conditions.

At glancing incidence the P_1 and P_2 pulses are completely superposed and Roesler (1954) has obtained a solution by considering the observed quantities to be (A_1+A_2) and A_3, since A_1 and A_2 no longer have separate identities. Carrying these ideas a little further, then for angles less than but approaching 90°, the observed quantities near the reflecting edge will still be the vector sum (A_1+A_2) and A_3, it being necessary to go a considerable distance away from the reflecting edge to measure A_1 and A_2 separately. So that for experiments on finite specimens it is the value of $A_3/|A_1+A_2|$ which must be considered, not A_3/A_1. The value of the function $A_3/|A_1+A_2|$ is shown on the graph for angles of incidence approaching 90°.

§ 3. Stress Optical Relations

Experimentally, plane fronted pulses were reflected at angles between 0° and 90° from a free edge of a transparent plate of ' Perspex '. The material is stress birefringent and the pulses were observed using polarized light. It is therefore necessary to know the relation between the displacement amplitudes of the pulses and the observed fringes. For two beams of light polarized in the directions of the principal stresses the relative optical path difference, Δn, per unit path length for normal incidence on the plate is proportional to the difference of principal stresses $(\sigma_{max}-\sigma_{min})$ in the plane of the plate. Using circularly polarized light and the polarizer and analyser crossed, the first dark fringe will occur when $\Delta n=\lambda'$=the wavelength of the light. If f denotes the fringe value of the material, i.e., the difference of principal stresses per fringe per cm path traversed, then if d=thickness of plate, m=fringe order (which may be fractional) and τ_{max}=maximum shear stress, which is at an angle of $\pi/4$ to σ_{max} and σ_{min},

$$mf/d=(\sigma_{max}-\sigma_{min})=2\tau_{max}. \quad . \quad . \quad . \quad . \quad (6)$$

Methods have been developed for static stress analysis to determine the principal stresses individually. They involve extra experiments to measure either the directions of the principal stresses in the model, or measurement of the strain through the thickness of the model in the direction of observation (Coker and Filon 1931). For the dynamic problem of stress pulses travelling through a material it is very difficult to obtain these other independent measurements at the same instant as the fringe pattern is recorded. However, with a knowledge of the type of pulse, i.e., dilatation or distortion, it is possible to calculate the particle displacement in the pulse and also the stress amplitudes if required, from the photoelastic fringe patterns.

Consider a plane dilatation pulse and a plane distortion pulse travelling in the x direction in the plate and having identical pulse shapes in time. Then the particle displacements for the P pulse can be represented by

$$u_{\mathrm{P}}=\phi\left[C\left(t-\frac{x}{c_1}\right)\right]; \qquad v_{\mathrm{P}}=0$$

and for the S pulse by

$$u_{\mathrm{S}}=0; \qquad v_{\mathrm{S}}=\phi\left[C\left(t-\frac{x}{c_2}\right)\right]$$

where C is an arbitrary constant.

For a P pulse $\tau_{\max}$ is at an angle of $\pi/4$ to the wave front and therefore given by $\frac{1}{2}(\sigma_{xx}-\sigma_{yy})$.

Now
$$\sigma_{xx}=\frac{4\mu(\lambda+\mu)}{\lambda+2\mu}\frac{\partial u}{\partial x}+\frac{2\mu\lambda}{\lambda+2\mu}\frac{\partial v}{\partial y}$$
$$=-\frac{C}{c_1}\frac{4\mu(\lambda+\mu)}{\lambda+2\mu}\phi'\left[C\left(t-\frac{x}{c_1}\right)\right]$$

and
$$\sigma_{yy}=\frac{4\mu(\lambda+\mu)}{\lambda+2\mu}\frac{\partial v}{\partial y}+\frac{2\mu\lambda}{\lambda+2\mu}\frac{\partial u}{\partial x}$$
$$=-\frac{C}{c_1}\frac{2\mu\lambda}{\lambda+2\mu}\phi'\left[C\left(t-\frac{x}{c_1}\right)\right],$$
$$\therefore m_{\mathrm{P}}f/d=-\frac{C}{c_1}2\mu\phi'\left[C\left(t-\frac{x}{c_1}\right)\right].$$

For the S pulse $\tau_{\max}$ is in the plane of the wave front,

$$\therefore \tau_{\max}=\sigma_{xy}=\mu\left(\frac{\partial u}{\partial y}+\frac{\partial v}{\partial x}\right)$$
$$=-\frac{C}{c_2}\mu\phi'\left[C\left(t-\frac{x}{c_2}\right)\right],$$
$$\therefore m_{\mathrm{S}}f/d=-\frac{C}{c_2}2\mu\phi'\left[C\left(t-\frac{x}{c_2}\right)\right],$$
$$\therefore m_{\mathrm{P}}/m_{\mathrm{S}}=\frac{c_2}{c_1}\frac{\phi'\left[C\left(t-\frac{x}{c_1}\right)\right]}{\phi'\left[C\left(t-\frac{x}{c_2}\right)\right]}.$$

Therefore for corresponding points of dilatation and distortion pulses having equal amplitudes

$$m_P/m_S=c_2/c_1$$

so that denoting the observed fringe order of the three pulses P_1, P_2 and S of eqns. (2) by m_1, m_2 and m_3

$$\left.\begin{aligned} &\text{then} \quad A_2/A_1=m_2/m_1 \\ &\text{and} \quad A_3/A_1=c_2m_3/c_1m_1 \end{aligned}\right\} \quad . \quad . \quad . \quad . \quad . \quad . \quad . \quad (7)$$

§ 4. Stress Relations for Superimposed Stress Fields

The maximum shear stress τ_{max} is related to the stresses σ_{xx}, σ_{yy} and σ_{xy} referred to rectangular axes x, y by the equation

$$\tau^2_{max}=\tfrac{1}{4}(\sigma_{xx}-\sigma_{yy})^2+\sigma_{xy}^2. \quad . \quad . \quad . \quad . \quad . \quad . \quad . \quad (8)$$

Fig. 3

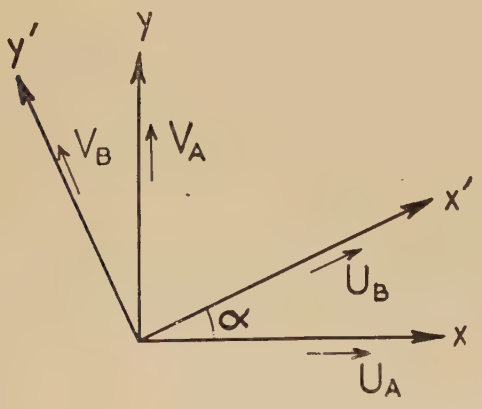

Consider the summation of two stress fields A and B, the fields being defined by their displacements (fig. 3). The displacements of A are given with respect to fixed axes x, y and of B with respect to axes x', y' at an angle α to x, y.

$$\left.\begin{aligned} u_A&=\phi_1(t, x, y), \\ v_A&=\phi_2(t, x, y), \end{aligned}\right\} \quad . \quad . \quad . \quad . \quad . \quad . \quad . \quad . \quad (9)$$

$$\left.\begin{aligned} U_B&=\psi_1(t, x', y'), \\ V_B&=\psi_2(t, x', y'), \end{aligned}\right\} \quad . \quad . \quad . \quad . \quad . \quad . \quad . \quad . \quad (10)$$

where $x'=x\cos\alpha+y\sin\alpha$, $y'=y\cos\alpha-x\sin\alpha$. So that the B field displacements with respect to x, y axes are:

$$\left.\begin{aligned} u_B&=U_B\cos\alpha-V_B\sin\alpha, \\ v_B&=V_B\cos\alpha+U_B\sin\alpha. \end{aligned}\right\} \quad . \quad . \quad . \quad . \quad . \quad . \quad . \quad (11)$$

Now for a plate in which $\sigma_{zz}=0$:

$$\left.\begin{aligned}\sigma_{xx}&=\frac{4\mu(\lambda+\mu)}{\lambda+2\mu}\frac{\partial u}{\partial x}+\frac{2\mu\lambda}{\lambda+2\mu}\frac{\partial v}{\partial y},\\ \sigma_{yy}&=\frac{4\mu(\lambda+\mu)}{\lambda+2\mu}\frac{\partial v}{\partial y}+\frac{2\mu\lambda}{\lambda+2\mu}\frac{\partial u}{\partial x}\\ \text{and}\quad \sigma_{xy}&=\mu\left(\frac{\partial u}{\partial y}+\frac{\partial v}{\partial x}\right).\end{aligned}\right\} \quad . \quad . \quad . \quad (12)$$

Substituting these equations in (8) gives

$$\tau^2_{\max}=\mu^2\left\{\left(\frac{\partial u}{\partial x}-\frac{\partial v}{\partial y}\right)^2+\left(\frac{\partial u}{\partial y}+\frac{\partial v}{\partial x}\right)^2\right\}. \quad . \quad . \quad . \quad . \quad . \quad (13)$$

Hence for the A field alone, substituting (9) in (13)

$$\tau^2_{A_{\max}}=2\mu^2(\phi_1'^2+\phi_2'^2). \quad . \quad . \quad . \quad . \quad . \quad . \quad (14)$$

Similarly for the B field

$$\tau^2_{B_{\max}}=2\mu^2(\psi_1'^2+\psi_2'^2). \quad . \quad . \quad . \quad . \quad . \quad . \quad (15)$$

For the combined field of A and B

$$u=u_A+u_B \quad \text{and} \quad v=v_A+v_B$$

$$\begin{aligned}\therefore\ \tau^2_{\max}=\mu^2\ &\{[\phi_1'-\phi_2'+\psi_1'(\cos 2\alpha-\sin 2\alpha)-\psi_2'(\cos 2\alpha+\sin 2\alpha)]^2\\ &+[\phi_1'+\phi_2'+\psi_1'(\cos 2\alpha+\sin 2\alpha)+\psi_2'(\cos 2\alpha-\sin 2\alpha)]^2\}\\ =2\mu^2&(\phi_1'^2+\phi_2'^2+\psi_1'^2+\psi_2'^2)+4(\phi_1'\psi_1'+\phi_2'\psi_2')\cos 2\alpha\\ &+4(\phi_2'\psi_1'-\phi_1'\psi_2')\sin 2\alpha. \quad . \quad . \quad . \quad . \quad . \quad . \quad . \quad . \quad . \quad (16)\end{aligned}$$

The specific problem under consideration is a plane dilatation pulse superimposed on a plane distortion pulse. This may be represented assuming B to be the dilatation pulse P of fig. 1 and A the distortional pulse, S, so that

$$u_A=0,\quad v_A=-\phi_2(c_1t+x) \quad \text{and} \quad U_B=-\psi_1(c_2t+x'),\quad V_B=0,$$

so that $\phi_1=\psi_2=0$ and eqn. (16) becomes

$$\tau^2_{\max}=2\mu^2(\phi_2'^2+\psi_1'^2)+4\mu^2\phi_2'\psi_1'\sin 2\alpha$$

which from (14) and (15)

$$\tau^2_{\max}=\tau^2_{A_{\max}}+\tau^2_{B_{\max}}+2\tau_{A_{\max}}\tau_{B_{\max}}\sin 2\alpha. \quad . \quad . \quad (17)$$

This gives the relation between the shear stresses of the individual P_1 and S pulses and the shear stress obtained when these pulses are superimposed at an arbitrary angle.

§ 5. Experimental

The experimental arrangement is basically a Cranz–Schardin type of multiple spark camera (Cranz and Schardin 1929). It is capable of taking a series of nine successive pictures at intervals which can be varied from 5 to 50 microseconds with a photographic exposure time of the order of one microsecond. The optical arrangement of the system is shown in

fig. 4 ; there are nine spark gaps and nine camera lenses, of which three of each are shown respectively as $S_{1\ldots3}$ and $L_{1\ldots3}$. The condenser lens C focusses an image of each spark gap on to one camera lens and the camera lenses produce images of the object O on the plate P. Thus when, say, spark S_1 flashes, the object, which is transparent, is illuminated in such a way that light transmitted by it passes through the lens L_3 only and an image of O is recorded behind this lens on plate P. Thus it is possible to take nine separate photographs at rates between 20 000 and 200 000 frames per second on the plate P (Christie 1952).

Fig. 4

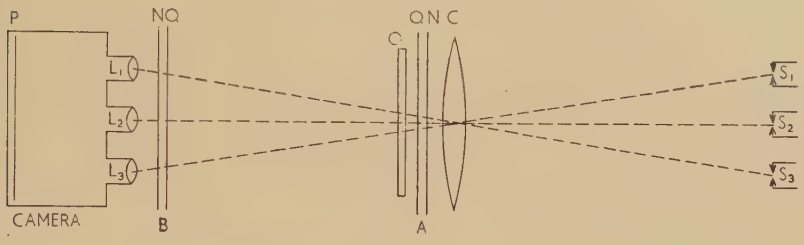

P=Photographic plate
$L_{1,2,3}$=Camera lenses
C=Condenser lens
Q=Quarter-wave plate
N=Polaroid screens
O=Test object
$S_{1,2,3}$=Spark sources

The specimens for these experiments were cut from thin sheets of unplasticized ' Perspex ' to the shape shown in fig. 5. To generate plane fronted pulses in the sheet, a length of ' Cortex ' detonating fuse was laid along the edge AB and detonated at A. This gives an explosive pulse

Fig. 5

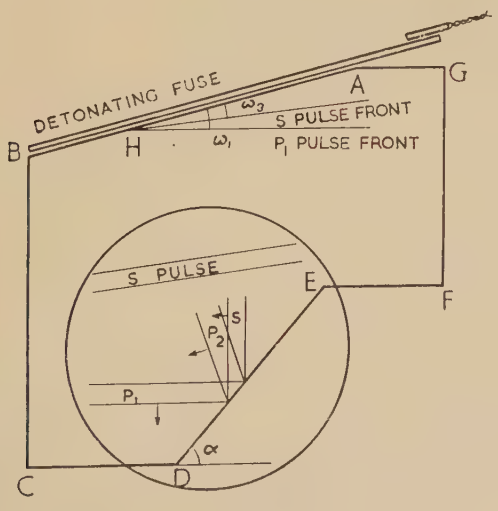

travelling at constant velocity, s, from A to B which in turn produces a plane stress pulse in the plate at an angle ω where

$$\sin \omega = \text{stress pulse velocity/explosive pulse velocity.}$$

This method generates both plane dilatation and distortion pulses. The upper part of fig. 5 shows the positions of the two pulse fronts when the detonation front reaches H ; the angles are given by

$$\sin \omega_1 = c_1/s \quad \text{and} \quad \sin \omega_2 = c_2/s.$$

To produce the S pulse it is necessary to shear the material along the direction of the pulse front. Since the component of the normal force applied by the explosive to the edge of the sheet is small in this direction, the amplitude of this pulse is small.

The field of view of the camera was arranged as shown by the circle, so that the reflection of the pulse from the edge DE could be observed. The angle of incidence was changed by cutting the specimens with different values for the angle α. The shape of the specimen was such that only the central portion of the initial pulse was used, the part of the specimen AGFE traps one end of the pulse and edge BC is sufficiently far away for reflections from it to be ignored.

For ease of interpretation of the results, it is desirable that a pulse once generated should travel through the plate without change of shape. It is therefore necessary that the material of the specimen should be non-dispersive. This means that the mechanical losses should be independent of frequency over the range used in the experiments. It was found that 'Perspex' satisfied these conditions, it being possible to propagate a pulse of about five microseconds duration without appreciable change of shape.

It is further necessary that the pulse should be long compared with the thickness of the plate ; it will then travel under plane stress conditions with a velocity of $[4\mu(\lambda+\mu)/\rho(\lambda+2\mu)]^{1/2}$. This velocity is the asymptotic value of the velocity of elastic waves in a plate when the wavelength is large compared with the thickness of the plate (Lamb 1917). For short waves the velocity is lower and approaches the value for Rayleigh waves. Considering the Fourier components of a pulse whose length is comparable with the thickness of the plate, the higher frequency components will travel faster than the lower frequency components, with a consequent change in pulse shape. To check experimentally that the asymptotic plane stress condition was applicable, tests were carried out on different plates having a range of thicknesses from 1/25 in. to 1/4 in., and no change of shape of the pulse or change of velocity was observed.

§ 6. Results

The pulses that can be seen when the incident P_1 pulse has travelled down the plate have been drawn within the circle of view in fig. 5. The right hand edge of the pulse has been reflected, generating the dilatation pulse P_2 and the distortion pulse S. The directions of travel of the P_1 and P_2 pulses, as shown by the arrows, both make an angle α with the

normal to the reflecting edge DE and the corresponding angle for the S pulse is β (cf. eqns. (2) and (3)). The S pulse generated by the detonating fuse will at this time have reached the upper part of the field of view. It has nothing to do with the reflection phenomenon under investigation but is included in the sketch to enable it to be identified in the photographs and separated from the other pulses.

Plate 8 shows the effects described when the angle of incidence is 30°. The scale on the left hand side is divided into 1 cm intervals and the times shown under the photographs in this and all other plates are measured from an arbitrary zero. In pictures 1 and 2 the pulse is travelling freely down the plate, in 3 reflection has just begun and in 5 and 6 the reflected pulses are clearly visible. The left hand one is the faster P pulse and the right the S pulse. The sharp dark areas in the later pictures are fractures produced by the passage of the stress pulses.

Plate 9 consists of eight pictures from eight different experiments showing how the intensity of the reflected pulses, as given by the fringes, varies with angle of incidence. It is this variation which is used to plot the points given in fig. 2, and other results not shown in the plates are also included. The full curves of fig. 2 are plots of $-(A_2/A_1)$ and (A_3/A_1) against α as given by eqns. (4) and (5), the experimentally determined value of $c_1/c_2 = 1{\cdot}76$ being used in eqns. (3) to obtain the relation between α and β.

Fig. 6

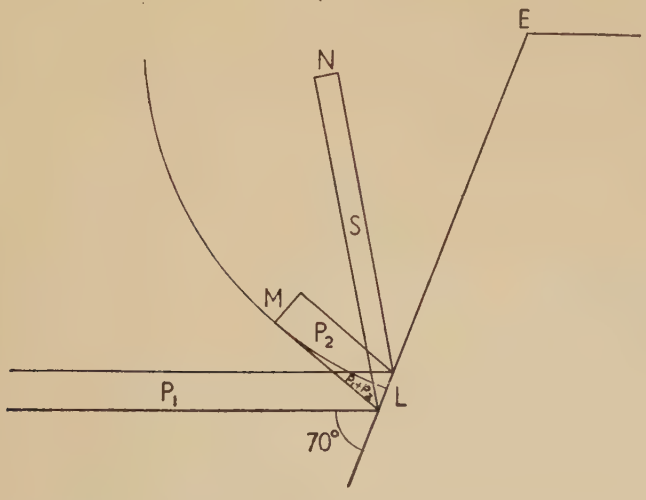

It is necessary to consider carefully the interpretation of the experimental results. The classical reflection theory applies to the steady state conditions when the incident pulse is infinite in extent and is reflected from an infinitely long boundary. Because of the finite size of the specimen there will be a transient effect at the commencement of the reflection when the incident pulse strikes the corner E, fig. 5. This effect is in the nature of a diffraction phenomenon. Figure 6 is a sketch approximately to scale, of the reflection of a pulse at 70° incidence after it has travelled

10 cm from the corner E, in time say t. Ideally, ignoring the transient effects at E, the reflected pulses will have the widths shown by LM and LN; LM goes to zero as the angle of incidence approaches 90°. Since the highest velocity of a wave in the plate is c_1, then the limit of the diffraction effects due to E will be a circle centre E and radius $c_1 t$. This circle is tangential to the front of the P_2 pulse as shown in the sketch. When the pulse has travelled far enough along the boundary, the reflection at L will be completely outside the circle. For angles of incidence less than about 70°, the incident P_1 pulse is completely beyond the circle for the later stages of the reflection shown in the photographs.

The reflected S pulse is superposed on the tail of the incident P_1 pulse, the reflected P_2 pulse and any transient effect from E. The latter can be expected to be small since in this case it will originate from the small amplitude tail of the P_1 pulse. The fringe count of the S pulse should be corrected for the former two effects.

From the photographs, the tail of the P_1 pulse would appear to be about $\frac{1}{2}$ fringe, but due to the photographic distortion of the half tones, resulting in a rapid transition from black to white, it may be as little as $\frac{1}{8}$ fringe. Taking the amplitude as $\frac{1}{2}$ fringe and substituting in eqn. (17), the corrected value of the S pulse can be found. Similarly, since A_3/A_1 is known, theoretically a correction for the tail of the P_2 pulse can also be calculated. The total of the two varies from $+\frac{1}{2}$ to $-\frac{1}{2}$ fringe. These are the maximum corrections and if the amplitude of the tail of the P_1 pulse is less than $\frac{1}{2}$ fringe, the corrections will be smaller. It is therefore doubtful if there is any gain in accuracy in correcting the fringe count of the S pulse in this way, since it can only be measured to $\frac{1}{2}$ fringe in the photographs. Thus there will be an error of $\pm 15\%$ in the measured value of the pulse amplitudes.

Referring to fig. 6, measurements can in theory be taken in the regions marked P_1, P_2, S and (P_1+P_2). For angles of less than 70° this latter region is too small to be of practical value. The incident pulse was always produced in the same way and the pictures show that there is no observable difference in different experiments. It was therefore assumed that m_1 of eqn. (7) was constant and it was considered more accurate to plot $A_3/A_1 = B(c_2/c_1)\, m_3$ where the constant B was found by fitting the experimental points at the maximum to the theoretical curve. These points are shown as diagonal crosses in fig. 2; the points in the circles are a plot of $A_2/A_1 = Bm_2$. The experimental values of A_3/A_1 are continued from 70° up to 88°, but for these angles it is also possible to obtain an estimate of the fringe count in the area marked P_1+P_2 in fig. 6. These measured values of $A_3/|A_1+A_2|$ are plotted as horizontal crosses in fig. 2, and the theoretical value is drawn in as a dotted curve for comparison.

At glancing incidence, as pointed out by Roesler (1954), A_1 cannot be observed and the experimental point shown is the measured value of $A_3/(A_1+A_2)$. (A_1+A_2) was measured as near the reflecting edge as possible so as to be within the diffraction circle and hence allow for

the reaction of the boundary back on the incident pulse. This effect will also be present for reflections at angles at less than 90°, but by making the reflecting edge long enough it is possible to make the diffraction circle lie behind the incident pulse.

It can be seen that the experimental points are in general agreement with the curves. At glancing incidence the value obtained for $A_3/(A_1+A_2)$ is low, but the theoretical value represents the behaviour when the incident pulse has travelled an infinit edistance along the reflecting edge. Plate 10 shows that the pulse has only travelled a short distance along the reflecting edge and therefore the experiments correspond to a transient condition, and it is possible that the steady state condition may not be reached until the incident pulse has travelled a considerable distance along the reflecting edge. The amplitude of the reflected wave would then be expected to approach asymptotically the value predicted by the theory. A further difficulty is that the value of $(A_3/|A_1+A_2|)_{\alpha=90}$ is very sensitive to the variations in the elastic properties of the material. A graph of its value in terms of the observable variable $\beta_{90}=\sin^{-1}(c_2/c_1)$ is shown in fig. 7. Accurate measurements of either β_{90} or c_2/c_1 are difficult and the values obtained are $\beta_{90}=34\frac{1}{2}°\pm1°$, so that there is a possible error in $(A_3/|A_1+A_2|)_{\alpha=90}$ of $\pm0{\cdot}1$.

Fig. 7

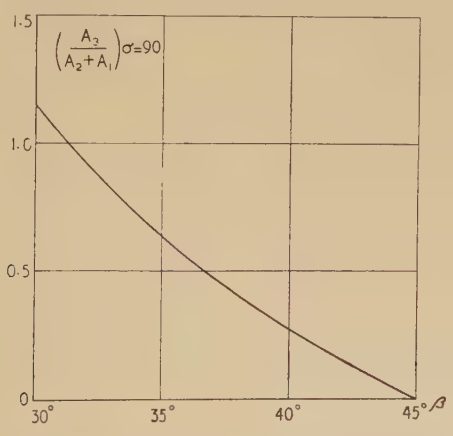

There is, however, a further aspect of the glancing incidence theory which can be verified experimentally. Roesler has shown that the boundary reacts back on the incident pulse in such a way as to cause the principal stresses of the pulse to turn through a small angle θ.

The directions of the principal stresses can be determined experimentally by using plane polarized light. With polarizer and analysers crossed, the intensity of the light in the fringe pattern is then modulated by a term equal to $\sin^2 2\delta$ where δ is the angle between the plane of polarization and the maximum stress. Hence whenever the plane of polarization is in the direction of either of the principal stresses. i.e., when $\delta=n(\pi/2)$, there is complete extinction irrespective of the absolute value of the stresses.

Plate 11 shows a plane pulse, produced as usual with detonating fuse, reflected at glancing incidence from both sides of a thin slit cut in the plate. The plane of polarization is 8° to the slit. Since the fastest rate at which a disturbance will propagate in the plate is the velocity of the P pulse, the only part of the incident pulse which can have been affected by the slit will be contained in a circle, centre the end of the slit and radius equal to the distance travelled by the P pulse down the slit. White circles have been drawn on the photographs to show this area.

Outside the circle the pulse should be unchanged, inside the directions of the principal stresses should be rotated. In the photographs shown, the rotation occurring due to reflection from the right of the slit is towards the plane of polarization and on the left of the slit away from the plane of polarization. Hence blackout occurs within the circle on the right and there is a slight intensification on the left ; the latter is not so marked, and more difficult to see in the photograph.

To determine the angle of rotation a set of experiments of the type shown in Plate 11 were carried out ; a different angle of polarization was used for each. The angle for which maximum blackout was obtained was 8°. It was not possible, however, to determine this angle to an accuracy greater than 2°. This was partly due to the fact that for smaller angles there was a tendency to black out the whole of the incident pulse outside the circle. Further, the rotation within the circle is probably not of constant value, since there must be a transition from 0° rotation outside the circle to about 8° inside.

Fig. 8

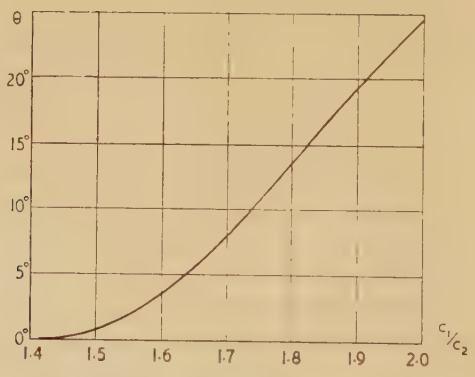

The variation of the rotation with c_1/c_2, as given by Roesler, is plotted in fig. 8. The extreme limits of c_1/c_2 are $\sqrt{2} \leqslant c_1/c_2 \leqslant 2$ for waves in a plate. For $c_1/c_2 = 1{\cdot}76$ the rotation is 11°, which is to be compared with the observed value of 8°. A lower value of the rotation would be expected since it can be assumed, as for the low value of the amplitude, that the pulse has not travelled sufficiently far along the reflecting edge to enable the asymptotic value to be reached. The observed blackout zone is thus still a transition stage from the state of no rotation to the steady state of maximum rotation.

§ 7. Conclusions

The accuracy of the experiments was limited, due to the superposition of several waves and to the fact that the pulse amplitudes could only be obtained to the nearest half fringe. However, to a first approximation the results indicated that the classical expressions for the reflection of elastic waves from a free boundary agree with experiment, provided care is taken in defining the observed variables, particularly towards glancing incidence. The glancing incidence experiments are not strictly comparable with the theory, but it would appear likely that a better agreement would be obtained if the pulse was allowed to travel a much further distance along the reflecting edge.

Acknowledgments

The author wishes to express his thanks to Dr. H. Kolsky and Dr. F. C. Roesler for help and advice in many discussions during this work, and to Miss C. J. Culf and Mr. D. J. Farthing for their assistance with the experimental work.

References

Bishop, R. E. D., 1953, *Quart. J. Mech. and Appl. Math.*, **6**, 250.
Chree, C., 1889, *Trans. Camb. Phil. Soc.*, **14**, 250.
Christie, D. G., 1952, *Trans. Soc. Glass Tech.*, **36**, 74.
Coker, E. G., and Filon, L. N. G., 1931, *Treatise on Photoelasticity* (Cambridge : University Press).
Cranz, C., and Schardin, H., 1929, *Zeits. f. Phys.*, **56**, 147.
Davies, R. M., 1948, *Phil. Trans.* A, **240**, 375.
Goodier, J. N., and Bishop, R. E. D., 1952, *J. Appl. Phys.*, **23**, 124.
Kolsky, H., 1953, *Stress Waves in Solids* (Oxford : Clarendon Press) ; 1954, *Phil. Mag.*, **45**, 712.
Lamb, H., 1917, *Proc. Roy. Soc.* A, **93**, 114.
Love, A. E. H., 1927, *The Mathematical Theory of Elasticity*, 4th edition, (Cambridge : University Press).
Prescott, J., 1942, *Phil. Mag.*, **33**, 703.
Rayleigh, 1889, *Lond. Math. Soc. Proc.*, **20**, 225.
Roesler, F. C., 1955, *Phil. Mag.*, **46**, 517.
Schardin, H., 1950, *Glastechn. Ber.*, **23**, 1, 67, 325.

LXIII. *On the Optical Model for Nucleon Scattering by Oxygen*

By Y. Fujimoto* and A. Hossain
H. H. Wills Physical Laboratory, University of Bristol†

[Received February 4, 1955]

In a recent paper, Feshbach, Porter and Weisskopf (1954) have explained the total cross section for the scattering of neutrons by nuclei, by an average potential $V(r)=-(42+i1{\cdot}3)$ Mev for the neutron within the nucleus.

We have tried to explain the angular distribution of 9·5 Mev protons elastically scattered by oxygen by making a similar approach. We have made calculations, varying both the nuclear radius, and the parameters of the complex potential, $V=-(V_0+iW_0)$, where W_0 gives the absorption potential. For the radius, we have chosen the value $R=1{\cdot}45\times10^{-13}$ cm; a lower value gave much too flat an angular distribution, and a higher value, too great a differential cross section. Having thus fixed the value of R, we calculated the angular distribution for different values of V_0. We thus found that in varying V_0 from 20 to 42 Mev, the position of the first interference minimum moves from $\phi=75°$ to 55°, where ϕ is the angle of scattering in the centre-of-mass system of the collision. Values of V_0 between 30 and 36 Mev gave the first minimum at angles between 65° and 70°. The same potential values gave the position of the maximum at $\phi=110°$.

The experimental angular distribution has been determined by Burcham, Gibson, Hossain and Rotblat (1952). For comparison with calculation, we have taken their results together with certain additions and modifications by the same authors and reported to us privately. By varying the parameters, we have found the values giving the best agreement with the experimental results, choosing as the condition of 'best-fit' (*a*) the correct position of the first interference minimum at $\phi=65°$, and (*b*) both the correct position, and the magnitude of the differential cross section of the first maximum at $\phi=110°$. These conditions are found to demand that V_0 shall be between 30 and 36 Mev, together with a suitable value of W_0. It may be significant that the amplitude of the f-wave of the incoming protons was the determining factor in fitting the experimental angular distribution. Figure 1 shows the angular distribution for two values of the potential V_0, and with proper adjustment of W_0, to give the best fit. The curve for $V_0=42$ Mev is also included and may be seen to give a rather poor fit.

We have also calculated the angular distribution of 14·1 Mev neutrons elastically scattered by oxygen, assuming, again, potentials between 20

---

* On leave of absence from the University of Kyoto, Japan.
† Communicated by Professor C. F. Powell, F.R.S.

and 42 MEV. This time our criterion for best fit was the value of the total cross section which is 1·6 barn for this energy (Conner 1953) A potential value V_0 of 20 MEV, with any adjustment of W_0, gave too high a value of the total cross section, whilst a similar analysis with $V_0=42$ MEV gave too low a value. Again values of V_0 between 30 and 36 MEV gave the correct value of the cross section, given proper adjustment of W_0. The results are given in fig. 2, and show that both $V=(32+i7)$ MEV and $V=-(36+i5)$ MEV give a satisfactory fit to the experimental points. For comparison, the theoretical curve for $V=-(42+i5)$ MEV is shown in the same figure.

Fig. 1

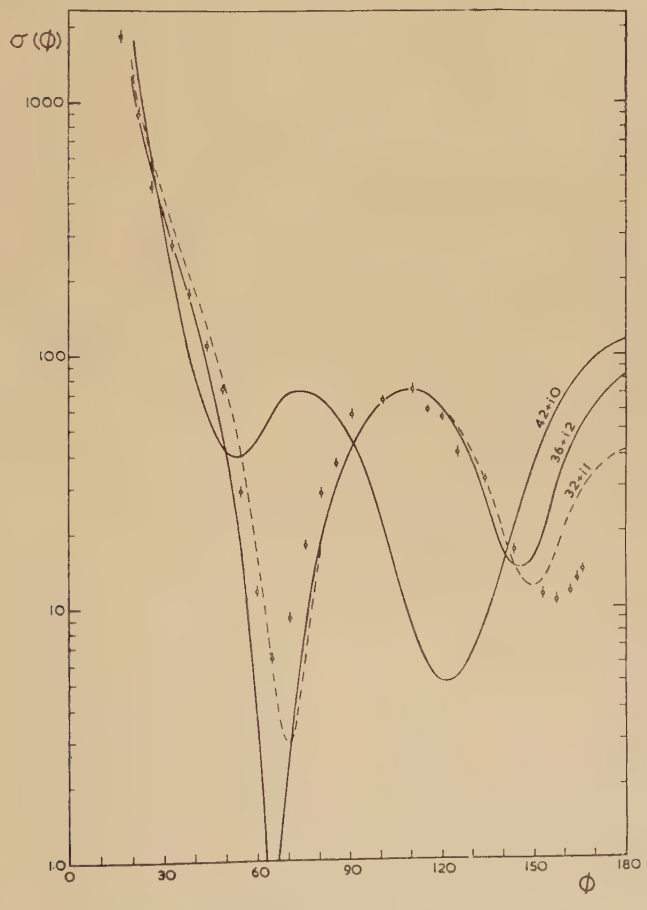

Angular distribution in the centre-of-mass system of 9·5 MEV protons elastically scattered by oxygen (Burcham *et al.* 1953, and private communication); $\sigma(\phi)$ is given in millibarn per steradian. The full curves are those given by the potential $V=-(42+i0)$ MEV and $-(36+i2)$ MEV, and the dashed curve is that given by the potential $V=-(32+i1)$ MEV. In both cases, $R=1{\cdot}45\times10^{-13}A^{1/3}$ cm.

Our values for the potential V_0 can also be compared with that obtained from slow neutron scattering. For this purpose, we have calculated the potential value which will explain the 2s resonance level of ^{17}O. Our chosen value of the radius, R, gave $V_0=42$ MEV, in agreement with the results of slow neutron scattering (Adair 1953, Ford and Bohm 1950). This suggests that the effective depth of the potential well is lowered as the incident energy of the neutron increased.

There is also an indication that the mean-free-path of a nucleon in the

Fig. 2

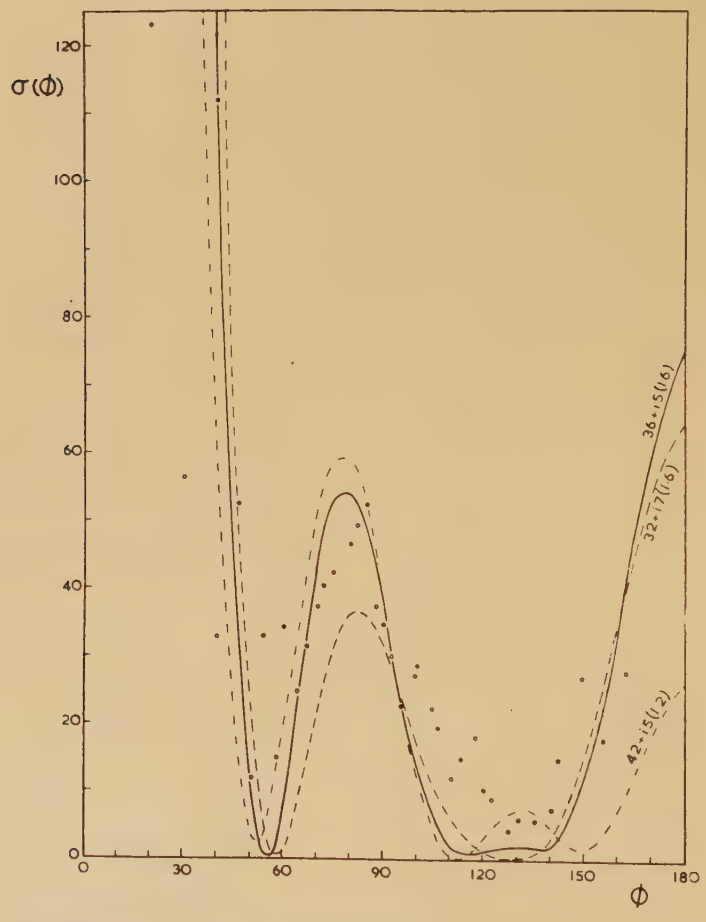

Angular distribution in the centre-of-mass system of 14·1 MEV neutrons elastically scattered by oxygen. $\sigma(\phi)$ is given in millibarns per steradian. The experimental points marked ○ and ● are taken from the article by Conner (1953). (The difference between the two sets of points is explained in the article. The absolute cross section has been adjusted to fit the curves.) The three theoretical curves are as shown in the figure. The figures in brackets give values of the total cross section in barns, for those potential values.

nucleus decreases as its energy increases from 9·5 Mev to 14 Mev assuming charge independence of nuclear forces. Further, recent results on the angular distribution of 18 Mev protons elastically scattered by elements of medium and high atomic weight (Chase and Rohrlich 1954), and on the scattering of 90 Mev neutron (Fernbach, Serber and Taylor 1949), taken with our own results, suggest that the mean-free-path of a nucleon in nuclear matter decreases with energy up to 18 Mev, and possibly beyond, and then, at some energy between 18 and 90 Mev, it begins to increase.

A more detailed account of the calculations and their extension to other target nuclei, will be published later.

We are indebted to Professor M. H. L. Pryce and Dr. D. J. Prowse for many helpful discussions during the course of the work, and to Professor C. F. Powell for his interest and encouragement. We are also very grateful to Dr. E. J. Burge for assisting us with various calculations.

References

Adair, R. K., 1954, *Phys. Rev.*, **94,** 737.
Burcham, W. E., Gibson, W. M., Hossain, A., and Rotblat, J., 1953, *Phys. Rev.*, **92,** 1266 and private communication.
Chase, D. M., and Rohrlich, M., 1954, *Phys. Rev.*, **94,** 81.
Conner, J. P., 1953, *Phys. Rev.*, **89,** 712.
Fernbach, S., Serber, R., and Taylor, T. B., 1949, *Phys. Rev.*, **75,** 1352.
Feshbach, H., Porter, C. E., and Weisskopf, V. F., 1954, *Phys. Rev.*, **96,** 448.
Ford, K. W., and Bohm, D., 1950, *Phys. Rev.*, **79,** 745.

LXIV. *Non-linear Dissipative Processes in Liquid Helium II*

By H. E. Hall and W. F. Vinen
The Royal Society Mond Laboratory, Cambridge*

[Received April 1, 1955]

As a consequence of an extended investigation of non-linear dissipative processes in liquid helium II by means of thermal and mechanical experiments, we have been led to examine the propagation of second sound in uniformly rotating helium, and have found an attenuation proportional to the angular velocity. Lane, Wheeler and Blakewood (1955) have performed what appears to be a similar experiment, and this prompts us to publish a preliminary note of our work at the present time.

An investigation has been made (W. F. V.) of the behaviour of the temperature difference between the ends of a tube of 6 mm $\times$ 2 mm cross section when a heat current suddenly starts to flow down it. No measureable temperature difference appears for a time of order 1 sec after the heat current is switched on, and then a temperature difference given by the mutual friction of Gorter and Mellink (1949) builds up ; this delay time decreases as the heat current is increased. If a second sound resonance is established across the tube the second sound suffers a linear attenuation in a steady heat current. This attenuation appears after the same delay time as is involved in establishing the temperature difference ; it is proportional to the square of the heat current and is given by a modified Gorter–Mellink force of the form $A\rho_s\rho_n \mathbf{V}^2 \mathbf{v}$, where $\mathbf{V}$ is the time average of the vector relative velocity of the two fluids and $\mathbf{v}$ is the instantaneous relative velocity. The velocity of the second sound is not measureably changed. It is further found that when the heat current is switched off the helium takes about 4 min to recover its initial undisturbed state completely. The delay time effects associated with mutual friction and this very slow recovery are strikingly similar to the growth and decay of turbulence in an ordinary liquid, suggesting that at sufficiently high velocities laminar superflow becomes unstable and breaks up into turbulence ; and the form of the observed second sound attenuation implies that mutual friction is a property of this turbulent state. It may therefore be a property of any non-irrotational state.

Further evidence for this idea is provided by experiments (H. E. H.) on the angular acceleration and retardation of the superfluid. A can filled with closely spaced discs, so that the normal fluid is tightly coupled to it, is rotated uniformly until the helium is in equilibrium with it. The can is then suddenly brought to rest and the torque exerted on it by the liquid is measured as a function of time. Even at angular velocities of only 0·1 rad sec^{-1} the amount of angular momentum collected indicates

* Communicated by D. Shoenberg, F.R.S.

that the equilibrium state of the superfluid is rotation with the containing vessel. The force exerted on the superfluid is found to be greater than the Gorter–Mellink friction. Also the variation of torque with time is different for the acceleration and retardation processes, implying that absolute angular velocity is an important parameter. Detailed examination of the results suggests the possibility of a mutual force between the two fluids of the form $B(\rho_s\rho_n/\rho)\,|\omega|\,(\mathbf{v}_s-\mathbf{v}_n)$, where ω is the angular velocity in an inertial coordinate system either of the superfluid or of the liquid as a whole, and B is a dimensionless constant having the value $6{\cdot}3\pm0{\cdot}5$ at $1{\cdot}27^\circ$K. It thus appears that macroscopic rotation is also effective in producing mutual friction.

If mutual friction is a general property of rotational flow, as both these investigations suggest, there should be an attenuation of second sound in uniformly rotating helium II, and such an effect has been observed with a resonance technique. The complete resonator, including heater and thermometer, is rotated. A small gap at the temperature node allows the mean heat input to escape to a further volume of rotating helium, whose only connection with stationary helium is via vapour and the film. Most of the measurements have been made with a resonator using a radial mode of propagation ; for such a mode Coriolis forces will cause an extra viscous attenuation, but this effect should be only of the order of the square of the ratio of the frequency of rotation to the frequency of the second sound, about 1 part in 10^6. When the resonator is rotated, the amplitude of the second sound resonance at first falls considerably and then rises, attaining a steady value less than the initial value after about 1 min. When rotation is stopped the amplitude again falls steeply at first, but rises to its initial value after about 5 min. A moderate amount of mechanical vibration does not produce any extra attenuation, but shaking the cryostat to and fro does. This effect and the transient effects on starting and stopping are attributed to the formation of eddies. The attenuation produced by rotation is linear and accurately proportional to the angular velocity up to 1·2 rev. sec^{-1}; the velocity is not changed by more than 0·1%. Interpretation in terms of the force $B(\rho_s\rho_n/\rho)\,|\omega|\,(\mathbf{v}_s-\mathbf{v}_n)$ gives values of B varying from $1{\cdot}52\pm0{\cdot}05$ at $1{\cdot}3^\circ$K to $0{\cdot}80\pm0{\cdot}05$ at $2{\cdot}0^\circ$K.

A single experiment has been made with an axial mode resonator, using the same direction of second sound propagation as Lane *et al.* (1955); however, we have insufficient information about their experiment to compare results. For this mode we obtain an apparent value of B of $0{\cdot}15\pm0{\cdot}15$ at $1{\cdot}28^\circ$K, which is much less than for the radial mode. The accuracy is low because the Q of the resonator used so far is low, probably because the design permits radiation of second sound from it. The true value of B may be greater, for it is just possible that the rotation causes sufficient dissipation in a narrow gap to reduce the radiation loss appreciably.

We have also seen above that if the interpretation of the angular acceleration experiments in terms of the force $B(\rho_s\rho_n/\rho)\,|\omega|\,(\mathbf{v}_s-\mathbf{v}_n)$ is

accepted, we obtain $B=6{\cdot}3\pm0{\cdot}5$ at $1{\cdot}27^{\circ}$K, which is much greater than the value from second sound measurements. The acceleration experiment is less direct than the second sound measurements, and consequently the interpretation is more doubtful ; however, it should be noted that in the three experiments giving discordant values of B the relative velocity $(\mathbf{v}_s-\mathbf{v}_n)$ is directed in the three different directions that exist in a rotating coordinate system.

It therefore seems probable that we have assumed too simple a relation between rotation and mutual friction. Thus B may be anisotropic, with different values for the three principal directions, and it may depend on the radius of the vessel. Also the precise meaning of ω is uncertain, as can be seen by considering three possible classes of rotation : circulation with non-vanishing curl $\mathbf{v}_s$ everywhere ; circulation with curl $\mathbf{v}_s=0$ except on vortex sheets dividing regions of different circulation (London 1954) ; and curl-free circulation in a multiply connected region. No experiments have yet been done to see whether mutual friction is present in the third case ; nor do we know whether macroscopic uniform rotation belongs to the first or second class. Therefore we cannot yet say whether it is a non-zero value of curl $\mathbf{v}_s$ or a non-zero value of the circulation that is responsible for mutual friction. Experiments are now in progress to investigate further the relationship between rotation and mutual friction.

In the experiments on second sound in rotating helium the only parameter that has been changed is the angular velocity ; there are no steady relative velocities, for it has been shown that the superfluid rotates with the containing vessel. The existence of an attenuation therefore strongly supports the general conclusion that mutual friction is a property of rotational states of the superfluid, and only of such states.

We are grateful to Dr. D. V. Osborne and Dr. A. B. Pippard for many helpful discussions, and to the Department of Scientific and Industrial Research for maintenance grants.

References

Gorter, C. J., and Mellink, J. H., 1949, *Physica*, **15**, 285.

Lane, C. T., Wheeler, R. G., and Blakewood, C. H., 1955, *Bull. Amer. Phys. Soc.*, **30**, 57.

London, F., 1954, *Superfluids*, Vol. II (New York : Wiley), p. 151.

LXV. *Diurnal and Seasonal Wind Variations in the Upper Atmosphere*

By J. S. Greenhow and E. L. Neufeld
Jodrell Bank Experimental Station, University of Manchester *

[Received December 23, 1954]

Abstract

The results of a years survey of the winds at altitudes of 80–100 km are described. The measurements were made using radio reflections from drifting meteor trails. The principal periodic wind in this region is semi-diurnal in character, and is approximately represented by a vector of amplitude 10-40 metres sec^{-1}, rotating in a clockwise direction. The phase of the rotation undergoes a marked variation during the autumn months, but for most of the year the wind is directed towards the North near 0600 and 1800 hours local time. A small diurnal periodic wind of amplitude 5–10 metres sec^{-1}, directed towards the North at 1130 hours, has also been resolved. Prevailing winds with components of magnitude 5–25 metres sec^{-1}, towards the East in summer and winter, and towards the West in spring and autumn are observed. Components towards South of similar amplitude are present during most of the year. Turbulent winds with r.m.s. velocities of 30 metres sec^{-1}, are almost always observed.

§ 1. Introduction

The study of radio reflections from drifting meteor trails has now proved to be an exceptionally powerful method for the investigation of upper atmosphere winds (Greenhow 1952, 1954, Manning, Villard and Peterson 1950, Elford and Robertson 1953). In an earlier paper (Greenhow 1954), a technique was described which enabled mean hourly wind speeds and directions at heights of 80–100 km to be determined throughout the day. Preliminary results showed that the method was able to resolve large periodic and prevailing wind components from a single days observations. Routine measurements have now been in progress for over a year, and the first fifteen months observations are presented below. As the technique and method of analysis have already been described in detail, these subjects are not discussed in the present paper.

§ 2. Results

(*a*) *Turbulent Wind Component*

The wind in the lower E-region is extremely turbulent. Radio echo studies of long duration meteor trails show that the wind velocities at points separated by only 5 km may differ by as much as 50 metres sec^{-1},

* Communicated by the Authors.

at times when the average wind velocity is only of this order (Greenhow 1952). Persistent meteor trails photographed at intervals of a few seconds show considerable distortion, and wind shears of the same order or even higher than those observed by radio methods have been recorded (Liller and Whipple 1954). Thus when wind observations are carried out during a short period of time, over a localized region of the sky, regular variations in velocity will be obscured by turbulent winds. In the present method over a 100 individual wind measurements are made each hour, the meteor trails responsible for the radio echoes are distributed over a region of sky approximately 200 km by 100 km in extent, and 10 km in depth. In this way the effects of large scale eddies are smoothed out, and the average hourly wind velocities throughout the day generally show regular periodic variations. Test experiments carried out by directing the aerial beam in diametrically opposite directions, show that the uniform wind components are essentially the same in regions 500 km apart.

Fig. 1

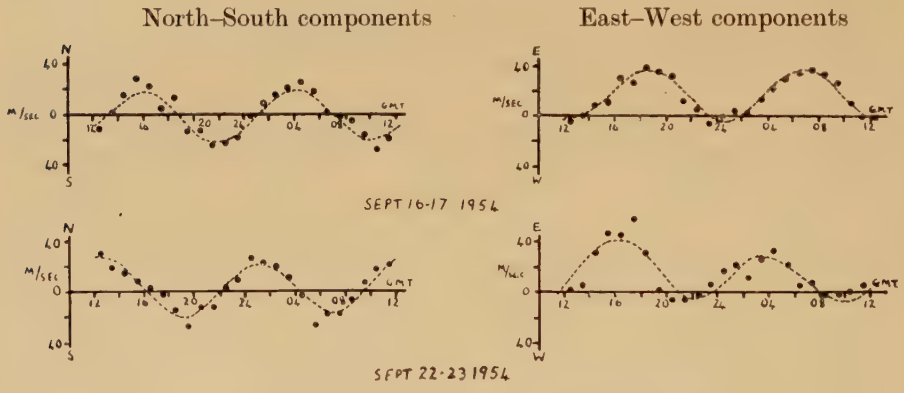

Components of wind velocity, September 1954.

Sept. 16–17 : $V_{NS} = -1{\cdot}4 + 1{\cdot}9 \sin 15(t - 0{\cdot}3) + 20{\cdot}5 \sin 30(t - 1{\cdot}1)$

$V_{EW} = +16{\cdot}0 + 1{\cdot}9 \sin 15(t - 6{\cdot}3) + 19{\cdot}8 \sin 30(t - 3{\cdot}7)$

Sept. 22–23 : $V_{NS} = +1{\cdot}9 + 4{\cdot}3 \sin 15(t - 6) + 22{\cdot}2 \sin 30(t + 2)$

$V_{EW} = +14{\cdot}3 + 8{\cdot}0 \sin 15(t - 11{\cdot}4) + 20{\cdot}8 \sin 30(t - 1{\cdot}1)$

In this paper we will be concerned only with the average hourly wind vectors. It must be remembered, however, that irregular winds with r.m.s. turbulent velocities of the order of 30 metres sec^{-1}, are almost always present.

(*b*) *The Semi-Diurnal Wind Component*

(i) *Qualitative Observations*

Observations have been carried out approximately two days each month between September 1953 and November 1954. Examples of the North–South and East–West mean hourly wind components for individual days are given in fig. 1. The points are unsmoothed. Winds towards the North and East are considered positive. On most days marked

semi-diurnal oscillations in the wind components are apparent. For example, in the 24 hour period from 1200 h local (Greenwich mean) time on September 16, 1954, to 1200 h September 17, 1954 maximum velocity towards the North occurs at approximately 1600 h, and again 12 hours later at 0400 h. The phase of the oscillation in the East–West direction is approximately 90° behind that in the North–South direction, maximum velocity towards the East occurring at 1900 and 0700 h. These components correspond to a wind vector rotating in a clockwise direction with a period of half a day. The amplitude of the vector is approximately 20 metres sec^{-1}.

Examination of the records for individual days shows that the amplitude and phase of the semi-diurnal wind components vary considerably. During the spring and summer months, for example, the amplitude is only about 10 metres sec^{-1}, and on March 17–18 (table 1) it is hardly resolvable in the North–South direction. These results will now be considered in greater detail.

(ii) *Harmonic Analysis of 24-hour Observations*

A harmonic analysis has been carried out for each days observations, taking a fundamental period of 1 day. The only other terms of the Fourier series included in the analysis are the second harmonic with a period of 12 hours—this is the semi-diurnal oscillation—and a constant term. The constant term is equivalent to a steady prevailing wind. This component is discussed in § 2 (*c*).

The results of the harmonic analysis for the 24 days are given in table 1. The broken curves in fig. 1 are the components V_{NS} and V_{EW}, representing the first three terms of the Fourier series. There is quite good agreement between the experimental points and the theoretical curves, showing that harmonics higher than the second are insignificant.

The semi-diurnal components from table 1 are shown on harmonic dials in fig. 2. An average point is given for each month from September 1953 to August 1954 so as not to confuse the diagrams, as records taken on successive days can show variations in phase of approximately half an hour. Figure 2 (*a*) shows the amplitude of the North–South component, and the time of maximum velocity towards the North. The variations in amplitude and phase of the semi-diurnal wind component are very marked. Between September and November 1953 the phase of the oscillation changes by almost 360°, the amplitude varying between 10 and 40 metres sec^{-1}. During the same period in 1954 an attempt was made to study this phase change in greater detail, by observing at intervals of a few days near the critical period. The results for individual days for September to November 1954 are shown by crosses in fig. 2. It can be seen that this remarkable change in phase of the semi-diurnal wind component is repeated in two successive years. A large part of the phase shift occurs over a time interval of only a few days. This is shown by the 24 hour component plots for September 16–17 and September 22–23, 1954, in fig. 1. On these days the semi-diurnal wind component,

Table 1. Results of Harmonic Analysis of North–South and East–West Wind Components for Individual Days

Amplitudes are in metres sec^{-1}. Movements towards North and East are considered positive

24 hour period	Prevailing V_{NS}=	Diurnal	Semi-Diurnal	Prevailing V_{EW}=	Diurnal	Semi-Diurnal
Sept. 7–8, 1953	− 2·5	− 6·9 sin 15(*t* − 6·5)	+31·0 sin 30(*t* − 1·6)	+21·2	+ 1·0 sin 15(*t* − 14·5)	+21·5 sin 30(*t* − 4·0)
Sept. 16–17, 1953	−12·3	+ 6·0 sin 15(*t* − 7·5)	+28·3 sin 30(*t* − 0·3)	+11·6	+ 7·0 sin 15(*t* − 12·2)	+14·2 sin 30(*t* − 3·4)
Sept. 17–18, 1953	−14·2	− 8·6 sin 15(*t* − 8·5)	+40·8 sin 30(*t* − 0·0)	+10·6	+ 4·5 sin 15(*t* − 9·4)	+19·6 sin 30(*t* − 3·4)
Oct. 16–17, 1953	+ 4·3	+13·0 sin 15(*t* − 8·7)	+ 15·1 sin 30(*t* − 7·8)	− 4·7	+14·8 sin 15(*t* − 11·5)	+13·4 sin 30(*t* − 11·3)
Oct. 17–18, 1953	0·0	−11·8 sin 15(*t* − 5·2)	+12·4 sin 30(*t* − 9·1)	− 8·1	+10·3 sin 15(*t* − 8·8)	+ 6·6 sin 30(*t* − 0·3)
Nov. 19–20, 1953	+ 9·8	− 5·4 sin 15(*t* + 3·0)	+32·9 sin 30(*t* − 2·5)	− 4·0	+ 7·3 sin 15(*t* + 0·0)	+29·4 sin 30(*t* − 5·8)
Dec. 17–18, 1953	− 5·4	−13·7 sin 15(*t* − 1·7)	+38·8 sin 30(*t* − 2·7)	+10·8	+22·7 sin 15(*t* − 11·3)	+25·9 sin 30(*t* − 5·1)
Dec. 18–19, 1953	+15·6	−15·1 sin 15(*t* + 3·0)	+40·2 sin 30(*t* − 4)	+22·7	+ 4·1 sin 15(*t* − 3·0)	+32·2 sin 30(*t* − 5·5)
Jan. 20–21, 1954	− 6·6	− 9·9 sin 15(*t* + 3·0)	+31·5 sin 30(*t* − 3·7)	+ 7·3	+10·2 sin 15(*t* − 1·7)	+19·4 sin 30(*t* − 6·6)
Jan. 28–29, 1954	− 1·0	+ 3·5 sin 15(*t* − 3·0)	+ 23·4 sin 30(*t* − 3·4)	+13·4	+ 5·2 sin 15(*t* + 1·2)	+21·0 sin 30(*t* − 6·4)
Feb. 10–11, 1954	+ 8·5	−13·1 sin 15(*t* − 0·9)	+ 29·8 sin 30(*t* − 4·0)	+16·7	+ 4·8 sin 15(*t* − 8·2)	+16·5 sin 30(*t* − 7·4)
Mar. 17–18, 1954	−11·8	− 2·3 sin 15(*t* + 6·2)	+ 5·4 sin 30(*t* − 3·7)	−11·1	+ 1·8 sin 15(*t* − 0·9)	+12·4 sin 30(*t* − 8·1)
Mar. 23–24, 1954	− 1·5	+18·0 sin 15(*t* − 10·8)	+ 26·7 sin 30(*t* − 0·7)	−24·2	+20·5 sin 15(*t* − 0·5)	+20·4 sin 30(*t* − 4·3)
Apr. 4–5, 1954	− 3·0	− 6·3 sin 15(*t* − 4·9)	+11·3 sin 30(*t* − 2·7)	+ 0·5	+10·0 sin 15(*t* + 9·2)	+12·1 sin 30(*t* − 4·4)
Apr. 14–15, 1954	−13·8	− 5·0 sin 15(*t* − 6·5)	+15·2 sin 30(*t* − 2·6)	−13·7	+ 8·5 sin 15(*t* + 10·3)	+10·9 sin 30(*t* − 5·3)
Apr. 22–23, 1954	−10·0	+14·4 sin 15(*t* − 6·3)	+11·2 sin 30(*t* − 3·8)	− 24·0	+ 5·0 sin 15(*t* − 10·2)	+ 5·5 sin 30(*t* − 6·5)
May 18–19, 1954	− 6·5	+ 4·0 sin 15(*t* − 11·8)	+ 8·2 sin 30(*t* − 4·7)	− 4·1	+ 5·0 sin 15(*t* − 11·3)	+11·2 sin 30(*t* − 8·1)
May 25–26, 1954	−14·0	+ 8·9 sin 15(*t* − 1·2)	+15·8 sin 30(*t* − 1·6)	+ 1·8	+14·7 sin 15(*t* − 2·3)	+10·3 sin 30(*t* − 7·3)
June 12–13, 1954	−19·6	+14·8 sin 15(*t* − 3·5)	+20·4 sin 30(*t* − 2·6)	+13·7	+12·0 sin 15(*t* + 5·8)	+ 6·5 sin 30(*t* − 8·2)
June 28–29, 1954	−19·7	+14·8 sin 15(*t* − 8·8)	+21·5 sin 30(*t* − 2·4)	+20·9	+ 7·6 sin 15(*t* + 6·4)	+ 6·9 sin 30(*t* − 4·8)
Jul. 11–12, 1954	−17·1	+20·2 sin 15(*t* − 5·1)	+ 13·2 sin 30(*t* − 2·9)	+15·7	+17·1 sin 15(*t* + 9·7)	+ 9·0 sin 30(*t* − 2·1)
Jul. 15–16, 1954	−12·4	+ 4·8 sin 15(*t* − 6·4)	+20·8 sin 30(*t* − 2·1)	+ 11·4	+ 4·7 sin 15(*t* − 11·4)	+12·1 sin 30(*t* − 1·9)
Aug. 17–18, 1954	− 9·3	+17·7 sin 15(*t* − 1·8)	+19·3 sin 30(*t* − 2·0)	+17·9	+14·0 sin 15(*t* + 7·7)	+18·5 sin 30(*t* − 4·2)
Aug. 19–20, 1954	−21·1	+20·3 sin 15(*t* − 4·5)	− 7·9 sin 30(*t* − 3·1)	+14·3	+23·1 sin 15(*t* + 10·2)	+ 9·0 sin 30(*t* − 3·7)

which had been rather small and irregular during the summer months, once again increased in amplitude and became very distinct. On each day the NS and EW components are very nearly three hours out of phase, corresponding to a regular rotation of the wind vector. Over this period of 6 days, however, the phase of the rotation clearly advances by approximately 90°, time of velocity towards the North changing from 4·1 to 1·0 h, and time of velocity towards the East from 6·7 to 4·1 h.

Fig. 2

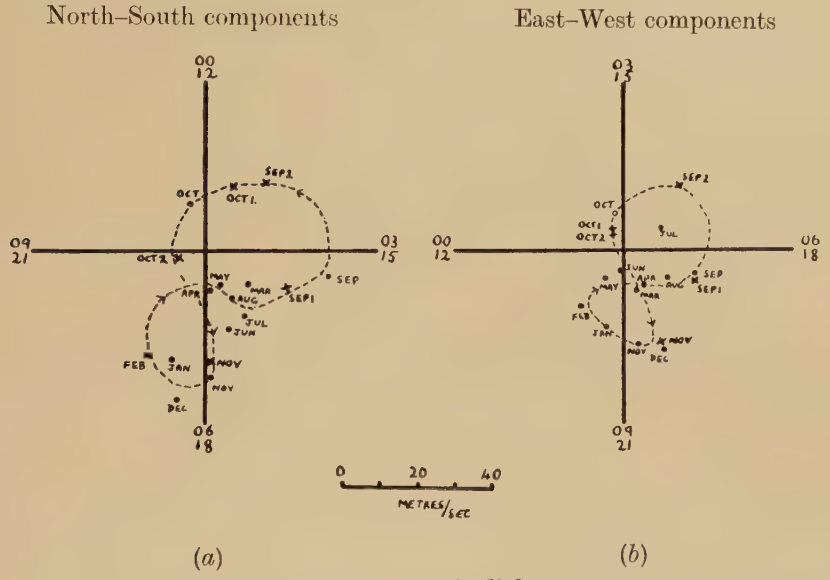

12-hour harmonic dials.

(*a*) North–South components. (*b*) East–West components. •12 months period, Sept. 1953 to Aug. 1954. ×Beginning of second 12 month period.

During the winter months, November to February, the 12 hour periodic wind is fairly stable, maximum velocity towards the North occurring near 0630 h with an amplitude of 30 metres sec^{-1}. The amplitude falls to approximately 10 metres sec^{-1} during the spring and summer months (March to August), although the time of maximum velocity towards the North does not change appreciably (~0530 h).

The behaviour of the East–West component is very similar to that of the North–South component, the phases being retarded by approximately 90° (3 hours). The East–West harmonic dial in fig. 2 (*b*) has been rotated through 90° to counterbalance this phase lag, and the broken curves in 2 (*a*) and (*b*) show the same general trends.

(iii) *Seasonal Averages of the Wind Components*

The points in the 12-hour harmonic dials representing the month to month variations of the semi-diurnal wind vector, show a number of distinct groupings. For example, the large components from November to February with similar amplitudes and phases form one group. The

much smaller components in the summer months also form a group. September and October appear to be exceptional, and are considered separately.

Fig. 3

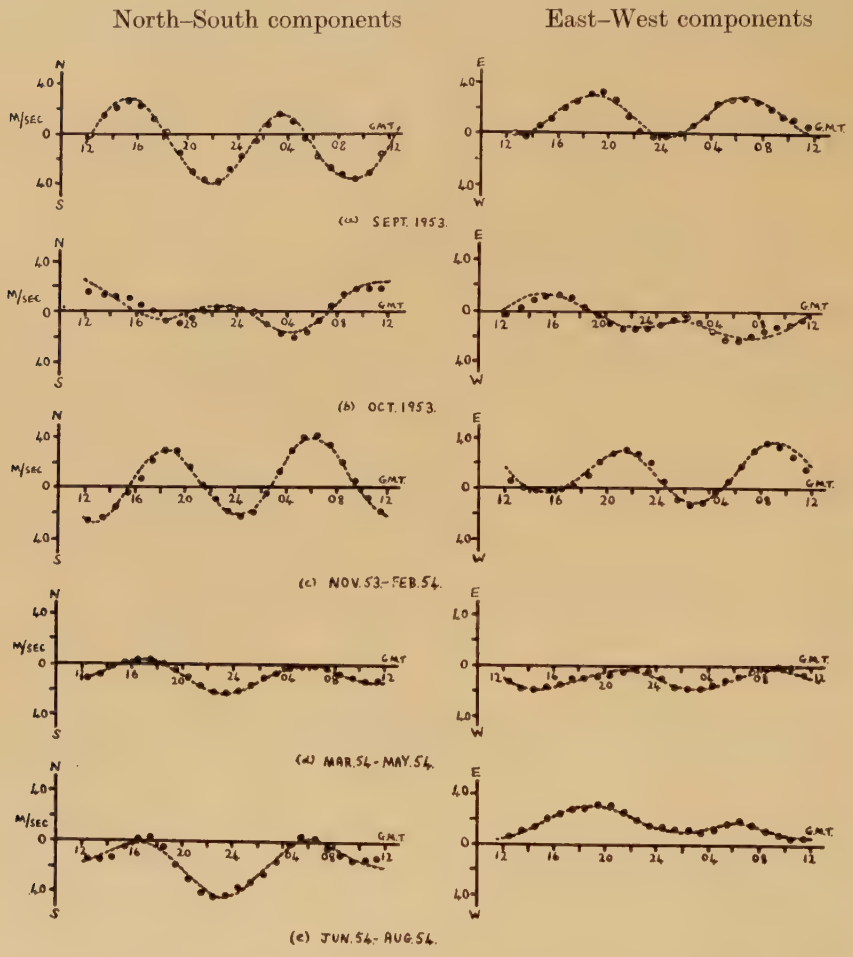

North–South and East–West components of wind velocity throughout the day. Seasonal averages (table 2). The broken curves show the sum of the first three terms of the Fourier series, representing prevailing, diurnal, and semi-diurnal wind components.

Average N–S and E–W wind components for groupings of several days, based on similarities in the semi-diurnal wind vectors and in the direction of the prevailing wind (§ 2 (*c*)), are given in fig. 3. The individual points have been smoothed in sliding groups of three to reduce the effect of small hour to hour wind variations. The broken curves again represent the first three terms of the Fourier series, given in table 2.

Table 2. Results of Harmonic Analysis of North–South and East–West Wind Components for Seasonal Averages

Amplitudes are in metres sec^{-1}. Movements towards North and East are considered positive

Average 24 hour period	Prevailing $V_{NS}=$	Diurnal	Semi-Diurnal	Prevailing $V_{EW}=$	Diurnal	Semi-Diurnal
Sept. 1953	− 8·5	+ 9·2 sin 15(t−9·2)	+30·4 sin 30(t−0·6)	+13·3	+ 1·9 sin 15(t− 9·4)	+16·4 sin 30(t−3·6)
Oct. 1953	+ 1·8	+12·1 sin 15(t−6·9)	+12·9 sin 30(t−8·2)	− 6·2	+12·1 sin 15(t−10·4)	+ 8·0 sin 30(t−0·0)
Nov. 1953–Feb. 1954	+ 3·7	+ 5·3 sin 15(t+1·8)	+29·1 sin 30(t−3·5)	+11·9	+ 2·3 sin 15(t− 5·7)	+20·1 sin 30(t−6·1)
Mar.–May 1954	− 8·4	+ 4·7 sin 15(t−7·4)	+ 9·5 sin 30(t−2·1)	−10·8	+ 1·3 sin 15(t− 2·1)	+ 7·4 sin 30(t−6·2)
June–Aug. 1954	−16·5	+13·2 sin 15(t−4·9)	+14·2 sin 30(t−2·4)	+15·9	+ 8·2 sin 15(t+ 8·4)	+ 6·9 sin 30(t−3·6)
Sept. 1953–Aug. 1954	− 7·1	+ 6·5 sin 15(t−5·3)	+14·5 sin 30(t−2·3)	+ 4·8	+ 2·6 sin 15(t+11·5)	+ 9·0 sin 30(t−52)

The component plots in fig. 3 show very clearly the seasonal changes in the 12 hourly periodic wind component. The variation in the amplitude of the oscillation between winter 3 (*c*) and spring 3 (*d*), is very marked. The rapid changes in phase during the autumn months are also apparent.

Fig. 4

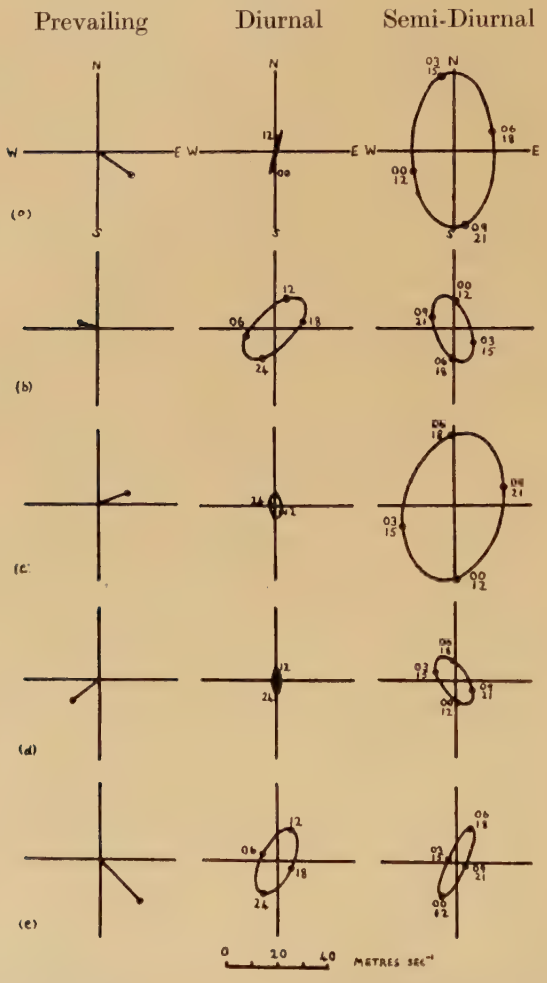

Polar plots of the prevailing, 12 hour and 24 hour periodic wind components for seasonal averages. (*a*) Sept. 1953, (*b*) Oct. 1953, (*c*) Nov. 53–Feb. 54, (*d*) Mar. 54–May 54, (*e*) June 54–Aug. 54.

Comparison of the N–S and E–W wind components shows a serious anomaly in the semi-diurnal wind. In general the amplitude of the oscillation in the North–South direction is significantly bigger than in the East West direction (up to a factor of 3). Also the phases of the oscillations do not always differ by exactly 3 hours. In summer, for

example, table 2 shows that the phase difference between the two components is only 1·2 hours. Thus the 12 hour periodic wind is only very approximately represented by a vector of constant amplitude rotating in a clockwise direction.

The ellipticity of the locus of the tip of the wind vector is illustrated more clearly in fig. 4, where the semi-diurnal N–S and E–W components of the seasonal averages have been combined in polar form, to show the actual time variations in magnitude and direction of the wind vector. In September and the winter months the ratio of major axis to minor axis is between 1·5 : 1 and 2 : 1, the major axis lying roughly in the N–S direction. In the summer months the ellipse is very eccentric, approximating more to a straight line oscillation between NE and SW, rather than to a simple rotation of the wind vector.

(*c*) *Prevailing Winds*

In addition to an oscillatory wind component, with a period of 12 hours, harmonic analysis of the N–S and E–W wind components often shows large constant terms. Such terms correspond to a steady wind blowing throughout the day. For example, during September 16–17, 1954 (fig. 1) the N–S periodic wind component oscillates about a line displaced 1·4 metres sec^{-1} to the South of the line of zero wind velocity. Similarly, in the E–W direction, the oscillation takes place about a line +16 metres sec^{-1}. There is thus a steady wind with components 1·4 and 16 metres sec^{-1} in directions towards South and East respectively—a resultant wind vector of 16 metres sec^{-1} towards East.

Components of the prevailing wind for the year September 1953 to August 1954 are shown in fig. 5. Points are shown for individual days. During summer and winter the E–W component is positive (wind towards East), with an amplitude of 20 metres sec^{-1}. Small components towards the West (~5 metres sec^{-1}) occur during the autumn months October and November, and quite large components towards the West during the spring months March and April.

In the North–South direction components of magnitude 10–20 metres sec^{-1} towards the South prevail during most of the year, with small components towards the North in the winter months.

Some prevailing wind vectors for the seasonal averages are illustrated in polar form in fig. 4. These results may be summarized as follows: winter, 15 metres sec^{-1} towards NE; spring, 15 metres sec^{-1} towards SW; summer, 25 metres sec^{-1} towards SE; and autumn (including October and November which is integrated with the winter months), 10 metres sec^{-1} towards NW.

(*d*) *Diurnal Wind Components*

(i) *Day to Day Fluctuations in Prevailing Wind*

Examination of table 1 shows that the periodic component of the wind is by no means purely 2nd harmonic. An appreciable amount of 1st harmonic is often present, corresponding to a variable wind with a period

of one day. At times this component considerably distorts the semi-diurnal oscillation. Table 1 shows that the amplitude of this component varies between 1 and 23 metres sec ^{1}, while the phases of the N–S and E–W components appear to be very irregular. It is very probable that random daily variations in the prevailing wind contribute to this 24 hour component. This is certainly the case for the observations on two successive days in December (Dec. 17–18–19, table 1). During this period the prevailing wind changed direction from South–East to North–East, distorting the 12 hour oscillation and introducing a large diurnal term.

Fig. 5

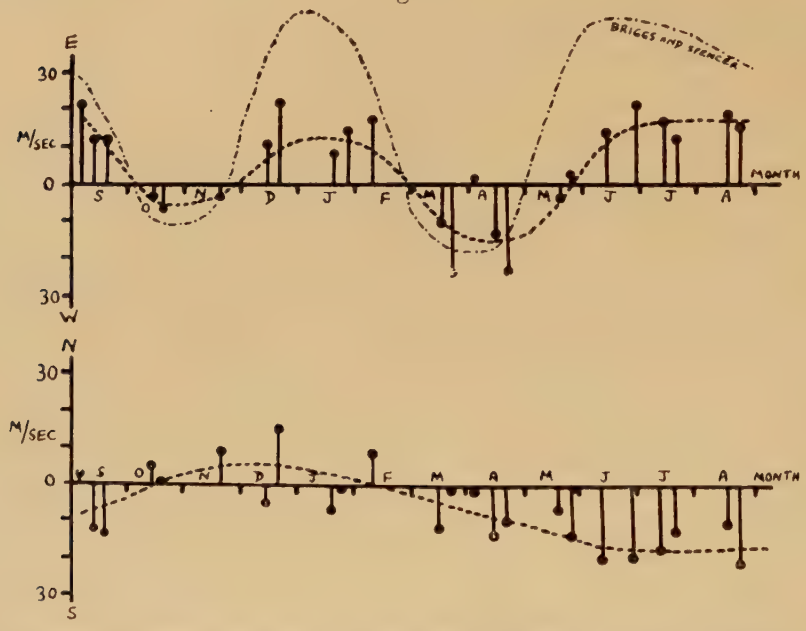

Components of prevailing wind. Sept. 53–Aug. 54. Points are shown for individual days. The East–West component of the overall wind vector for 1400–1500 h, observed by Briggs and Spencer between 1949 and 1952, is shown for comparison.

In order to search for a true diurnal component, whose amplitude may be small compared with random variations in the prevailing wind, it is therefore necessary to average a number of daily observations.

(ii) *Integration of Observations*

For the purpose of resolving the 24 hour periodic wind component, the seasonal averages of fig. 3 have been used. The diurnal terms of the harmonic analysis of the N–S and E–W components for these average days are given in table 2, and plotted in polar form in fig. 4. In October and the summer months (June–August), the diurnal wind component is of the same order as the semi-diurnal wind component. Maximum

velocity towards the North occurs at approximately 1200 h local time, and the amplitude of the component is approximately 10 metres sec^{-1}.

During the remaining months of the year the amplitude of the diurnal wind is small compared with the semi-diurnal component, even so the polar plots of fig. 7 indicate that maximum velocity towards North occurs near midday.

The wind variations of an average day for the whole year are shown in fig. 6. The points are unsmoothed. Significant 24 hour periodic wind components, equal to one third the 12 hour components, are present. Averaged over a year, the diurnal wind component may be approximately represented by a vector of amplitude 5 metres sec^{-1} rotating in a clockwise direction, directed towards the North at 11.30 h.

Fig. 6

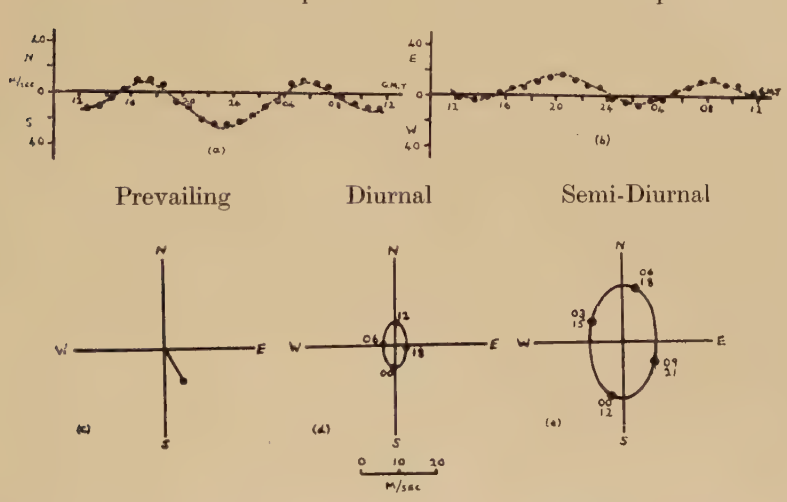

Average wind components throughout the day for the 12 month period Sept. 1953–Aug. 1954. (*a*) North–South component, (*b*) East–West component, (*c*) Prevailing wind: polar presentation, (*d*) diurnal component: polar presentation, (*e*) semi-diurnal component: polar presentation.

§ 3. Summary and Discussion

The wind system between heights of 80 and 100 km can be resolved into a number of distinct components. The most important of these is :

(*a*) *The Semi-diurnal Component*

This periodic wind can be approximately represented by a vector of amplitude 5–40 metres sec^{-1}, rotating in a clockwise direction. The phase of the rotation varies considerably, although for most of the year maximum velocity towards the North occurs near 0600 h. This is in reasonable agreement with the theory of atmospheric oscillations (Wilkes 1949), which predicts that the wind should blow towards the North at 0700 h at the 100 km level.

Disagreement with theory occurs in that the observed oscillation is markedly elliptical, and also because of the large phase changes observed during the autumn months. These effects may be due to the presence of more than one semi-diurnal wind component. The semi-diurnal pressure oscillation due to tidal forces of the sun can be resolved into two terms, a progressive wave and a stationary wave. In equatorial regions the stationary wave is small, and for this reason it is generally neglected in theoretical considerations. However, at higher latitudes the two pressure oscillations become comparable in amplitude and this may result in considerable distortion of the predicted wind system. As the phases of the two semi-diurnal pressure waves vary over the earth's surface, one being fixed in local and the other in universal time, observations at different longitudes would be of considerable value in interpreting these results.

However, the observed pressure oscillation at the earth's surface does not undergo the very large phase changes associated with the upper atmosphere winds. Thus it may be that the semi-diurnal wind component at heights of 80–100 km is not entirely due to atmospheric resonance effects as previously supposed. The autumn effect could be produced if the periodic wind was due in part to the absorption of energy in the high atmosphere, which would not be apparent in the pressure oscillation at the earth's surface. Alternatively, the form of the resonance effect could be modified by a seasonal change in the temperature distribution in the upper atmosphere.* It is interesting to observe that the pressure oscillation near the earth's surface does undergo a small annual variation in phase of approximately 30° (or 1 hour) (Chapman 1939). Most of the change takes place during the autumn months September and October, and it is tempting to associate this change with the much larger variations in phase of the upper atmosphere winds.

Comparison of the semi-diurnal wind components described in this paper, with other wind measurements in the Northern hemisphere, does not show very good agreement. Observations at Cambridge (Briggs and Spencer 1954), at a similar latitude and longitude to Jodrell Bank, show that the time of Northerly velocity occurs near 0300 h. There is thus a difference of approximately 90° (3 hours) between the phases of the two sets of observations. The Cambridge results were obtained using the ionospheric fading technique, and the measurements probably refer to a region 10–20 km higher than the meteor observations.

---

* In November 1954 the phase of the semi-diurnal component varies by 12 degrees/km between heights of 83 and 100 km. The time of velocity towards North becomes earlier with increasing altitude, varying from 1200 to 0500 h. The amplitude increases from 15 to 55 m/sec. Height changes of the wind system would thus explain both the variations in amplitude and phase observed at a fixed level, and the apparent ellipticity of the 12 hour periodic wind. In December the phase shift falls to 6 degrees/km. while the amplitude gradient remains unchanged.

The only comparable meteor observations are those of Elford and Robertson (1953) in the Southern hemisphere. For the months October–December the 12 hour component observed by these workers is directed towards the North at 0000 h, rotating in an anti-clockwise direction. It is thus in reasonable agreement with the corresponding measurements in the Northern hemisphere, as the phases of the oscillations should differ by 180° (6 hours).

(*b*) *Prevailing Winds*

Next in order of magnitude to the semi-diurnal component is the prevailing or geostrophic wind, with an amplitude of approximately 20 metres sec^{-1}. The prevailing wind undergoes seasonal variations in direction, and has components towards East in summer and winter, and components towards West in spring and autumn. The ionospheric measurements of Briggs and Spencer (1954) show that at midday the overall wind velocity is towards West in autumn and winter, and towards East in spring and summer. However, these workers did not separate the large semi-diurnal periodic wind from the steady component. In order to determine the prevailing wind the periodic components must be subtracted from the overall wind vector. Inspection of the curves of Briggs and Spencer for 1400–1500 h—when the East–West component of their periodic wind averages zero—does in fact show evidence for movements towards East in summer and winter, and towards West in spring and autumn (fig. 5). When interpreted in this way the ionospheric results thus appear to be in agreement with the meteor observations, with a semi-annual variation in the E–W component of the prevailing wind, rather than an annual variation.

North–South components at least as large as the East–West components are generally present, movement towards the South being preferred. The prevailing wind shows irregular day to day variations, and changes in direction of as much as 90° have been observed over a period of 24 hours.

(*c*) *Diurnal Wind Component*

The 24 hour periodic wind component is very small ($\sim$5 metres sec^{-1}). and is only resolvable by integrating a number of observations. On the other hand large diurnal wind components are reported by Elford and Robertson (1953), who also use a meteor echo technique. It may be that the results of these workers are influenced by the variations in prevailing wind discussed in this paper, and inspection of their 24 hour components shows that the phases are rather irregular. In two cases the N–S and E–W components are almost 180° out of phase, and in only one case approximately 90° out of phase.

If the 24 hour periodic wind components measured by Elford and Robertson are real, they represent a considerable difference in the behaviour of the wind between the two observing stations (Manchester and Adelaide).

(*d*) *Turbulent Winds*

For completeness the turbulent wind component is included in this summary, although this subject has not been considered in detail in the present paper. Almost all the measurements of large scale turbulence in the 80–100 km region have been obtained from meteor observations, both radio and visual. The r.m.s. turbulent velocity is of the order of 30 metres sec ^{1}, and wind shears of 50 metres sec^{-1} over height differences of a few kilometres are observed (Greenhow 1952, Liller and Whipple 1954).

Acknowledgments

The work has been carried out at the Jodrell Bank Experimental Station of the University of Manchester, and forms part of a research programme made possible by financial assistance from the Department of Scientific and Industrial Research. We wish to thank Professor A. C. B. Lovell for his interest in the investigations. One of us (J. S. G.) is indebted to Messrs. I. C. I. Limited for a research fellowship.

References

Briggs, B. H., and Spencer, M., 1954, *Phys. Soc. Rep. Prog. Phys.*, **17**, 245.

Chapman, S., 1939, *Int. Union of Geodesy and Geophys. Ass. of Met.* Presidential Address.

Elford, W. G., and Robertson, D. S., 1953, *J. Atmos. Terr. Phys.*, **4**, 271.

Greenhow, J. S., 1952, *J. Atmos. Terr. Phys.*, **2**, 282; 1954, *Phil. Mag.*, **45**, 471.

Liller, W., and Whipple, F. L., 1954, *Special Supp. J. Atmos. Terr. Phys.*, **1**, 112.

Manning, L. A., Villard, O. G., and Peterson, A. M., 1950, *Proc. Inst. Radio Engrs.*, **38**, 877.

Mitra, S. N., 1949, *Proc. Inst. Elect. Engrs.* (Part III) **96**, 441.

Wilkes, M. V., 1949, *Oscillations of the Earth's Atmosphere* (Cambridge: University Press).

LXVI. CORRESPONDENCE

Loss of Electrons from Fast Nitrogen Ions in Collisions with Single Gas Molecules

By K. G. Stephens and D. Walker
Physics Department, University of Birmingham

[Received March 9, 1955]

An ion moving at high speed through matter can either lose or capture electrons in collisions with the atoms of the medium traversed. This continual process of charge-exchange determines the characteristic mean charge carried by an ion when passing through a particular medium at a particular velocity. This equilibrium mean charge relates to an element of the ion path which is long enough to include a large number of charge-exchange collisions but too short for there to be any appreciable slowing down of the ion. Such equilibrium mean charges have recently been measured for moderately heavy ions (nitrogen, oxygen, and fluorine) accelerated in cyclotrons. In particular the relative probabilities of occurrence of individual charge states have been measured under conditions of charge-exchange equilibrium (Stephens and Walker 1954, 1955, Reynolds and Zucker 1954).

In the experiments of Stephens and Walker a narrow beam of ions, extracted from the Birmingham cyclotron, traversed a very thin organic film which was however thick enough to allow the ions to reach charge-exchange equilibrium. Beyond the film the ions were magnetically analysed into their various charge groups and recorded in a photographic emulsion. When incident $^{14}N^{2+}$ ions of 15 Mev (velocity$=1{\cdot}43\times10^{9}$ cm/sec) were used, the equilibrium mean charge carried by the ions emerging from the thin film was found to be $+5{\cdot}49e$ where e is the electron charge. This experiment has now been modified by replacing the organic film with a gas chamber 1·5 cm thick, containing air at pressures in the region of 10^{-2} mm Hg and having small entrance and exit holes for the beam. At these low pressures, the average number of collisions made by an ion is less than unity and the distribution in charge of the emergent ions is far removed from the equilibrium distribution observed with the thin film. In fact it is possible to say something about the number of electrons which are lost from 15 Mev $^{14}N^{2+}$ ions in individual charge-exchange collisions with gas molecules in the chamber. (The experiment of course gives no information about those collisions which do not involve charge-exchange by the ions.) The results are of interest not only in themselves but also for their bearing on the production of heavy ions of high charge in a cyclotron (Walker *et al.* 1954).

Figure 1 shows, in histogram form, the charge distributions of the emergent ions at gas chamber pressures of approximately 10^{-5} (check experiment), approximately 5×10^{-3}, $2{\cdot}3\times10^{-2}$ and $2{\cdot}7\times10^{-2}$ mm Hg respectively. From the gas pressure in the chamber (measured with a McLeod gauge) and the ratio of the number of emergent 2+ ions to the total number of emergent ions in figs. 1(*b*), 1(*c*) and 1(*d*), the cross section for the removal of one or more electrons from a 2+ ion in a single collision with a molecule of the air in the gas chamber can be computed. This cross section is found to be of the order of 4×10^{-16} cm^2.

The foregoing calculation involves the assumption that an ion of charge greater than 2+, formed in a first collision, has a negligible probability of making a second charge-exchange collision in which the ion returns to the 2+ state by electron capture. This assumption can readily be justified. Not only is the probability of a second collision in any event small because of the low gas pressure but, more important, the cross sections for the capture of electrons by 3+ or 4+ ions are small compared with the corresponding cross sections for electron loss by these ions. The latter fact can be deduced from the equilibrium charge distribution obtained earlier by using the thin film. In all the arguments which follow below we can also ignore electron capture. It is of interest in passing to observe further that, in the present experiment, very few emergent 1+ ions are observed; the cross section for electron capture by a 2+ ion is not more than 0·5% of the cross section for electron loss by this ion at the ion velocity used.

The relative abundances of 3+ ions in the distributions of fig. 1 suggest immediately that in most collisions which lead to further ionization of 15 MeV $^{14}N^{2+}$ ions only one electron is lost from an ion. An *upper limit* can be set to the fraction of cases in which more than one electron is lost by considering the data of fig. 1(*b*) relating to the gas pressure of 5×10^{-3} mm Hg. If it is assumed that in no case does an ion suffer more than one charge-exchange collision (actually a small number will do so), then 4+ and 5+ ions must be produced by the loss of more than one electron in a single collision. It is then found, from the ratio of the number of ions with a charge greater than 3+ to the number of ions with a charge greater than 2+, that multiple loss of electrons from 15 MeV $^{14}N^{2+}$ ions occurs in not more than 25±1% of charge-exchange collisions.

To obtain a *lower limit* to the fraction of charge-exchange collisions which lead to the multiple loss of electrons, we may proceed as follows. First assume that (*a*) only one electron is lost from an ion in a charge-exchange collision and (*b*) the cross section for the loss of an electron from a 3+ ion in a second collision is the same as the cross section for the loss of an electron from a 2+ ion in a first collision. If these assumptions are true then the ratio of the 3+ and 2+ abundances can be immediately predicted at any given gas pressure from the observed total probability for the loss of electrons by 2+ ions. It is found that the ratio of the number of 3+ ions to the number of 2+ ions when calculated in this way

Fig. 1

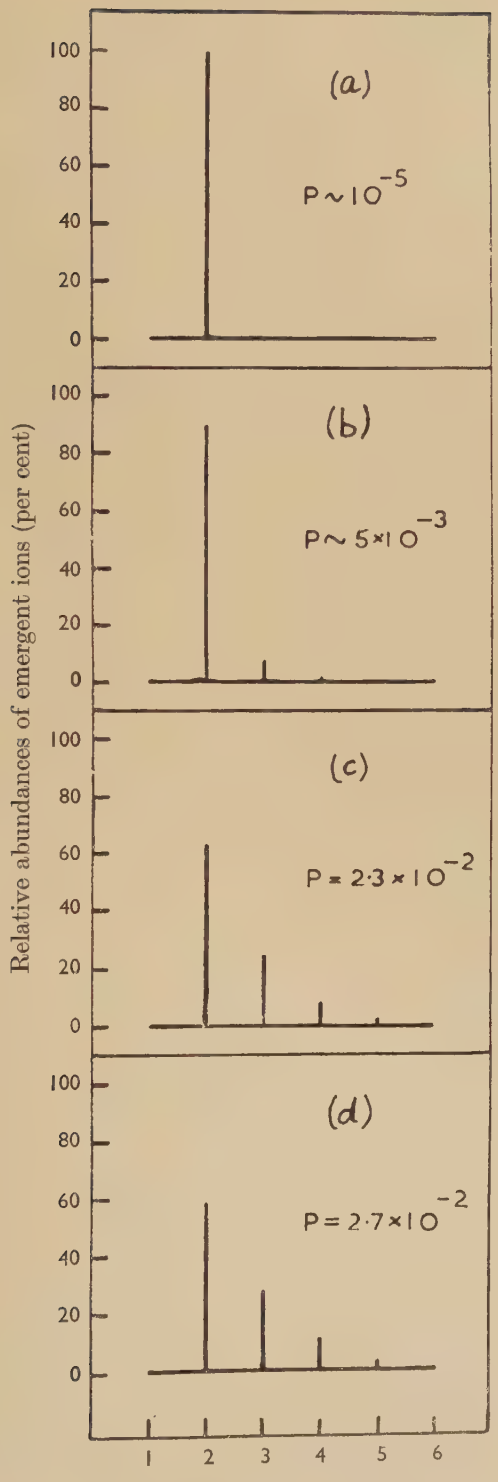

Charge distributions at gas chamber pressures of approximately 10^{-5} (check experiment), approximately 5×10^{-3}, $2{\cdot}3\times10^{-2}$ and $2{\cdot}7\times10^{-2}$ mm Hg. [In fig. 1 (*b*) the 4+ and 5+ abundances are 1·8% and 0·6% respectively.]

is always larger than the observed ratio. Expressed as a percentage of the calculated ratio, the discrepancy is greatest at the pressure of 5×10^{-3} mm and least at the pressure of $2{\cdot}7\times10^{-2}$ mm.

The discrepancy cannot be due to the breakdown of assumption (*b*) since the cross section for the loss of an electron by a 3+ ion should be less than that for the loss of an electron by a 2+ ion, a situation which would lead to an enhanced ratio of 3+ ions to 2+ ions being found experimentally. Indeed the reduction of the discrepancy between the calculated and observed ratios of 3+ to 2+ ions which occurs with increase of gas pressure must be due to just the fact that the cross section for electron loss by a 3+ ion is less than that for electron loss by a 2+ ion.

It follows that assumption (*a*) must be wrong i.e. in some cases more than one electron must be lost from 2+ ions in individual charge-exchange collisions. From the charge distribution at the gas pressure of 5×10^{-3} mm Hg we calculate the lower limit for the fraction of charge-exchange collisions which lead to multiple loss of electrons to be $20\pm3\%$.

Thus, to summarize, it can be concluded that individual charge-exchange collisions of 15 MeV $^{14}N^{2+}$ ions with gas molecules, while passing through air at a pressure of the order of 10^{-2} mm Hg, involve mostly the loss of just one electron from an ion. However between $20\pm3\%$ and $25\pm1\%$ of the charge-exchange collisions involve the loss of more than one electron from the ion, where the errors quoted are standard deviations.

References

Reynolds, H. L., and Zucker, A., 1954, *Phys. Rev.*, **95**, 1353.

Stephens, K. G., and Walker, D., 1954, *Phil. Mag.*, **45**, 543; 1955, *Proc. Roy. Soc.* A (in press).

Walker, D., Fremlin, J. H., Link, W. T., and Stephens, K. G., 1954, *Brit. J. Appl. Phys.*, **5**, 157.

Chlorine 38, 34 *Ratios from Heavy Ion Bombardments*

By A. E. Souch

Physics Department, The University of Birmingham*

[Received March 24, 1955]

§ 1. Introduction

The bombardment of aluminium with ^{14}N ions has produced a large number of radioactive products (Chackett, Fremlin and Walker 1954). After chemical separation ^{34}Cl (β^+, E_{max} 4·45 MeV) was identified but the evidence for ^{38}Cl (β^+, E_{max} 4·81 MeV) was inconclusive because of the similar half-lives of the two isotopes (33 and 37·3 minutes respectively).

The apparent lack of ^{38}Cl, quoted as probably less than 5% of ^{34}Cl, was of interest in considering possible reaction mechanisms. The isotopes

---

* Communicated by W. E. Burcham.

differ in that one emits positrons and the other negatrons. An investigation has therefore been made of the $^{38}Cl/^{34}Cl$ ratio from ^{13}C, ^{14}N and ^{16}O bombardments of aluminium, using magnetic deflection to provide charge-discrimination.

§ 2. Experimental Methods and Results

Aluminium targets were first bombarded at 25 in. radius with the internal ^{14}N beam of the 60 in. Nuffield cyclotron. The decay of the chlorine activities under a geiger counter gave a half-life in good agreement with the value for ^{34}Cl, showing that this isotope was the most abundant. The chlorine activities were examined with a semi-circular-focusing beta-spectrometer of moderate resolution. Fermi plots showed that

Table 1. Chlorine Activities measured with the Beta-spectrometer

Bombarding particle	Target element	$^{38}Cl/^{34}Cl$ ratio	^{34}Cl half-life	^{38}Cl half-life
^{14}N	Al	12·85 ± 1·5%	32 min	38 min
^{14}N	Al	14·5 ± 1·8%	35 min	40 min
^{13}C	Al	45·3 ±12·2%	33 min	39 min
^{16}O	Al	0 %		
^{14}N	Mg	5·1 ± 6·0%	29 min	

both positive and negative spectra were complex and had the right order of energies. A good value was obtained for the positron half-life and the negatron half-life was somewhat greater. Other bombardments were made and the relative yields and measured half-lives are shown in table 1.

Of the magnesium isotopes only the low abundance ^{25}Mg and ^{26}Mg can yield ^{38}Cl from ^{14}N bombardment. This is shown by the low relative yield but the result is not very accurate.

A charge-discrimination device was then built and is illustrated in fig. 1. It consisted of a pair of small, identical semi-circular-focusing beta-spectrometers with a common source. The arrangement was evacuated to a pressure of about 0·1 mm Hg. The transmission of the system was measured as a function of $B\rho$ with monoenergetic ^{137}Cs conversion electrons. Then with a suitable fixed value of the magnetic field B, the counting rates n_+ and n_- in the two counters were obtained for the chlorine source. The ratio n_-/n_+ was converted to the true ratio of $^{38}Cl/^{34}Cl$ activities by utilizing the measured transmission factor and the known energy spectra (Ruby and Richardson 1951, Langer 1950). From this ratio the relative yield of the two isotopes was calculated and the results are shown in table 2. The half-lives obtained from the first ^{14}N bombardment of magnesium were used in conjunction with the counting rates to show that 3·2% of the negative counts were due to positron activity ; this correction was applied to all of the results in table 2.

There is excellent agreement between the two methods for ^{14}N bombardment of aluminium. Although the results for ^{13}C differ, that in table 2 is of far higher accuracy.

Fig. 1

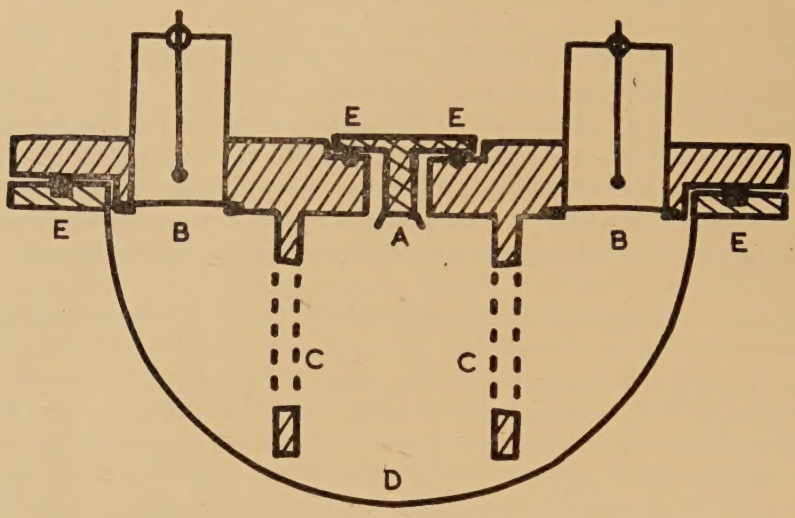

Sectional view of charge-discriminator. A, Source; B, GM4 geiger counters; C, Slit system; D, Vacuum chamber; E, Vacuum seals.

Table 2. Chlorine Activities measured with the Charge-discriminator

Bombarding particle	Target element	$^{38}Cl/^{34}Cl$ ratio	^{34}Cl half-life	^{38}Cl half-life
^{14}N	Al	12·0%	32·4 min	35·8 min
^{14}N	Al	12·5%	30·8 min	34·2 min
^{13}C	Al	21·8%	32·5 min	37·0 min
^{16}O	Al	<5 %	33 min	
^{14}N	Mg	3·4%	33·0 min	34·5 min
^{14}N	Mg	~4 %		

§ 3. Discussion

The results show the value of such methods of charge-discrimination in separating otherwise similar activities. They do not, however, provide much evidence in favour of any particular reaction mechanism.

The formation of ^{34}Cl may readily be explained on the ' buckshot ' model (Chackett *et al.* 1954) as the capture of two alpha-particles followed by the emission of a neutron. ^{38}Cl requires the capture of three alpha-particles and a neutron with the subsequent emission of two protons; the apparent lack of ^{38}Cl among the products of ^{14}N bombardment of aluminium was a qualitative argument advanced in favour of the ' buckshot ' hypothesis.

The internal heavy ion beams in the Nuffield cyclotron have a continuous energy spectrum (Walker, Fremlin, Link and Stephens 1954) of up to about 10 Mev per nucleon with an intensity fall-off by a factor two for each 10 Mev increase in energy. Compound nucleus interactions in heavy ion bombardments have been established with monenergetic beams (Cohen, Reynolds and Zucker 1954) and compound nuclei would be highly excited. The Q-values for the reactions forming ^{34}Cl and ^{38}Cl from ^{13}C, ^{14}N and ^{16}O bombardments of aluminium range from $+1{\cdot}0$ Mev to $-10{\cdot}2$ Mev with the exception of that for the ^{27}Al(^{16}O, 4p 1 n) ^{38}Cl reaction which is $-29{\cdot}5$ Mev. This latter is the only reaction of the six which is not established (see table 2) but there is otherwise no apparent correlation between Q-values and the ^{38}Cl/^{34}Cl ratios.

Acknowledgments

The author wishes to thank Dr. J. H. Fremlin for suggesting the experiment and the Department of Scientific and Industrial Research for a grant during the period in which the work was performed.

References

Chackett, K. F., Fremlin, J. H., and Walker, D., 1954, *Phil. Mag.*, **45**, 173.
Cohen, B. L., Reynolds, H. L., and Zucker, A., 1954, *Phys. Rev.*, **96**, 1617.
Langer, L. M., 1950, *Phys. Rev.*, **77**, 50.
Ruby, L., and Richardson, J. R., 1951, *Phys. Rev.*, **83**, 698.
Walker, D., Fremlin, J. H., Link, W. T., and Stephens, K. G., 1954, *Brit. J. Appl. Phys.*, **5**, 157.

On the Divergence of the Perturbation Method in Field Theory

By S. F. Edwards
Mathematical Physics Department, The University of Birmingham*

[Received March 20, 1955]

In a note published earlier in this journal (Edwards 1954, henceforward I) the problem of the convergence of the perturbation expansion of field theory was discussed, referring to the calculation of the one nucleon Green function in the approximation of neglecting vacuum polarization. In this letter it will be noted that the removal of this approximation leads to some interesting changes. In particular the analysis for nucleons interacting with Bose mesons which in I is essentially the same for nucleons obeying Fermi or Bose statistics, becomes very different when the approximation is removed. The notation of I is used : H, K are the Fredholm resolvent and determinant of the equation defining G, the bare one nucleon Green function in an external meson field ϕ. If the nucleons

---

* Communicated by Professor R. E. Peierls, F.R.S.

are bosons or fermions, the formula used in I for the complete Green function S' was

$$S' = \int HK^{-1} \exp(iL)\delta\phi \Big/ \int \exp(iL)\delta\phi.$$

If, however, the vacuum polarization effects are included, the complete formulae become

$$S'_{\text{Fermi}} = \int H \exp(iL)\delta\phi \Big/ \int K \exp(iL)\delta\phi,$$

$$S'_{\text{Bose}} = \int HK^{-2} \exp(iL)\delta\phi \Big/ \int K^{-1} \exp(iL)\delta\phi.$$

These formulae are assumed here ; they are derived from formulations of field theory in terms of functional integration (Feynman 1950, Edwards and Peierls 1954, Gelfand and Minloc 1954, Fradkin 1954, Matthews and Salam 1955, Edwards 1955) and will be discussed from the present point of view more fully in the last reference.

For our purpose, notice that by putting in cut-off factors to make all integrations finite, as in I, one obtains the results

$$S'_{\text{Fermi}} = A_{\text{F}} B_{\text{F}}^{-1},$$
$$S'_{\text{Bose}} = A_{\text{B}} B_{\text{B}}^{-1}$$

where A_{F} and B_{F} are convergent power series in the coupling constant, and A_{B}, B_{B} are asymptotic. Thus in general the series for S'_{Fermi} has a radius of convergence whilst S'_{Bose} does not. We are led thus to the surprising result that in a cut-off theory there is the radius of convergence which is finite for Fermi–Bose interaction of this type, but zero for Bose–Bose.

The author would like to thank Drs. G. Feldman, P. T. Matthews and Professor R. E. Peierls for discussions which this letter is the outcome of.

References

Edwards, S. F., 1954, *Phil. Mag.*, **45**, 758 ; 1955 (to be published).
Edwards, S. F., and Peierls, R. E., 1954, *Proc. Roy. Soc.* A, **224**, 24.
Feynman, R. P., 1950, *Phys. Rev.*, **80**, 440.
Fradkin, 1954, *Dok. Akad, Nauk.*, **98**,
Gelfand, I. M., and Minloc, R. A., 1954, *Dok. Akad, Nauk.*, **97**, 209.
Matthews, P. T., and Salam, A., 1955, *Phys. Rev.* (in course of publication).
